# ICAM-1 nanoclusters regulate hepatic epithelial cell polarity by leukocyte adhesion-independent control of apical actomyosin

Cristina Cacho-Navas[1], Carmen López-Pujante[1], Natalia Reglero-Real[2], Natalia Colás-Algora[1], Ana Cuervo[3], José Javier Conesa[3], Susana Barroso[1], Gema de Rivas[1], Sergio Ciordia[3], Alberto Paradela[3], Gianluca D'Agostino[3], Carlo Manzo[4], Jorge Feito[5], Germán Andrés[1], Francisca Molina-Jiménez[6-7], Pedro Majano[6-9], Isabel Correas[1], Jose María Carazo[3], Sussan Nourshargh[2], Meritxell Huch[10] and and Jaime Millán[1,*]

[1]Centro de Biología Molecular Severo Ochoa, CSIC-UAM, Cantoblanco, Madrid, Spain
[2]William Harvey Research Institute, Barts and The London School of Medicine and Dentistry, Queen Mary University of London, London, UK
[3]Centro Nacional de Biotecnología, CSIC, Cantoblanco, Madrid, Spain
[4]Facultat de Ciències, Tecnologia i Enginyeries, Universitat de Vic – Universitat Central de Catalunya (UVic-UCC), Vic, Spain
[5]Servicio de Anatomía Patológica, Hospital Universitario de Salamanca, Salamanca, Spain
[6]Molecular Biology Unit, Hospital Universitario de la Princesa, Madrid, Spain.
[7]Instituto de Investigación Sanitaria Hospital Universitario de La Princesa (IIS-Princesa), Madrid, Spain
[8] Centro de Investigación Biomédica en Red de Enfermedades Hepáticas y Digestivas (CIBERehd), Madrid, Spain
[9] Department of Cellular Biology, Faculty of Biology, Universidad Complutense de Madrid, Madrid, Spain
[10]Max Planck Institute of Molecular Cell Biology and Genetics, Dresden, Germany

Running title: Leukocyte-independent ICAM-1 signaling to apical actomyosin

*Correspondence: Jaime Millán, Centro de Biología Molecular Severo Ochoa, Universidad Autónoma de Madrid, Cantoblanco, 28049, Madrid, Spain
Phone: ++34 91 1964 713
Fax: ++34 91 1964 420
email: jmillan@cbm.csic.es

Number of characters: 9869

Number of Figures: 8

Number of Supplementary Figures: 6

**ABSTRACT**

Epithelial Intercellular Adhesion Molecule (ICAM)-1 is apically polarized, interacts with and guides leukocytes across epithelial barriers. Polarized hepatic epithelia organize their apical membrane domain into bile canaliculi and ducts, which are not accessible to circulating immune cells but that nevertheless confine most of ICAM-1. Here, by analyzing ICAM-1_KO human hepatic cells, liver organoids from ICAM-1_KO mice and rescue-of-function experiments, we show that ICAM-1 regulates epithelial apicobasal polarity in a leukocyte adhesion-independent manner. ICAM-1 signals to an actomyosin network at the base of canalicular microvilli, thereby controlling the dynamics and size of bile canalicular-like structures (BCs). We identified the scaffolding protein EBP50/NHERF1/SLC9A3R1, which connects membrane proteins with the underlying actin cytoskeleton, in the proximity interactome of ICAM-1. EBP50 and ICAM-1 form nano-scale domains that overlap in microvilli, from which ICAM-1 regulates EBP50 nano-organization. Indeed, EBP50 expression is required for ICAM-1-mediated control of BC morphogenesis and actomyosin. Our findings indicate that ICAM-1 regulates the dynamics of epithelial apical membrane domains beyond its role as a heterotypic cell-cell adhesion molecule and reveal potential therapeutic strategies for preserving epithelial architecture during inflammatory stress.

**KEYWORDS**

ICAM-1/ EBP50-NHERF1-SLC9A3R1/ hepatocyte polarity/ bile canaliculus/ nanocluster

## INTRODUCTION

Intercellular adhesion molecule (ICAM)-1 is the counterreceptor of leukocyte β2-integrins and mediates firm adhesion of leukocytes to epithelial and endothelial cells (Rothlein *et al*, 1986; Sumagin *et al*, 2014; Reglero-Real *et al*, 2012; Vestweber, 2015). ICAM-1 is not only a passive endothelial surface anchor for circulating immune cells, but also signals and remodels the plasma membrane and the underlying actin cytoskeleton to promote transendothelial migration (TEM) and extravasation of leukocytes in many inflammatory diseases (Reglero-Real *et al*, 2012), including those involving cholestasis, in which inhibition of ICAM-1 function reduces liver injury (Gujral *et al*, 2004). ICAM-1 is apically confined in polarized intestinal and hepatic epithelia (Sumagin *et al*, 2014; Reglero-Real *et al*, 2014, 2016), which confers on these cellular barriers the capacity to establish a haptotactic gradient between apical and basolateral membrane domains in order to guide infiltrated immune cells (Sumagin *et al*, 2014). The apical membrane domains of hepatocytes and cholangiocytes form bile canaliculi and bile ducts, respectively, which drain bile acids and other hepatic molecules into the gastrointestinal tract. The composition of the apical plasma membrane domains in these small channels differs from that of basolateral membranes and from plasma membranes in non-polarized cells, and is determined by an actin cytoskeletal network, which concentrates in these apical domains, and by mechanisms of polarized intracellular sorting of proteins and lipids towards these membrane regions (Meyer *et al*, 2020; Tsukada *et al*, 1995; Fu *et al*, 2010; Cacho-Navas *et al*, 2022; Musch, 2014). The filamentous actin cytoskeleton in the bile canaliculus forms small membrane protrusions, called microvilli, which contain actin but not myosin. However, early electron microscopy analyses and studies of bile canaliculus dynamics *in vivo* revealed the additional existence of

an actomyosin mesh surrounding the basal regions of these microvilli. This cytoskeletal scaffold regulates the diameter and dynamics of the biliary network and is involved in bile trafficking and cholestasis (Meyer *et al*, 2020; Tsukada *et al*, 1995; Gupta *et al*, 2017).

The population of hepatic ICAM-1 molecules that are segregated into bile canaliculi and ducts is not accessible to circulating immune cells, which are in contact with the basolateral membranes of hepatic epithelial cells through the space of Disse. Indeed, the adhesion of leukocytes increases when these epithelial cells lose their polarity and expose this receptor pool. Studies of ICAM-1 dynamics have demonstrated that basolateral ICAM-1 is highly dynamic, but the apical pool of receptors is highly stable and confined within BCs (Reglero-Real *et al*, 2014). This confinement depends on the interaction of ICAM-1 with the underlying canalicular F-actin (Reglero-Real *et al*, 2014). However, it is currently unknown whether segregation and immobilization of ICAM-1 into these hepatic apical plasma membrane domains play any role in canalicular dynamics and function.

Here, we have followed experimental strategies that facilitate the analysis of ICAM-1 function in absence of interactions with circulating immune cells. We have generated and characterized CRISPR-CAS9-edited human hepatic epithelial cells lacking ICAM-1 expression, and liver organoids derived in 3D from hepatic bipotent ductal stem cells of wildtype (WT) and ICAM-1_KO mice. We show that ICAM-1 regulates the size and dynamics of bile canalicular-like structures (BCs) in absence of leukocyte adhesion by controlling the actomyosin meshwork that surrounds these apical lumens. Hepatic epithelial cells lacking ICAM-1 expression have their BCs massively enlarged, although these are properly sealed and retain their ability to confine other canalicular proteins. In contrast, upregulation of

ICAM-1 expression by inflammatory cytokines greatly reduced BC frequency in a myosin-II-dependent manner. By combining super-resolution microscopy and proximal interactomics analyses we also reveal that microvillar ICAM-1 is organized into membrane nanoclusters with EBP50, a membrane-cytoskeleton protein connector that has been linked to canalicular dysruption during intrahepatic cholestasis (Bryant *et al*, 2014; Reczek & Bretscher, 2001; Hsu *et al*, 2010; Li *et al*, 2015). Indeed, we show that EBP50 controls ICAM-1-mediated regulation of polarity and actomyosin. Our findings indicate that ICAM-1 acts not only as a mediator of leukocyte infiltration in inflammatory and cholestatic diseases, but also as a master regulator of cellular scaffolds that maintain the apical membranes that form the biliary network.

## RESULTS

### ICAM-1 regulates the size and morphology of apical canalicular-like structures in human hepatic epithelial cells

We had previously shown that ICAM-1 is expressed in sinusoids but also concentrates in the bile canaliculi and bile ducts of polarized hepatic epithelial cells of the human liver parenchyma (Figure 1A) (Reglero-Real *et al*, 2014). HepG2 cells are spontaneously polarized human hepatic epithelial cells that form actin-rich, bile canalicular-like structures (BCs) and are thus a prototypical *in vitro* model for studying hepatic apicobasal polarity (Reglero-Real *et al*, 2014; Lazaro-Dieguez & Musch, 2017; Madrid *et al*, 2010; van Ijzendoorn *et al*, 1997; Cacho-Navas *et al*, 2022). To investigate the role of ICAM-1 on hepatic epithelial cell polarity, we first generated HepG2 cells in which the *ICAM-1* gene was edited using CRISPR/CAS9 (ICAM-1_KO cells) (Figure 1B and C). ICAM-1_KO cells proliferated slightly slower than parental WT cells and had similar size and percentage of cell death (Supplementary Figure 1A, B). In addition, ICAM-1_KO cells exhibited larger, less spherical and more elongated BCs than did parental WT cells, suggesting a role for this receptor in regulating BC morphology (Figure 1C and D). We called these structures enlarged BCs (eBCs) because their area was more than 2.5 times that of BCs in WT cells, although the frequency of eBCs per cell was similar to that of BCs (Figure 1E). Similar to BCs, eBCs were enriched in microvilli, sealed by tight junctions (TJs), and contained intracellular canalicular markers such as radixin (Supplementary Figure 1C). In addition, eBC did not show significant alterations in the distribution of membrane proteins that reach BCs by a direct route of intracellular transport, such as MDR1 and MRP2 (Figure 1D and Supplementary Figure 1C) (Sai *et al*, 1999), or by an indirect route, such as CD59 (Figure 1D) (de Marco *et al*, 2002). eBCs were also surrounded by a subapical compartment (SAC), as observed by detecting endogenous plasmolipin

(Cacho-Navas *et al*, 2022) (Supplementary Figure 1D) or by expressing the SAC marker GFP-Rab11 (Supplementary Figure 1E). The enlargement of these canalicular structures was rescued by expressing ICAM-1-GFP in ICAM-1_KO cells, which reduced the size of BCs to those in control HepG2 cells (Figure 1F). ICAM-1 knockdown (KD) also increased the BC area, confirming the effect of ICAM-1 reduction on BC size (Supplementary Figures 1F and G). To analyze ICAM-1-mediated morphological changes further, we performed correlative cryo-soft X-ray tomography (cryo-SXT) in control and ICAM-1_KO HepG2 cells that stably expressed GFP-Rab11 to enable the localization of BCs in live cells. Correlative Cryo-SXT revealed that eBCs from ICAM-1_KO cells contained all the morphological features of BCs, although in an enlarged state, including the abundance and length of the microvilli (Figure 1G).

Potential fusion events between eBCs were also observed by Cryo-SXT (Figure 2A) and by time-lapse fluorescence microscopy (Figure 2B, left panel, central graph, movies 1 and 2) in ICAM-1_KO cells. However, no differences in the relative changes of canalicular areas between frames were observed between KO and WT cells in these time-lapse experiments (Figure 2B, right graph). Indeed, long-term culture of ICAM-1_KO (Figure 2C and Supplementary Figure 1H) and ICAM-1_KD (Supplementary Figure 1I) cells induced the appearance of microvillus-rich structures that were much larger than eBCs observed between 48 and 72 h, covering areas of up to 100 $\mu m^2$. These structures were surrounded by TJs with a cobblestone morphology, although the TJ polygons did not enclose an underlying nucleus and, hence, did not correspond to single cells establishing cell–cell contacts (Figure 2C and D). Spherical, canalicular-like domains enriched in F-actin (Figure 2D and Supplementary Figure 1J) and similar to the BCs observed in control cells were found in

contact with these large canalicular structures, suggesting that the fusion of several BCs might contribute to the enlargement of canalicular domains in ICAM-1-depleted cells. Finally, to test whether these massive eBCs were exposed to the extracellular milieu, WT and ICAM-1_KO cells were incubated in the cold with sulfo-NHS-biotin, which labels lysine residues from proteins that are exposed on the cell surface and in contact with the medium. Cells were fixed and biotinylated proteins stained with TRITC-conjugated neutravidin. This revealed that streptavidin did not penetrate the lumens of the eBCs, indicating that these large structures are not exposed to the extracellular milieu (Figure 2E). Taken together, our analyses indicate that eBCs fuse more frequently than BCs and become considerably expanded after four days of polarization.

**ICAM-1 upregulation by inflammatory cytokines reduces hepatic apicobasal polarity**

ICAM-1 editing or silencing increases the size of apical surfaces maintaining the frequency of BCs, indicating that reducing this receptor promotes apicobasal polarity in hepatic epithelial cells. ICAM-1 is basally expressed in hepatic epithelial cells *in vitro* and *in vivo* (Smith & Thomas, 1990; Adams *et al*, 1989; Park *et al*, 2010) but its expression is strongly upregulated by cytokines during the inflammatory response (Volpes *et al*, 1990; Kvale & Brandtzaeg, 1993). We next addressed the effect of exposing polarized WT and ICAM-1_KO cells to a set of cytokines involved in liver inflammation (Park *et al*, 2010; Lacour *et al*, 2005; He *et al*, 2021). IL-1$\beta$, IFN-$\gamma$ and the combination of TNF-$\alpha$ and IFN-$\gamma$ induced the expression of ICAM-1 protein by a factor of 4-6, whereas TNF-$\alpha$ had a moderate effect (Figure 3A). The quantification of the apical-to-basolateral ratio revealed a greater increase in expression at the basolateral domains compared to the apical ones (Figure 3B and C). These changes of expression and distribution were correlated with a reduction in the number of BCs in

cytokine-stimulated cells (Figure 3D). However, BC loss was prevented when ICAM-1_KO cells were stimulated with these cytokines (Figure 3D, left graphs). In addition, BC size was not reduced upon cytokine stimulation (Figure 3D, right graphs), indicating that either the morphological remodeling of the remaining BCs is controlled by additional expression changes and signaling events triggered by these cytokines, or that these inflammatory mediators provoke the collapse of the smallest BCs, so only the enlarged ones are preserved after the treatment, giving rise to a moderate increase in the average size. However, collectively, these findings demonstrate that ICAM-1 expression levels modulate BC size and/or frequency and thus have a role in hepatic epithelial apicobasal polarity.

**ICAM-1 controls canalicular actomyosin, thereby regulating BC size**

Upon leukocyte adhesion, ICAM-1 signals to actomyosin in endothelial cells (Reglero-Real *et al*, 2012; Millan & Ridley, 2005; van Buul & Hordijk, 2004; van Buul *et al*, 2007). We hypothesized that hepatic ICAM-1, which is abundant and highly confined within BCs (Reglero-Real *et al*, 2014), could signal locally to actomyosin and thereby regulate the size and dynamics of these apical membrane domains in absence of any interaction with immune cells. To analyze the distribution of actomyosin, polarized hepatic epithelial cells expressing GFP-tagged myosin light chain (GFP-MLC) were incubated with SirActin, which concentrated into BCs similar to the phalloidin staining (Figure 4A and 1C). GFP-MLC formed a spherical network that surrounded SirActin positive BCs (Figure 4A, movie 3). Single planes of the confocal time lapse projections showed that MLC formed a ring at the base of microvilli-like actin domains, but did not localized in the most central parts of microvillar structures. High-resolution confocal microscopy of endogenous F-actin and myosin light chain phosphorylated in the T18/S19 residues (p-MLC) confirmed that active non-muscle myosin-

II complexes were distributed in the most distal parts BC where they overlapped with F-actin, which also formed microvilli-like structures (Figure 4B). In addition, the regions of F-actin that overlapped with ICAM-1 and the actomyosin network clearly differed, and the colocalization of p-MLC and ICAM-1 staining was much less extensive than that of these two proteins with F-actin, as shown by the Manders' analyses of the confocal images (Figure 4B, central and right panels). Importantly, the canalicular stainings of p-MLC (Figure 4C) and of myosin heavy chain-IIb (MHCIIb) (Figure 4D) were significantly reduced in ICAM-1_KO cells, whereas the F-actin levels were maintained (Figure 4E). In contrast, F-actin and p-MLC distribution in the basolateral membrane domains were higher in ICAM-1_KO cells than in WT cells (Figure 4E and Supplementary Figure 2A). The exogenous expression of ICAM-GFP in ICAM-1_KO cells restored the canalicular actomyosin network, indicating that ICAM-1 regulates the actomyosin cytoskeleton surrounding BCs (Figure 4C-E and Supplementary Figure 2A). Moreover, cells treated with blebbistatin, the ATPase inhibitor for non-muscle myosin-II, induced eBCs in a manner similar to that observed in ICAM-1_KO cells (Figure 4F). Blebbistatin also prevented the ICAM-1-dependent loss of BCs in response to IL-1$\beta$ (Figure 4G).

MLC phosphorylation and actomyosin contraction are regulated by the Rho kinases (ROCKs), major effectors of the RhoA subfamily of GTPases. ROCK inhibition with Y27632 phenocopied the effect of ICAM-1 editing and blebbistatin treatment on BC size (Supplementary Figure 2B). The RhoA subfamily comprises the small GTPases RhoA, RhoB and RhoC (Hodge & Ridley, 2016; Riento & Ridley, 2003), which are activated and translocated to the plasma membrane in response to different stimuli (Marcos-Ramiro *et al*, 2016, 2014). The expression of GFP-RhoB and GFP-RhoC in polarized hepatic cells suggested that the RhoA subfamily significantly

concentrates in the plasma membrane of BCs (Supplementary Figure 2C). GFP-RhoA expression completely depolarized these hepatic epithelial cells, so its apicobasal distribution could not be addressed (not shown), whereas another Rho GTPase, GFP-Rac1, was almost evenly distributed between canalicular and basolateral plasma membrane domains (Supplementary Figure 2C). Together, these results indicate that BC concentrate the machinery regulating the Rho-ROCK-actomyosin signaling pathway.

**ICAM-1 signaling to actin and non muscle myosin-II prevents BC morphogenesis**

To address whether hepatic ICAM-1 signaling to actomyosin affects hepatic cell polarity, while taking into account that canalicular ICAM-1 cannot be accessed from the canalicular lumen (Figure 2E), we adopted an alternative strategy, which involved investigating the effect of ICAM-1 surface immobilization on BC morphogenesis of epithelial cells that initially were non-polarized. A variety of antibodies, including anti-ICAM-1 antibody, and fibronectin were immobilized on coverslips. Cells were then trypsinized and seeded on the antibody-coated coverslips to analyze the effect of ICAM-1-mediated signaling. Cells seeded on anti-ICAM-1 antibody-coated converslips were unable to form BCs after 24 h of culture and had more stress fibers than did cells seeded on surfaces coated with control immunoglobulin(Ig)-G, anti-transferrin receptor (TfR) or the integrin ligand, fibronectin, all of which formed BCs with a frequency similar to that of cells plated on uncoated surfaces (Figure 5A-C). This result indicated that receptor engagement signaled to F-actin, thereby preventing the acquisition of polarity. Moreover, cells on anti-ICAM-1 antibodies frequently displayed stellate stress fibers that were similar to those arising in response to the expression of the constitutively active mutant of ROCK (Figure 5A-C) (Garg *et al*, 2008; Nakano *et al*, 1999). We found that in addition to the fraction of receptor localized on the basal surface after 24 h of adhesion,

stellate stress fibers concentrated surface ICAM-1 in their proximities (Figure 5A and Supplementary Figure 3A), whereas p-MLC localized at the F-actin-rich regions where stellate stress fibers arised (Figure 5B and Supplementary Figure 3A). These cellular structures did not constitute aberrant BCs, since they neither had a canalicular morphology nor concentrated other canalicular markers such as MDR1 (Figure 5D). When cells seeded on anti-ICAM-1-coated coverslips were treated with blebbistatin, canalicular morphogenesis was restored to a level comparable with that observed in ICAM-1_KO cells on anti-ICAM-1 antibody-coated coverslips or in cells cultured on control coverslips (Figure 5B, C and Supplementary Figure 3B). This implies that the impairment of BC formation in response to surface ICAM-1 immobilization depends on non-muscle myosin-II. As previously described, the myosin inhibitor blebbistatin affected only the distribution of MLC (Figure 5B and Supplementary Figure 3B), and not the phosphorylation of the residues recognized by the antibody (Ponsaerts *et al*, 2008; Calaminus *et al*, 2007). In addition, the overall signaling to p-MLC in cells plated on anti-ICAM-1 antibodies was similar to that of cells on FN (Supplementary Figure 3C), indicating that the impaired morphogenesis was specific to ICAM-1 immobilization, and independent of the general actin remodeling and myosin-II activation occurring in response to the adhesion and spreading of cells previously in suspension. Indeed, ICAM-1 surface engagement by clustering with a secondary antibody, independently of epithelial adhesion and spreading, was sufficient to induce the phosphorylation of MLC (Figure 5E), which demonstrates that the receptor signals to actomyosin in these cells.

ICAM-1 is the main adhesion receptor for T-cells in the hepatic epithelium (Reglero-Real *et al*, 2014). To investigate the relevance of our findings in the contest of leukocyte interaction,

we analyzed the effect of T-cell adhesion on the apicobasal polarity of hepatic epithelial cells. First, ICAM-1_KO cells had also impaired their ability to interact with T-cells, comfirming the essential role of epithelial ICAM-1 in T-cell adhesion (Supplementary Figure 3D). In addition, co-culture of T-lymphocytes with polarized HepG2 cells for at least 6 h, at an approximate ratio 1:2, reduced the number of BCs found in cells prior to adhesion by approximately 40%. Hence, these results indicate that the signaling events that control epithelial apicobasal polarity by ICAM-1 in absence of interaction with immune cells, also mediate the reduction of epithelial polarity and BC frequency upon leukocyte adhesion (Figure 5F). Collectively, these results indicate that hepatic ICAM-1 signaling to actomyosin controls canalicular morphogenesis and frequency (Figure 5G).

**The proximal interactome of ICAM-1 regulates BC size and ICAM-1-mediated signaling to actomyosin**

To characterize further the mechanisms of ICAM-1-mediated signaling to canalicular actomyosin, we analyzed the proteome in the proximity of ICAM-1 by BioID (Roux *et al*, 2012). We expressed a chimeric ICAM-1-BirA* protein, performed a biotinylation assay and analyzed the neutravidin pulldown fractions by mass spectrometry. Two independent experiments revealed a restricted set of proteins that were biotinylated in both assays and only in cells expressing the ICAM-1-BirA* chimera (Supplementary Figure 4A-C). Amongst them, the ezrin-radixin-moesin phosphoprotein (EBP)-50/NHERF1/SLC9A3R1 was detected and further validated (Figure 6A). EBP50 is an scaffolding protein that interacts with Rho and Rab GTPase activity regulators (Hsu *et al*, 2010; Reczek & Bretscher, 2001) and can bind directly to transmembrane proteins or indirectly through the interaction with ERM proteins, which in turn also bind to Ig-superfamily receptors (Barreiro *et al*, 2002; Reglero-Real *et al*,

2014). However, no proximal biotinylation was detected for ERM proteins (Supplementary Figure 4D). EBP50 has been found to interact with ICAM-1 in whole rat hepatic tissue and regulate the liver inflammatory response after bile duct ligation, although the precise molecular mechanisms underlying such regulation, and the cellular identity and localization where such interaction takes place have not been addressed (Li *et al*, 2015). We found that EBP50 was highly polarized and concentrated and colocalized with ICAM-1 in BCs (Figure 6B). Confocal analysis of hepatic tissue also revealed a sinusoidal (S) and canalicular (red arrows) distribution of EBP50 *in vivo* (Figure 6C). However, triple co-staining revealed that EBP50 was exclusively localized in the actin-positive canalicular microvilli but not in the peripheral actomyosin mesh (Figure 6D). EBP50 is a modular protein that is maintained in a closed conformation by a head-to-tail intramolecular interaction that masks its association with ligands through its two N-terminal PDZ domains (Morales *et al*, 2007). Immunoprecipitation experiments showed a weak interaction between ICAM-1 and ectopically expressed full-length EBP50, which was strongly increased when the two N-terminal PDZ domains were expressed alone, without the masking C-terminal EB domain (Figure 6E). The binding of EBP50 fragments containing only one PDZ domain was clearly reduced and suggested a preferential interaction with the second PDZ domain. The expression of these PDZ domains was sufficient to target EBP50 to BCs (Supplementary Figure 4E). Thus, ICAM-1 interacts through this PDZ tandem in addition to a potential indirect interaction through ERM proteins. This latter interaction, which occurs through the the EB domain of EBP50, could not be properly analyzed because of the very low levels of ectopic expression obtained for this fragment alone, which suggests that the EB domain is unstable and prone to degradation in absence of the rest of the protein (not shown). To better understand the ICAM-1-EBP50 molecular complexes, we analyzed the canalicular distribution of these two proteins by

super-resolution stimulated emission depletion (STED) confocal microscopy (Figure 6F). STED revealed that both ICAM-1 and EBP50 distribution was not even, but displayed patterns of overlapping nano-scale domains along F-actin-rich microvilli. These nanodomains had a size between 80 and 200 nm. In contrast, super-resolution images showed that microvillar F-actin did not form nanoscopic clusters in these filaments (Figure 6G). Furthermore, in plasma membrane regions containing few microvilli, such as those of non-polarized cells, ICAM-1 was more evenly distributed and did not overlap with EBP50 (Figure 6H). These EBP50 nanodomains, however, responded to ICAM-1 engagement by aggregating themselves, often forming circular structures of several nanoclusters, which only partially overlapped with the clustered receptor (Figure 6H and I). Such redistribution caused EBP50 to become more insoluble to mild-non inonic detergents (Supplementary Figure 4F), indicating that ICAM-1 induces changes in the condensation properties of EBP50, either by increasing the association of EBP50 to cytoskeletal structures or by changing its oligomerization properties (Fouassier *et al*, 2000). Importantly, ICAM-1 and EBP50 nanoclusters were in closer proximity in apical BCs than in non-polarized plasma membrane regions, even if non-polarized cells were exposed to anti-ICAM-1 antibody, which increased nanocluster overlapping, as shown by Manders' analyses (Figure 6I). This indicates that the proximal interaction and the potential ICAM-1-EBP50-mediated signaling mainly occur in BCs in absence of receptor engagement. In addition, it also suggests that, in addition to associating to this scaffold protein, ICAM-1 also signals and reorganizes EBP50 in macromolecular complexes that do not contain the receptor.

The absence of ICAM-1 in KO cells caused no overall dispersion of EBP50 from BCs, indicating that EBP50 is localized in these apical plasma membrane domains through additional

interactions (Figure 6J). Nevertheless, quantification of EBP50 by STED microscopy revealed an increase in the intensity of the nanodomains in ICAM-1_KO cells with respect to WT, but not in their distribution and density, measured by analyzing the nearest neighbor distance (Figure 6K, nnd). These observations suggest that EBP50 nanoclustering does not require ICAM-1 expression, but also that the receptor modulates EBP50 clustering at BCs. Next, we addressed whether EBP50 regulates canalicular size and dynamics. siRNA-mediated *SLC9A3R1* gene silencing reduced EBP50 expression by around 50% and increased BC area by almost a half (Figure 7A and B). Although moderately, this EBP50 depletion decreased pMLC staining at the canalicular actomyosin network. Unlike ICAM-1_KO cells, F-actin levels at the canalicular microvilli of EBP50_KD cells were lower than in control cells, which suggests that EBP50 has functions that are independent of ICAM-1 in these apical domains (Figure 7B). It is particularly notheworthy that EBP50 depletion attenuated the negative effect of ICAM-1 on BC morphogenesis and ICAM-1-mediated signaling to F-actin (Figure 7C-E). EBP50_KD cells formed more BCs upon ICAM-1 immobilization and reduced the number of stress fibers with respect to control cells (Figure 7E). In addition, EBP50 accumulated with ICAM-1 close to stellate stress fibers, consistent with the interaction between ICAM-1 and EBP50 in membrane domains enriched in underlying F-actin (Figure 7D, top images). These results indicate that EBP50 regulates ICAM-1-mediated signaling towards actomyosin. Such signaling prevents BC morphogenesis and can promote BC contraction and loss of apicobasal polarity. Given the role of ICAM-1 association with EBP50 in experimental cholestatic liver injury (Li *et al*, 2015), our findings provide a mechanistic rationale to explain the function of these molecular complex in mediating the progression of inflammatory diseases that disrupts the biliary network.

**ICAM-1 regulates the size and morphology of canalicular-like structures in an actomyosin-dependent manner in hepatic organoids**.

A confocal analysis of ICAM-1 distribution in murine livers revealed that this receptor was highly expressed in hepatic sinusoids and, with less intensity, in bile canaliculi and ducts (Figure 8A) (Colás-Algora *et al*, 2020). Hence, we performed a morphological study of bile canaliculi in livers from ICAM-1_KO mice and their WT littermates (Bullard et al., 2007), which revealed a significant increase of canalicular width in hepatic tissue lacking ICAM-1 expression (Figure 8B). This suggested that ICAM-1 regulates the biliary network of murine livers. Canalicular components such as F-actin and MRP2 were still detected in bile canaliculi form ICAM-1_KO livers, consistently with the results observed in human hepatic cells (Figure 8C). However, the specific cell-autonomous contribution of epithelial ICAM-1 with respect to the sinusoidal expression of the receptor and, above all, with respect to the adhesion of immune cells to hepatic epithelial and endothelial ICAM-1-expressing cells, could not be discriminated by analyzing these tissues. To investigate the potential cell-autonomous role of epithelial hepatic ICAM-1 on regulating canalicular membrane domains and cell polarity, independent of other functions in vessels and of its interactions with leukocytes, we took advantage of recent advances in the generation of hepatic organoids obtained from 3D culture and expansion of ductal bipotent stem cells isolated from human and murine livers (Supplementary Figure 5A) (Broutier *et al*, 2016; Huch *et al*, 2015). Murine hepatic organoids expressed hepatocyte markers such as albumin. They also expressed ICAM-1 without previous exposure to inflammatory stimuli (Supplementary Figure 5B) (Broutier *et al*, 2016; Huch *et al*, 2013). Hepatic organoids had an heterogenous morphology but mostly formed spheroids of cell agregrates that formed cell-cell junctions (Figure 8D, Supplementary Figure 5C). Interestingly, the bile canalicular marker HA-4 was localized between cells in the

peripheral regions of these spheroids. HA-4 exhibited a staining pattern of wide tubular and dotted domains different to that of the cell-cell junction marker ZO-1 (Figure 8D, enlarged areas). Moreover, a time-lapse analysis of carboxyfluorescein diacetate (CFDA), a fluorescent probe of hepatobiliary transport and secretion into the bile canaliculi, revealed that fluorescent CF was also laterally secreted between cells, as shown by the relative distribution of CF with respect to the nuclei, which was similar to that of HA-4 (Figures 8D and E). Transmission electron microscopy of these organoids revealed the existence of lateral cavities between cells, which were sealed by electrodense cell–cell junctions and contained long, thin microvilli, different from those observed in the plasma membrane domain facing bigger lumens in the central part of the spheroids (Figure 8F). The cell–cell junctions observed in these lateral lumens resembled the recently described membrane bulkheads that contribute to the elongation of canalicular lumens (Figure 8F, bottom right image) (Belicova *et al*, 2021). Collectively, these results suggested that differentiated hepatic organoids form BC-like lateral cavities that morphologically and functionally resemble BCs. Interestingly, ICAM-1 accumulated in these domains in mouse and human hepatic organoids (Figure 8G). pMLC and EBP50 were also localized in lateral plasma membrane domains, although EBP50 also concentrated in the plasma membrane facing central lumens (Supplementary Figure 5C). To address whether ICAM-1 regulates the morphology of these BC-like lateral cavities, we generated hepatic organoids from WT and ICAM-1_KO mice. Measuring the area of BC-like lateral lumens revealed larger areas in ICAM-1_KO than in WT differentiated organoids (Figure 8H). Time-lapse analyses of organoids incubated with CFDA (Figure 8I, top) as well as albumin secretion assays (Figure 8I, bottom) indicated that BC-like lateral domains were functional in WT and ICAM-1_KO organoids. In addition, confocal (Supplementary Figures 5D and E) and electron (Supplementary Figure 5F) microscopy

analyses also revealed that ICAM-1_KO organoids contained enlarged cells (Supplementary Figure 5G), suggesting that ICAM-1 may exert a overall control of the submembranal cytoskeletal scaffolds that control cellular size in the hepatic organoids. Finally, incubation with blebbistatin also increased the area of these lateral lumens in a manner almost identical to that observed in ICAM-1_KO organoids (Figure 8J)

Hence, collectively, our observations from the various polarized hepatic cellular models reveal that ICAM-1 is organized in nano-scale domains in surface microvilli at BCs, from where the receptor signals to actomyosin, independent of its role as an adhesion receptor for immune cells. This apical confinement of ICAM-1 regulates BC size and the hepatic cell architecture. In a more general perspective and taking into account previous reports (Reglero-Real *et al*, 2014; Cacho-Navas *et al*, 2022), these findings also provide direct evidence of a close and reciprocal connection between epithelial apicobasal polarity and the inflammatory response through ICAM-1 (Supplementary Figure 6).

**DISCUSSION**

We had previously shown that epithelial apicobasal polarity modulates leukocyte adhesion to hepatic epithelial cells by regulating ICAM-1 exposure to the extracellular milieu (Reglero-Real *et al*, 2014). Our findings here indicate that ICAM-1-mediated signaling regulates epithelial cell polarization. This signaling can emanate from receptor engagement upon leukocyte adhesion, in accordance with previous reports in different cellular contexts (Millan & Ridley, 2005; Etienne *et al*, 1998), but also by confining and enriching ICAM-1 in BCs in a leukocyte-independent manner. The participation of ICAM-1 in immune cell adhesion and trafficking through the vascular system, which are essential immune and inflammatory processes closely involved in liver pathology, makes it difficult to discriminate and quantify *in vivo* the real contribution of epithelial ICAM-1 to the loss of epithelial architecture during the progression of these pro-inflammatory diseases, independently of its function in leukocyte adhesion. However, our experiments with different cellular models demonstrate that ICAM-1 upregulation upon proinflammatory stimulation is sufficient to depolarize hepatic epithelial cells in an actomyosin-dependent manner. The concentration of this receptor in nano-scale domains in membrane regions enriched in microvilli, such as BCs, is sufficient to induce signaling to actomyosin, which regulates the contraction of these apical structures, leading to their disruption. Thus, given that many proinflammatory liver diseases, which provoke massive leukocyte infiltration into the liver, cause a reduction of epithelial apicobasal polarity in the hepatic parenchyma (Gissen & Arias, 2015), leukocyte-dependent and independent-ICAM-1 signaling may directly contribute to the pathological dysfunction of hepatocytes and cholangiocytes.

Although ICAM-1 localizes to and signals from the basolateral membrane, polarized hepatic cells express basolateral-to-apical transcytotic machinery that removes the receptor from these plasma membrane domains and confines most of ICAM-1 within the BC (Reglero-Real *et al*, 2014; Cacho-Navas *et al*, 2022). This machinery is developmentally expressed in other epithelia and is essential for the acquisition of cell polarity and differentiation of gut epithelial cells, highlighting again the molecular connections between epithelial patterning and immune response. By editing and silencing the *ICAM-1* gene, or by increasing its expression in response to inflammatory cytokines, we have shown that this apical confinement controls the canalicular dynamics by regulating the pericanalicular myosin-II levels. Bile canaliculi are mechanosensory hubs that polarize actomyosin upon changes in canalicular flow and during the regeneration of the hepatic parenchyma (Meyer *et al*, 2020). In accordance with these findings, we have found that BCs concentrate not only F-actin and actomyosin but also their master regulators, the GTPases of the RhoA subfamily. *In vivo*, myosin-II exhibits a canalicular distribution, although discriminating between subapical and fully apical distributions by high-resolution light microscopy is more difficult to achieve *in vivo* under some experimental conditions (Meyer *et al*, 2020). However, a detailed analysis of liver samples by electron microscopy has identified a subapical myosin-II network surrounding the microvillus-rich canalicular plasma membrane (Tsukada *et al*, 1995). This myosin-II activity controls the function of the bile canaliculus *in vivo* (Meyer *et al*, 2017). Pharmacological inhibition of ROCK is sufficient to increase the bile canalicular diameter in murine livers, which reduces the bile flow and delays CFDA clearance from this network of channels (Meyer *et al*, 2017). Conversely, cholestasis-inducing drugs affect hepatic myosin-II activation, suggesting that canalicular actomyosin may be a target when treating diseases related to the bile flow (Sharanek *et al*, 2016). On the other hand, blebbistatin and Y-27632

treatments are also sufficient to induce lateral, canalicular-like lumen formation in columnar epithelial cells when cell–cell junction formation is prevented. This suggests a central and specific role for the RhoA-ROCK-myosin-II pathway in forming lateral canalicular-like structures (Cohen *et al*, 2007). The enlargement of hepatic apical membranes has also been observed in the liver parenchyma in various pathological and physiological contexts, and resembles alterations observed in cells lacking proteins regulating apical membrane integrity, such as ABCB4 and Cdc42 (Pradhan-Sundd *et al*, 2019; Shitara *et al*, 2019; Sonal *et al*, 2014).

Myosin-II has been located in the terminal web, the cytoskeletal network at the base of microvilli, in a variety of epithelial cells (Delacour *et al*, 2016). Myosin-II activity in this structure negatively regulates the incorporation of G-actin into microvilli, which affects their length (Chinowsky *et al*, 2020). The myosin-II grid detected in the base of BCs under our experimental conditions display a discrete pattern that colocalizes with the most basal part of microvilli, suggesting that this cytoskeletal structure is also part of the hepatic epithelial terminal web. Therefore, crosstalk appears to exist between myosin-II at the terminal web and microvilli. If ICAM-1 expression and localization in canalicular microvilli determine the activation of pericanalicular myosin-II that controls canalicular dynamics, it is plausible that the receptor may regulate the canalicular network in proinflammatory diseases in which hepatic ICAM-1 density is massively increased. However, the effect of inflammatory cytokines on the bile flow has not been adequately addressed so far. We do know that TNF-$\alpha$ and IL-6 treatments clearly reduce bile flow in rat livers and alter canalicular dynamics *in vitro* (Ikeda *et al*, 2003). Liver pathologies with an inflammatory component have in common the loss of apicobasal polarity of epithelial cells in the hepatic parenchyma (Shousha *et al*,

2004). Our results stimulating polarized hepatic cells suggest that cellular depolarization is intrinsic to expression changes occurring in these cells upon exposure to inflammatory cytokines and that ICAM-1 induction contributes, at least in part, to polarity loss without requiring engagement by adhering leukocytes.

ICAM-1 is a type-I transmembrane protein that mediates plasma membrane remodeling upon engagement because it is connected to the underlying actin cytoskeleton by membrane-actin crosslinkers such as ERMs. In endothelial cells, engaged ICAM-1 receptor reorganizes microvilli into docking structures that mediate leukocyte adhesion and promote extravasation (Reglero-Real *et al*, 2012; Millan *et al*, 2006; Barreiro *et al*, 2002). Therefore, in other cellular contexts, ICAM-1 may help form plasma membrane domains in which the receptor is also confined. Photoactivation experiments have demonstrated that ICAM-1 concentrates and is highly stable in BCs, whereas in the basolateral plasma membrane the receptor rapidly diffuses and translocates towards the BC (Reglero-Real *et al*, 2014). This suggests that molecular mechanisms must exist that selectively stabilize or engage ICAM-1 in these apical membrane domains. Our interactome analyses revealed that ICAM-1 interacts with the scaffold protein EBP50/NHERF1/SLC9A3R1, which is also confined in canalicular microvilli. Moreover, super-resolution microscopy experiments clearly demonstrate that ICAM-1 and EBP50 are organized in overlapping nanoclusters in BC. The nature of these domains remains to be solved, but F-actin does not form clusters and is evenly distributed in microvilli, suggesting that other nano-scale structures should be involved. Liquid ordered membrane condensates or lipid rafts help form membrane microdomains based on the differential affinity of certain membrane lipids for membrane-associated proteins (Levental & Lyman, 2023), thereby regulating clustering and function of transmembrane proteins.

Lipid-ICAM-1 membrane nanodomains may be involved in the control of ICAM-1 nanodomains and their subsequent signaling since these condensates are abundant in BCs (Ismair *et al*, 2009) and a transient confinement in raft-like domains has been previously reported for ICAM-1 (Millan *et al*, 2006; Tilghman & Hoover, 2002) and EBP50 (Sultan *et al*, 2013) in different cellular contexts.

ICAM-1-actin connection through EBP50 or ERM proteins into overlapping nanodomains may therefore have a role in its apical confinement, but additional interactions mediated by ICAM-1 transmembrane and extracellular domains must contribute to its retention and function in the BCs. Ligand-mediated stabilization may be one of the mechanisms contributing to ICAM-1 retention in BCs. It is unlikely that polarized hepatic cells express and accumulate β2 integrin molecules on the canalicular surface that are able to interact in *trans* with ICAM-1. In addition, hepatic epithelial cells express very low levels of Muc1, which is another ICAM-1 ligand involved in epithelial cancer cell adhesion (Regimbald *et al*, 1996). However, hepatocytes are the main source of fibrinogen, a large protein involved in coagulation, which binds and clusters the ICAM-1 receptor by interacting with its first Ig-like domain (Tsakadze *et al*, 2002). As shown by The Human Protein Atlas (Uhlen *et al*, 2015; Yu *et al*, 2015), hepatic cells express very high levels of various fibrinogen chains and at least the fibrinogen β-chain is highly concentrated in bile canaliculi in immunohistochemical analyses of human hepatic tissue. This suggests that fibrinogen is not only secreted, but also retained close to hepatic apical membrane domains, where it could potentially interact with, cluster and stabilize canalicular ICAM-1, thereby inducing its intracellular signaling.

In conclusion, our findings indicate that ICAM-1 plays a dual role in hepatic epithelial cells: as an adhesion receptor that interacts with leukocytes and guides immune cell migration, and as a signaling molecule that regulates non-muscle myosin-II through EBP50, independent of its role as a leukocyte adhesion counter receptor, and mostly in BCs (Supplementary Figure 6). Interestingly, our results also bring together molecular machinery that is central to the progression of cholestasis in preclinical models, providing potential mechanistic insights into the canalicular collapse provoked by this pathological condition (Gupta *et al*, 2017; Li *et al*, 2015), which is linked to inflammatory responses that induce ICAM-1 expression (Gujral *et al*, 2004; Li *et al*, 2017). Further investigation into the leukocyte-independent signaling pathways orchestrated by ICAM-1 may reveal new strategies to preserve the hepatic epithelial architecture in different pathological inflammatory contexts.

## STAR METHODS

### Key Resources Table

| Reagent or resource | Source | Identifier |
|---|---|---|
| Mouse anti-ICAM-1 | R&D Systems | #BBA3; IF 1/400; IP 1/100; RRID: AB_356950 |
| Rabbit anti-ICAM-1 | Santa Cruz Biotechnology | sc-7891; WB 1/1000; RRID: AB_647486 |
| Mouse anti-ICAM-1 | Santa Cruz Biotechnology | sc-107; IHC 1/1000; RRID: AB_627120 |
| Rat anti-ICAM-1 | EBioscience | 14-0542-81; WB 1/1000; IF 1/200; RRID: AB_529544 |
| Rabbit anti-ERK1/2 | Santa Cruz Biotechnology | sc-94; WB 1/1000; AB_2140110 |
| Mouse anti-EBP50 | Santa Cruz Biotechnology | sc-271552; WB 1/1000; IF 1/400; RRID: AB_10649999 |
| Rabbit anti-EBP50 | Thermo Fisher Scientific | PA1-090; WB 1/1000; IF 1/250; RRID: AB2191493 |
| Mouse anti-tubulin | Santa Cruz Biotechnology | sc-134241; WB 1/5000; RRID: AB_2009282 |
| Rabbit anti-SNAP23 | Synaptic Systems | 111 202; WB 1/1000; IF 1/400; RRID: AB_887788 |
| Mouse anti-SNAP23 | Santa Cruz Biotechnology | sc-374215; WB 1/1000; RRID:AB_10990315 |
| Mouse anti-CD59 | EXBIO | MEM43 (11-233-C100); IF 1/400; RRID: AB_10735273 |
| Rabbit anti-ERM | Cell Signaling Technology | 3142; WB 1/1000; IF 1/400; RRID: AB_2100313 |
| Mouse anti-GFP | Roche | 11814460001; WB 1/1000; RRID: AB_390913 |
| Rabbit anti-ZO-1 | Thermo Fisher Scientific | 40-2200; IF 1/500; RRID: AB_2533456 |
| Mouse anti-Rab11 | Thermo Fisher Scientific | 71-5300; WB 1/1000; RRID: AB_2533987 |
| Mouse anti-TfR | Thermo Fisher Scientific | 13-6800; WB 1/1000: RRID: AB_2533029 |
| Rabbit anti-MLC | Cell Signaling Technology | 3672; WB 1/1000; IF 1/200; RRID: AB_10692513 |
| Rabbit anti-p(T18/S19)-MLC | Cell Signaling Technology | 3671; WB 1/1000; IF 1/200; RRID: AB_330248 |
| Rabbit anti-MHC-IIb | BioLegend | 909902; IF 1/200 ;RRID: AB_2749903 |
| Rabbit anti-MHC-IIa | BioLegend | 909802; IF 1/200 ;RRID: AB_2734686 |
| Mouse anti-Exo70 | MERCK (Millipore) | MABT186 clone 70X13F3; WB 1/500 |
| Mouse anti-IgG | MERCK (Sigma-Aldrich) | I5381; IP 1/100; RRID: AB_1163670 |
| Rabbit anti-IgG | MERCK (Sigma-Aldrich) | I5006; IP 1/100; RRID: AB_1163659 |
| Rat anti-F4/80 | Abcam | ab6640; IF 1/1000; RRID: AB_1140040 |
| Mouse anti-HA-4 antigen (CEACAM) | University of Iowa | IF 1/100; RRID: AB 10659875 |
| Rabbit anti-plasmolipin | In house | IF 1/250 |
| Rabbit anti-Radixin | Cell signaling | C4G7; IF 1/250; RRID:AB_2238294 |
| Mouse anti-MRP2 | Enzo Life Sciences | ALX-801-016; IF 1/250; RRID:AB_2273479 |

| | | |
|---|---|---|
| Mouse anti-CD3 OKT3 | ATCC | Purified from mouse hybridomas producing anti-CD3ε mAb OKT3 (our laboratory) |
| Goat F(ab) anti mouse IgG 596 | Abcam | Abcam (ab6723); IF 1/100; RRID: AB_955573 |
| Streptavidin-Alexa Fluor 555 | Thermo Fisher Scientific | S21381; RRID: AB_2307336 |
| Streptavidin-HRP | Thermo Fisher Scientific | 815-968-0747; WB 1/10000 |
| Phalloidin-Alexa Fluor 647 | Thermo Fisher Scientific | A-22287; IF 1/250; RRID:AB_2620155 |
| DAPI | MERCK | 268298; IF 1/1000 |
| Donkey anti-mouse Alexa Fluor 488 | Thermo Fisher Scientific | A-21202; IF 1/500; RRID: AB_141607 |
| Donkey anti-mouse Alexa Fluor 555 | Thermo Fisher Scientific | A-31570; IF 1/500; RRID: AB_2536180 |
| Donkey anti-mouse Alexa Fluor 647 | Thermo Fisher Scientific | A-31571; IF 1/500; RRID: AB_162542 |
| Donkey anti-rabbit Alexa Fluor 488 | Thermo Fisher Scientific | A-21206; IF 1/500; RRID: AB_141708 |
| Donkey anti-rabbit Alexa Fluor 555 | Thermo Fisher Scientific | A-31572; IF 1/500; RRID: AB_162543 |
| Donkey anti-rabbit Alexa Fluor 647 | Thermo Fisher Scientific | A-31573; IF 1/500; RRID: AB_2536183 |
| Donkey anti-rat Alexa Fluor 488 | Thermo Fisher Scientific | A-21208; IF 1/500; RRID: AB_2535794 |
| Donkey anti-mouse HRP | Jackson Immunoresearch | 715-035-151 ; WB 1/5000; RRID: AB_2340771 |
| Donkey anti-rabbit HRP | GE Healthcare | NA934; WB 1/5000; RRID: AB_772206 |

## Chemicals

| **Reagent or resource** | **Source** | **Identifier** |
|---|---|---|
| Geneticin | Santa Cruz Biotechnology | 29065B |
| Ultrapure salmon sperm DNA solution | Thermo Fisher Scientific | 15632 |
| Sulfo-NHS-biotin | Thermo Fisher Scientific | 21217 |
| Neutravidin Agarose | Thermo Fisher Scientific | 29201 |
| Glutathione Sepharose | GE Healthcare | 17-0756-01 |
| Phorbol 12-miristate 13-acetate (PMA) | MERCK (Sigma-Aldrich) | P8139 |
| Ficoll | STEMCELL Technologies | 07801 |
| PHA | Thermo Fisher Scientific | 10576015 |
| IL-2 | Thermo Fisher Scientific | PHC0021 |
| Calcein-AM | Thermo Fisher Scientific | C3099 |
| Y-27632 | MERCK (Calbiochem) | 688000 |
| Blebbistatin | MERCK (Sigma Aldrich) | B-0560 |
| Biotin | MERCK (Sigma Aldrich) | B4501 |
| (5-(and-6)-Carboxyfluorescein Diacetate (CFDA) | Thermo Fisher Scientific | C195 |
| Tissue-Tek® O.C.T.™ | Sakura | 4583 |
| Holey Carbon Grids for Cryo EM | Quantifoil | R2/2 G200F1 |
| BCG albumin assay kit | MERCK (Sigma-Aldrich) | MAK124 |
| IL-1β | Peprotech | 200-01B |
| TNF-α | R&D Systems | 210-TA/CF |
| IFN-γ | Peprotech/Teb-bio | 300-02 |

| | | |
|---|---|---|
| Fibronectin | Corning | 356008 |

## Plasmids

| Plasmid | Backbone | Origin |
|---|---|---|
| ICAM-1-BirA* | pEGFP-N1 | This paper and |
| ICAM-1-GFP | pEGFP-N1 | Dr. F. Sánchez-Madrid (Madrid, Spain) (Barreiro et al., 2002) |
| pSpCas9(BB)-2ª-GFP | PX458 | Addgene; 48138; Dr F. Zhang (Cambridge, MA) |
| GFP | pEGFP-N1 | Clontech |
| GFP-Rab11 | pEGFP-C1 | Dr. F. Martín-Belmonte (Madrid, Spain) (Rodriguez-Fraticelli et al., 2015) |
| MDR1-GFP | | Dr. I.M. Arias, (Bethesda, MD) (Sai et al., 1999) |
| GFP-RhoB | pEGFP-C1 | Dr. D.Pérez-Sala (Madrid, Spain) (Marcos-Ramiro et al. 2016) |
| GFP-Rac1 | | from Dr. G. Bokoch |
| GFP-RhoC | pEGFP-C2 | Addgene; 23226; from Channing Der (Chapel Hill, NC) |
| pCMV-FLAG-EBP50(NHERF1)-FL | pCMV-2-FLAG | Addgene; 28291; from Dr. M.M. Georgescu (Houston, TX) |
| pCMV-FLAG-EBP50(NHERF1)-PDZ1-2 | pCMV-2-FLAG | Addgene; 28294 ; from Dr. M.M. Georgescu Houston, TX) |
| pCMV-FLAG-EBP50(NHERF1)-PDZ1iP | pCMV-2-FLAG | Addgene; 28295 ; from Dr. M.M. Georgescu (Houston, TX) |
| pCMV-FLAG-EBP50(NHERF1)-PDZ2 | pCMV-2-FLAG | Addgene; 28296 ; from Dr. M.M. Georgescu (Houston, TX) |
| pCMV-FLAG-EBP50(NHERF1)-EB | pCMV-2-FLAG | Addgene; 28297 ; from Dr. M.M. Georgescu (Houston, TX) |

## sgRNAs CRISPR/Cas9

| sgRNA name | 5'-3' Sequence |
|---|---|
| sgRNA ICAM-1 fw | CACCGCGCACTCCTGGTCCTGCTCG |
| sgRNA ICAM-1 rv | AAACCGAGCAGGACCAGGAGTGCGC |

## PCR oligonucleotides

| Oligonucleotide name | 5'-3' Sequence |
|---|---|
| qPCR msICAM-1 Fw | CTTCAACCCGTGCCAAGC |
| qPCR msICAM-1 Rv | GAAGGCTTCTCTGGGATGGA |
| qPCR msHRPT Fw | AAGCTTGCTGGTGAAAAGGA |
| qPCR msHRPT Rv | TTGCGCTCATCTTAGGCTTT |

| | |
|---|---|
| qPCR msALB Fw | GCGCAGATGACAGGGCGGAA |
| qPCR msALB Rv | GTGCCGTAGCATGCGGGAGG |

**siRNA oligonucleotides**

| **siRNA name** | **5'-3' Sequence / Target sequence (TS)** |
|---|---|
| siControl | AUGUAUUGGCCUGUAUUAGUU |
| siICAM-1 3'UTR | GAACAGAGUGGAAGACAUAUU |
| siSLC9A3R1 05 | (TS) CCAGAAACGCAGCAGCAAA |
| siSLC9A3R1 06 | (TS) GCGAAAACGUGGAGAAGGA |
| siSLC9A3R1 07 | GCGAGGAGCUGAAUUCCCA |
| siSLC9A3R1 08 | GAACAGUCGUGAAGCCCUG |

## Lead Contact and Materials Availability

Further information and requests for resources and reagents should be directed to, and will be fulfilled by, the Lead Contact, Jaime Millán (jmillan@cbm.csic.es).

All unique/stable reagents generated in this study will be made available on request, but we may require a Material Transfer Agreement.

## Cells and culture

Human polarized hepatic HepG2 cells were grown in high-glucose Dulbecco's modified Eagle's medium supplemented with 5% fetal bovine serum. T lymphoblasts were prepared from isolated human peripheral blood mononuclear cells (PBMCs). Nonadherent PBMCs were stimulated with 0.5% phytohemagglutinin for 48 h and maintained in RPMI medium supplemented with 2 U/ml IL-2, as previously described (Millan *et al*, 2002). Experiments were performed with memory T-lymphocytes cultured for 7-12 days. Inflammatory stimulation of human polarized hepatic cells was performed with 50 ng/ml TNF-$\alpha$, 15 ng/ml IL-1$\beta$ and IFN-$\gamma$ 1000 U/ml. These concentrations were identified after performing initial

dose-response curves and analyses of ICAM-1 expression and STAT3 and AKT phosphorylation in these cells and in human endothelial cells (Colás-Algora *et al*, 2023).

**Biliary ductal stem cell isolation and organoid culture**

Wildtype and ICAM-1_KO mice on a C57BL/6 background were used in accordance with the institutional Animal Welfare Ethical Review Body (AWERB) and UK Home Office guidelines. ICAM-1_KO mice were kindly shared by Prof. Nancy Hogg (London, UK). Briefly, ICAM-1_KO mice were generated by deleting the coding region of the ICAM-1 gene , rendering it null for all isoforms of the receptor. ICAM-_KO mice was phenotypically normal and did not require special husbandry measures (Bullard *et al*, 2007). Mouse organoids derived from hepatic bipotent stem cells were cultured as previously described (Broutier et al., 2016). Briefly, livers were isolated from mice and digested using collagenase/dispase II (0.125 mg/ml in DMEM/F12 medium). Isolated ducts were mixed with Matrigel (BD Bioscience), seeded and cultured in 3D. One week after seeding, organoids were mechanically dissociated into small fragments and transferred to fresh Matrigel. Passage was performed weekly at 1:3-1:6 split ratios. For human organoid culture, frozen organoids were previously obtained from healthy liver resections ($\sim$1 $cm^3$) from liver transplantations performed at the Erasmus Medical Center, Rotterdam, MEC-2014-060. These organoids were cultured and expanded at the CBM Severo Ochoa under a Material Transfer Agreement between the University of Cambridge and the CBM Severo Ochoa (CSIC-UAM). All *in vivo* experiments were conducted in compliance with UK legislation set out in the Animal Scientific Procedures Act 1986. All procedures were conducted in accordance with UK Home Office regulations.

**Liver organoid differentiation**

The liver organoid differentiation procedure was performed as described elsewhere (Huch et al., 2015). Briefly, liver organoids were seeded for 3 days in liver expansion medium (Broutier et al., 2016). That medium was then exchanged for differentiation medium (Broutier et al., 2016), which was replenished every 2-3 days for a period of 11-13 days. Culture medium was collected 48 h after the final medium change for albumin secretion assays. Albumin concentration in culture supernatant was determined using the BCG Albumin assay kit (Sigma-Aldrich). For the CFDA secretion assay, organoids were incubated with 0.1 μM of CFDA diluted in phenol red-free DMEM supplemented with 10 mM HEPES, pH 7.4. At 10 min, CFDA fluorescence at the BC-like, lateral lumens of live organoids were detected by time-lapse confocal microscopy under a Nikon AR1 confocal microscope. Time-lapse acquisitions were processed using Fiji image processing software (NIH, Bethesda, Maryland).

**Method Details**

**RNA preparation and PCR analysis**

RNA was extracted from organoid cultures using an RNeasy Mini RNA Extraction Kit (Qiagen), and reverse-transcribed using Moloney murine leukemia virus reverse transcriptase (Promega). cDNA was amplified in a thermal cycler (GeneAmp PCR System 9700, Applied Biosystems). The primers used are listed in the corresponding key resource table.

**Cell transfection and stable expression of exogenous proteins**

5 μg DNA/$10^6$ cells or 100 nM siRNA /$10^6$ cells were transfected by electroporation (200 mV, 950 μF and 480 Ω; Bio-Rad). Expression was measured 24-48 h post-transfection, and the

siRNA effect was analyzed 72 h post-transfection. For stable expression of exogenous proteins, transfected cells were selected by treatment with 0.75 μg/ml G-418 sulfate for at least 4 weeks after transfection. Positive cell clones were selected and maintained in drug-free medium. After several passages in this medium, >80% of cells retained expression of the exogenous protein. For CRISPR/Cas9 gene editing, the cDNA sequence was analyzed using the Breaking-Cas tool (http://bioinfogp.cnb.csic.es/tools/breakingcas), and the selected target sequences were inserted in the pSpCas9(BB)-2A-GFP plasmid, which was a gift from Feng Zhang (Massachusetts Institute of Technology, Cambridge, MA, USA) (Addgene plasmid # 48138; http://n2t.net/addgene:48138; RRID:Addgene_48138). GFP-positive cells were sorted after 24 h of transfection and plated. Individual clones were tested by immunofluorescence and immunoblot analyses.

**Laser scanning and spinning disk confocal microscopy**

HepG2 cells were grown on coverslips ($5x10^5$ cells/well), fixed in 4% paraformaldehyde (PFA) for 15 min, rinsed and treated with 10 mM glycine for 2 min to quench the aldehyde groups. Cells were then permeabilized with 0.2% Triton X-100, rinsed and blocked with 3% bovine serum albumin (BSA) in PBS for 15 min at room temperature (RT). Cells were incubated for 30 min with the primary antibodies, rinsed in PBS and incubated for 30 min with the appropriate fluorescent secondary antibodies. Actin filaments were detected with fluorophore-conjugated phalloidin (Ruiz-Saenz *et al*, 2011) (see table). Incubation with antibodies and other fluorescence reagents was always carried out at 37ºC. Phosphorylated proteins were stained using Tris-buffered saline (20 mM TRIS, pH 7.4; 150 mM NaCl) instead of PBS. For radixin and MRP-2 stainings, cells were fixed with methanol at -20ºC for 5 min and then blocked with 10 mM Gly buffer for 15 min at room temperature before

permeabilizing and incubating with specific antibodies as described above. Confocal laser scanning microscopy was carried out with a confocal Zeiss LSM710 system coupled to an AxioImager M2 microscope, a confocal Zeiss LSM 800 system coupled to an AxioObserver microscope, and a confocal Nikon AR1+ system coupled to an Eclipse Ti-E microscope. Confocal spinning microscopy was performed with a Confocal Spinning Disk SpinSR10 system from Olympus coupled to an inVerted microscope IX83. Morphological analyses and BC quantification were performed by staining for F-actin, EBP50, ICAM-1, phospho-MLC or ZO-1, depending on the experiment. The basolateral and apical intensity of ICAM-1 in WT and ICAM_KO HepG2 cells was calculated from confocal images of polarized cell colonies by measuring the fluorescence intensity in Fiji of basolateral and apical areas, respectively. Images were processed with Fiji and Imaris software to enable 3D volume reconstruction. When specified, XZ projections, produced by summing the confocal images containing the structure of interest, were shown.

**Stimulated emission depletion (STED) super-resolution microscopy**

STED super-resolution images were acquired using a confocal microscope Leica TCS SP8 (Leica Microsystems) with an immersion objective HCX PL APO CS 100x NA 1.4 (Leica). For the green channel, samples excitation was achieved using a WLL2 laser settled at 488 nm with 10% of power, fluorescence was collected through a hybrid detector in the 498-542 nm, and STED laser beam intensity (592 nm) was used at 30% of its power. For the red channel, samples excitation was achieved using a WLL2 laser settled at 553 nm with 10% of power, fluorescence was collected through a hybrid detector in the 563-620 nm, and STED laser beam intensity (660 nm) was used at 60% of its power. Images were acquired at 1024 x 1024 pixels, with a 6x zoom factor (to obtain a pixel size corresponding to 18.36 nm), frame

average 1 or 2, in the case of the red channel, a frame accumulation of 4, and a scanning speed of 400 Hz. Under these conditions, no significant photo bleaching was detected.

STED images were analyzed using a custom software written in MATLAB (The MathWorks, Inc., Natick, Massachusetts, United States) that detects fluorescent spots and provides their intensity and centroid position through an automatic detection algorithm based on fitting to a Gaussian point-spread function (PSF) profile (Martínez-Muñoz *et al*, 2018). In our experiments, the PSF profile and its full-width-at-half-maximum (FWHM = 60 nm) describing STED resolution were estimated using fluorescent spots present in the cell cytoplasm, considered as a non-aggregate state of the receptor. This PSF was applied for the identification and analysis of the spot clusters within the biliary channels. The nnd was calculated as the minimum Euclidean distance between each spot and its neighbors. Plot of the mean fluorescence intensities values and statistical analysis, calculated through the unpaired t-test with Welch's correction, were obtained using the GraphPad Prism 9 software.

**T-lymphocyte adhesion assays**

To measure the ability of T cells to induce their depolarization, HepG2 cells were plated onto 24-well plates ($5x10^4$ cells/well) for 48 h. The cells were co-cultured with T lymphocytes at a 2:1 ratio for the indicated times. After washing, cells were fixed, immunofluorescence was performed and the percentage of CD3-stained T lymphocytes or CD3-stained T cells adhering to HepG2 cells were measured under a fluorescence microscope.

**Surface protein labeling**

HepG2 cells were incubated for 30 min with 250 μg/ml of sulfo-NHS-biotin at 4°C. Cells were then washed and traces of unbound biotin were blocked by incubation for 10 min with DMEM containing 10% FBS. Cells were then incubated with TRITC-conjugated streptavidin at 4°C for 30 min to label surface-biotinylated proteins. Cells were then fixed and immunofluorescence was performed.

**Organoid whole-mount immunostaining**

Organoid staining was performed as previously described (Broutier et al., 2016). Briefly, for whole-mount immunofluorescent staining, organoids were washed twice in cold PBS before fixing in 4% PFA for 30 min at 4°C. Then, organoids were rinsed in PBS and incubated with gentle agitation in blocking buffer containing 1% DMSO, 2% BSA and 0.3% Triton X-100. Organoids were rinsed again in PBS and labeled with the primary antibodies at 4°C overnight, rinsed a further time in PBS, and incubated with the appropriate fluorescent secondary antibodies for 2 h. Finally, nuclei were stained with DAPI.

**Tissue immunofluorescence and immunohistochemistry**

Murine livers were removed and fixed overnight in 10% neutral-buffered formalin (Sigma-Aldrich) at RT. After fixation, tissues were incubated in 30% sucrose overnight and then frozen in Tissue-Tek O.C.T. compound. The sections were allowed to cool at RT and then incubated in blocking buffer (1% DMSO, 2% BSA and 0.3% Triton X-100 in PBS) for 2 h at RT. Primary antibodies were diluted in blocking buffer and incubated overnight at 4°C. Secondary antibodies were diluted in PBS containing 0.05% BSA and incubated for 2 h at RT. To facilitate analyses of hepatic ICAM-1 distribution mice were previously exposed to intraperitoneal 50 μg/kg LPS for 17 h. The analyses of bile canalicular width was performed

in absence of any inflammatory challenge to reduce the potential interactions of the hepatic receptor with immune cells. More than 80 bile canaliculi from four WT and four ICAM-1_KO mice were quantified.

The immunohistochemical analysis of human hepatic tissue was approved by the Hospital Ethics Committee of the Hospital Universitario de Salamanca. Biopsies from liver allograft rejections and control livers form healthy donors were analyzed. Formalin-fixed, paraffin-embedded sections of 4-µm thickness were deparaffinized in xylene and rehydrated through a decreasing graded ethanol solution series. After suppression of endogenous peroxidase activity (3% hydrogen peroxide, 10 min) and antigen retrieval (boiling in 10 mM citrate buffer, pH 6.0), sections were immunostained with the appropriate primary antibody, using the DakoCytomation Envision Plus peroxidase mouse system (Dako). The stained protein was visualized using DAB solution (Dako), and lightly counterstained with Mayer's hematoxylin. To ascertain the specificity of the antibody immunoreactivity, a negative control was carried out in the absence of the primary antibody; this did not produce any detectable immunolabeling.

**Correlative cryo-soft X -ray tomography**

HepG2 cells stably expressing GFP-Rab11 were grown on gold finder Quantifoil R2/2 holey carbon grids. To improve the adhesion of cells, the carbon-coated grids were glow-discharged and coated with FBS before cell seeding. The grids were then vitrified by immersion in liquid ethane on a Leica EM CPC and cryopreserved in liquid nitrogen. Samples selected by cryo-epifluorescence microscopy were transferred to a Mistral Transmission soft X-ray Microscope (TXM, Alba Synchrotron Light Source). Samples were again mapped using

an epifluorescence microscope online with the Mistral TXM. The epifluorescence microscope was equipped with an LED light source (Mightex), a Mitutoyo 20x 0.42 NA objective (Edmund Optics) and a Retiga CCD detector (QImaging). Coordinates determined in this way were used to select the X-ray acquisition areas. An X-ray energy of 520 eV was used to illuminate the samples. The photon flux on the sample was on the order of 4.6 x $10^{10}$ photons/s. Data sets were acquired using a Ni zone plate objective lens (ZP) with an outermost zone width of 40 nm (Zeiss) following a tomographic acquisition scheme. The tilt angle of sampling ranged from -65° to 65° at 1° intervals. Exposure time varied with sample thickness from 1 to 5 s per image. The final pixel size was 11.8 nm. Tilt series were normalized relative to the flat-field images, beam current and exposure time using software developed in house. Data were also corrected by the apparent point spread function (APSF) of the microscope (Oton *et al*, 2017) and deconvolved using a Wiener filter with a k=1/SNR value of 0.1 based on the signal-to-noise ratio (Oton *et al*, 2016). The pre-processed tilt series were aligned to a single rotation axis using IMOD software (Kremer *et al*, 1996) and reconstructed using TOMO3D software with 30 iterations of the SIRT algorithm (Agulleiro & Fernandez, 2011). 3D rendering volumes were represented with Chimera and ImageJ (Schneider *et al*, 2012).

**Transmission electron microscopy**

Matrigel-embedded liver organoids were *in situ* fixed with 4% paraformaldehyde and 2% glutaraldehyde in 0.1 M phosphate buffer, pH 7.4 for 2 h at RT. Postfixation was carried out with a mixture of 1% osmium tetroxide and 0.08% potassium ferricyanide for 1 h at 4°C and then with 2% uranyl acetate for 1 h at RT. Samples were dehydrated with ethanol and processed for standard Epon (TAAB-812) embedding. After polymerization, orthogonal ultrathin sections (80 nm) were collected on formvar-coated slot grids and stained with

uranyl acetate and lead citrate. Finally, sections were examined in a Jeol JEM-1400Flash transmission electron microscope operating at 100 kV. Images were recorded with a Gatan OneView (4K x 4K) CMOS camera.

**Biotinylation of ICAM-1-proximal proteins: BioID assay**

To generate an expression plasmid containing the ICAM-1-BirA* construct, the sequence coding for GFP in the ICAM-1-GFP was substituted by the BirA* sequence (Roux *et al*, 2012) obtained from the Cav1-BirA* plasmid, kindly provided by Prof. I. Correas (Centro de Biología Molecular Severo Ochoa), with BsrGI and AgeI enzymes (New England Biolabs). The expression vector coding for ICAM-1-BirA* was transfected into HepG2 cells by electroporation and cell clones stably expressing ICAM-1-BirA* were selected with G-418 as previously described (Reglero-Real *et al*, 2014). ICAM-1-BirA* HepG2 cells were cultured on 10-cm-diameter plates and, after 48 h, incubated with 50 μM biotin for 16 h, lysed and subjected to a pull-down assay of biotinylated proteins with neutravidin-agarose (Thermo Scientific) as previously described (Roux *et al*, 2012; Marcos-Ramiro *et al*, 2016). In parallel, non-transfected HepG2 cells were used as a control of the precipitation of biotinylated proteins. Lysates and pull-down pellets were analyzed by western blot and by LC-ESI QTOF tandem mass spectrometry. The identified proteins were listed and the proteins of interest were validated by western blot.

**Immunoprecipitation assays**

HepG2 were transfected with expression vectors coding for FLAG-tagged full length EBP50 and the indicated FLAG-tagged N-terminal fragments. 48 h post-transfection, cells were lysed in 400 μl of TNE buffer (50 mM Tris pH 7.4, 150 mM NaCl, 5 mM EDTA) containing 1%

Triton-X100 and a protease and phosphatase inhibitor cocktail. Lysates were incubated with 20 µl protein G-coated Sepharose (Sigma-Aldrich) previously conjugated with 5 µl of anti-FLAG antibody by overnight incubation. Lysates were precleared for 1 h with anti-IG mouse protein-G-sepharose and then incubated with anti-FLAG conjugated protein-G-sepharose for 3 h. Antibody-conjugated beads were rinsed in TNE + TX100 buffer five times and dried by aspiration. Immunoprecipitated proteins were eluted in 20 µl of Laemmli´s buffer and analyzed by western blot.

**Protein extraction and western blot**

Cell lysates and organoids cultures were prepared using Laemmli buffer supplemented with a cocktail of protease inhibitors. The lysates were heated at 95°C for 5 min and cleared by centrifugation at $14x10^3$ rpm for 5 min. The samples were loaded on acrylamide gels and transferred onto an Immobilon-PVDF membrane (Millipore), which was blocked in PBS containing 5% nonfat dry milk and incubated overnight with the indicated primary antibody. Anti-rabbit or anti-mouse horseradish-peroxidase-(HRP)-conjugated secondary antibodies were then used and the antibody–protein complexes were visualized using ECL (GE-Healthcare). Band intensities were quantified using Fiji software.

To analize the solubility of EBP50 and other proteins in non-ionic detergents upon ICAM-1 engagement, cells were incubated with 2 µg/ml anti-ICAM-1 mAb at 40ºC for 30 min, washed and incubated at 37ºC for the indicated times. Next, cells were lysed at 4ºC for 20 min in 400 µl of TNE buffer (50 mM Tris pH 7.4, 150 mM NaCl, 5 mM EDTA) containing 1% Triton-X100 and a protease and phosphatase inhibitor cocktail, passed five times through a 22G needle, incubated for 5 min at 37ºC and then centrifuged at $14x10^3$ rpm for 5 min at 4ºC to separate

the supernatant (soluble fraction) from the pellet. Pellets were washed with TNE + 1% Triton lysing buffer before adding laemmli buffer to and sonicate the samples.

**Quantification and statistical analysis**

Data are summarized as the mean and standard deviation (SD) or the mean and standard error of the mean (SEM). Student's two-tailed unpaired samples *t*-tests or two-way ANOVAs were used to establish the statistical significance ($p < 0.05$) of group differences. ANOVA tests were applied in Figures 1F, 4E and 5A-C. In all cases, data from at least three independent experiments were used. All calculations were performed using Prism 7 software.

**ACKNOWLEDGMENTS**

We gratefully acknowledge the expert technical advice of the Confocal Microscopy, Electron Microscopy and Genomic facilities of the CBM Severo Ochoa, especially the contribution of Milagros Guerra, from the electron microscopy facility. We thank the staff of the Advanced Light Microscopy and cryo-EM facilities of the CNB-CSIC for their expert technical assistance with the correlative Cryo-SXT. We also thank Dr. Eva Pereiro at ALBA Synchrotron Light Source (Cerdanyola del Vallès, Spain) for her expert technical advice, Prof. Nancy Hogg at the Francis Crick Institute (London, UK) for generating and sharing the ICAM-1_KO mouse, Dr. Lucía Cordero Espinoza at the Gurdon Institute (Cambridge, UK) for her technical support in generating liver organoids, and Ana López Sancha for her technical support with isolating the PBMCs. The work was supported by grants PID2020-119881RB-I00 from AEI (to J.M.) and P2022/BMD-7232 TomoXliver2 (to J.M., J.M.C and A.C.) and IND2019/BMD-17139 (to J.M.) from Comunidad de Madrid. S.B.F is supported by Endocornea, Convenio Colaboración CSIC, funded by Instituto de Investigación Fundación Jiménez Díaz. C.M. acknowledges support through the grant PID2021-125386NB-I00 funded by MCIN/AEI/10.13039/501100011033/ and FEDER "ERDF A way of making Europe". C.C-N. is a recipient of FPI fellowships from MINECO. N.C-A. is a recipient of an FPU fellowship from MECD. N.R-R is additionally supported by funding from the People Programme (Marie Curie Actions) of the European Union's Seventh Framework Programme (FP7/2007–2013) under REA grant agreement nº 608765.

**CONFLICT OF INTEREST**

The authors declare that they have no conflicts of interest.

## REFERENCES


Adams DH, Shaw J, Hubscher SG, Rothlein R & Neuberger JM (1989) Intercellular adhesion molecule 1 on liver allografts during rejection. *Lancet* 334: 1122–1125

Agulleiro JI & Fernandez JJ (2011) Fast tomographic reconstruction on multicore computers. *Bioinformatics* 27: 582–3

Barreiro O, Yanez-Mo M, Serrador JM, Montoya MC, Vicente-Manzanares M, Tejedor R, Furthmayr H & Sanchez-Madrid F (2002) Dynamic interaction of VCAM-1 and ICAM-1 with moesin and ezrin in a novel endothelial docking structure for adherent leukocytes. *J Cell Biol* 157: 1233–45.

Belicova L, Repnik U, Delpierre J, Gralinska E, Seifert S, Valenzuela JI, Morales-Navarrete HA, Franke C, Räägel H, Shcherbinina E, *et al* (2021) Anisotropic expansion of hepatocyte lumina enforced by apical bulkheads. *J Cell Biol* 220: e202103003

Broutier L, Andersson-Rolf A, Hindley CJ, Boj SF, Clevers H, Koo BK & Huch M (2016) Culture and establishment of self-renewing human and mouse adult liver and pancreas 3D organoids and their genetic manipulation. *Nat Protoc* 11: 1724–43

Bryant DM, Roignot J, Datta A, Overeem AW, Kim M, Yu W, Peng X, Eastburn DJ, Ewald AJ, Werb Z, *et al* (2014) A Molecular Switch for the Orientation of Epithelial Cell Polarization. *Dev Cell* 31: 171–187

Bullard DC, Hu X, Schoeb TR, Collins RG, Beaudet AL & Barnum SR (2007) Intercellular adhesion molecule-1 expression is required on multiple cell types for the development of experimental autoimmune encephalomyelitis. *J Immunol* 178: 851–7

van Buul JD & Hordijk PL (2004) Signaling in leukocyte transendothelial migration. *Arterioscler Thromb Vasc Biol* 24: 824–33

van Buul JD, Kanters E & Hordijk PL (2007) Endothelial signaling by Ig-like cell adhesion molecules. *Arterioscler Thromb Vasc Biol* 27: 1870–6

Cacho-Navas C, Reglero-Real N, Colás-Algora N, Barroso S, de Rivas G, Stamatakis K, Feito J, Andrés G, Fresno M, Kremer L, *et al* (2022) Plasmolipin regulates basolateral-to-apical transcytosis of ICAM-1 and leukocyte adhesion in polarized hepatic epithelial cells. *Cell Mol Life Sci* 79: 61

Calaminus SDJ, Auger JM, Mccarty OJT, Wakelam MJO, Machesky LM & Watson SP (2007) MyosinIIa contractility is required for maintenance of platelet structure during spreading on collagen and contributes to thrombus stability. *J Thromb Haemost* 5: 2136–2145

Carman CV, Sage PT, Sciuto TE, de la Fuente MA, Geha RS, Ochs HD, Dvorak HF, Dvorak AM & Springer TA (2007) Transcellular diapedesis is initiated by invasive podosomes. *Immunity* 26: 784–97

Chinowsky CR, Pinette JA, Meenderink LM, Lau KS & Tyska MJ (2020) Nonmuscle myosin-2 contractility-dependent actin turnover limits the length of epithelial microvilli. *Mol Biol Cell* 31: 2803–2815

Cohen D, Tian Y & Müsch A (2007) Par1b Promotes Hepatic-type Lumen Polarity in Madin Darby Canine Kidney Cells via Myosin II- and E-Cadherin–dependent Signaling. *Mol Biol Cell* 18: 2203–2215

Colás-Algora N, García-Weber D, Cacho-Navas C, Barroso S, Caballero A, Ribas C, Correas I & Millán J (2020) Compensatory increase of VE-cadherin expression through ETS1 regulates endothelial barrier function in response to TNFα. *Cell Mol Life Sci* 77: 2125–2140

Colás-Algora N, Muñoz-Pinillos P, Cacho-Navas C, Avendaño-Ortiz J, De Rivas G, Barroso

S, López-Collazo E & Millán J (2023) Simultaneous Targeting of IL-1–Signaling and IL-6–Trans-Signaling Preserves Human Pulmonary Endothelial Barrier Function During a Cytokine Storm. *Arterioscler Thromb Vasc Biol* 43: 2213–2222
Delacour D, Salomon J, Robine S & Louvard D (2016) Plasticity of the brush border — the yin and yang of intestinal homeostasis. *Nat Rev Gastroenterol Hepatol* 13: 161–174
Etienne S, Adamson P, Greenwood J, Strosberg AD, Cazaubon S & Couraud PO (1998) ICAM-1 signaling pathways associated with Rho activation in microvascular brain endothelial cells. *J Immunol* 161: 5755–61.
Fouassier L, Yun CC, Fitz JG & Doctor RB (2000) Evidence for Ezrin-Radixin-Moesin-binding Phosphoprotein 50 (EBP50) Self-association through PDZ-PDZ Interactions. *J Biol Chem* 275: 25039–25045
Fu D, Wakabayashi Y, Ido Y, Lippincott-Schwartz J & Arias IM (2010) Regulation of bile canalicular network formation and maintenance by AMP-activated protein kinase and LKB1. *J Cell Sci* 123: 3294–302
Garg R, Riento K, Keep N, Morris JDH & Ridley AJ (2008) N-terminus-mediated dimerization of ROCK-I is required for RhoE binding and actin reorganization. *Biochem J* 411: 407–414
Gissen P & Arias IM (2015) Structural and functional hepatocyte polarity and liver disease. *J Hepatol* 63: 1023–37
Gujral JS, Liu J, Farhood A, Hinson JA & Jaeschke H (2004) Functional importance of ICAM-1 in the mechanism of neutrophil-induced liver injury in bile duct-ligated mice. *Am J Physiol Gastrointest Liver Physiol* 286: G499–G507
Gupta K, Li Q, Fan JJ, Fong ELS, Song Z, Mo S, Tang H, Ng IC, Ng CW, Pawijit P, *et al* (2017) Actomyosin contractility drives bile regurgitation as an early response during obstructive cholestasis. *J Hepatol* 66: 1231–1240
He Y, Hwang S, Ahmed YA, Feng D, Li N, Ribeiro M, Lafdil F, Kisseleva T, Szabo G & Gao B (2021) Immunopathobiology and therapeutic targets related to cytokines in liver diseases. *Cell Mol Immunol* 18: 18–37
Hodge RG & Ridley AJ (2016) Regulating Rho GTPases and their regulators. *Nat Rev Mol Cell Biol* 17: 496–510
Hsu Y-H, Lin W-L, Hou Y-T, Pu Y-S, Shun C-T, Chen C-L, Wu Y-Y, Chen J-Y, Chen T-H & Jou T-S (2010) Podocalyxin EBP50 Ezrin Molecular Complex Enhances the Metastatic Potential of Renal Cell Carcinoma Through Recruiting Rac1 Guanine Nucleotide Exchange Factor ARHGEF7. *Am J Pathol* 176: 3050–3061
Huch M, Dorrell C, Boj SF, van Es JH, Li VS, van de Wetering M, Sato T, Hamer K, Sasaki N, Finegold MJ, *et al* (2013) In vitro expansion of single Lgr5+ liver stem cells induced by Wnt-driven regeneration. *Nature* 494: 247–50
Huch M, Gehart H, van Boxtel R, Hamer K, Blokzijl F, Verstegen MM, Ellis E, van Wenum M, Fuchs SA, de Ligt J, *et al* (2015) Long-term culture of genome-stable bipotent stem cells from adult human liver. *Cell* 160: 299–312
van Ijzendoorn SCD van, Zegers MMP, Kok JW & Hoekstra D (1997) Segregation of Glucosylceramide and Sphingomyelin Occurs in the Apical to Basolateral Transcytotic Route in HepG2 Cells. *J Cell Biol* 137: 347–357
Ikeda S, Mitaka T, Harada K, Sato F, Mochizuki Y & Hirata K (2003) Tumor necrosis factor-α and interleukin-6 reduce bile canalicular contractions of rat hepatocytes. *Surgery* 133: 101–109
Ismair MG, Häusler S, Stuermer CA, Guyot C, Meier PJ, Roth J & Stieger B (2009) ABC-transporters are localized in caveolin-1-positive and reggie-1-negative and reggie-2-negative microdomains of the canalicular membrane in rat hepatocytes. *Hepatology* 49: 1673–1682
Kremer JR, Mastronarde DN & McIntosh JR (1996) Computer visualization of three-

dimensional image data using IMOD. *J Struct Biol* 116: 71–6
Kvale D & Brandtzaeg P (1993) Immune modulation of adhesion molecules ICAM-1 (CD54) and LFA-3 (CD58) in human hepatocytic cell lines. *J Hepatol* 17: 347–352
Lacour S, Gautier J-C, Pallardy M & Roberts R (2005) Cytokines as potential biomarkers of liver toxicity. *Cancer Biomark* 1: 29–39
Lazaro-Dieguez F & Musch A (2017) Cell-cell adhesion accounts for the different orientation of columnar and hepatocytic cell divisions. *J Cell Biol* 216: 3847–3859
Levental I & Lyman E (2023) Regulation of membrane protein structure and function by their lipid nano-environment. *Nat Rev Mol Cell Biol* 24: 107–122
Li M, Cai SY & Boyer JL (2017) Mechanisms of bile acid mediated inflammation in the liver. *Mol Aspects Med* 56: 45–53
Li M, Mennone A, Soroka CJ, Hagey LR, Ouyang X, Weinman EJ & Boyer JL (2015) Na(+) /H(+) exchanger regulatory factor 1 knockout mice have an attenuated hepatic inflammatory response and are protected from cholestatic liver injury. *Hepatology* 62: 1227–36
Madrid R, Aranda JF, Rodriguez-Fraticelli AE, Ventimiglia L, Andres-Delgado L, Shehata M, Fanayan S, Shahheydari H, Gomez S, Jimenez A, *et al* (2010) The formin INF2 regulates basolateral-to-apical transcytosis and lumen formation in association with Cdc42 and MAL2. *Dev Cell* 18: 814–27
de Marco MC, Martin-Belmonte F, Kremer L, Albar JP, Correas I, Vaerman JP, Marazuela M, Byrne JA & Alonso MA (2002) MAL2, a novel raft protein of the MAL family, is an essential component of the machinery for transcytosis in hepatoma HepG2 cells. *J Cell Biol* 159: 37–44
Marcos-Ramiro B, Garcia-Weber D, Barroso S, Feito J, Ortega MC, Cernuda-Morollon E, Reglero-Real N, Fernandez-Martin L, Duran MC, Alonso MA, *et al* (2016) RhoB controls endothelial barrier recovery by inhibiting Rac1 trafficking to the cell border. *J Cell Biol* 213: 385–402
Marcos-Ramiro B, Garcia-Weber D & Millan J (2014) TNF-induced endothelial barrier disruption: beyond actin and Rho. *Thromb Haemost* 112
Martínez-Muñoz L, Rodríguez-Frade JM, Barroso R, Sorzano CÓS, Torreño-Pina JA, Santiago CA, Manzo C, Lucas P, García-Cuesta EM, Gutierrez E, *et al* (2018) Separating Actin-Dependent Chemokine Receptor Nanoclustering from Dimerization Indicates a Role for Clustering in CXCR4 Signaling and Function. *Mol Cell* 71: 873
Meyer K, Morales-Navarrete H, Seifert S, Wilsch-Braeuninger M, Dahmen U, Tanaka EM, Brusch L, Kalaidzidis Y & Zerial M (2020) Bile canaliculi remodeling activates YAP via the actin cytoskeleton during liver regeneration. *Mol Syst Biol* 16
Meyer K, Ostrenko O, Bourantas G, Morales-Navarrete H, Porat-Shliom N, Segovia-Miranda F, Nonaka H, Ghaemi A, Verbavatz J-M, Brusch L, *et al* (2017) A Predictive 3D Multi-Scale Model of Biliary Fluid Dynamics in the Liver Lobule. *Cell Systems* 4: 277-290.e9
Millan J, Hewlett L, Glyn M, Toomre D, Clark P & Ridley AJ (2006) Lymphocyte transcellular migration occurs through recruitment of endothelial ICAM-1 to caveola- and F-actin-rich domains. *Nat Cell Biol* 8: 113–23
Millan J, Montoya MC, Sancho D, Sanchez-Madrid F & Alonso MA (2002) Lipid rafts mediate biosynthetic transport to the T lymphocyte uropod subdomain and are necessary for uropod integrity and function. *Blood* 99: 978–84.
Millan J & Ridley AJ (2005) Rho GTPases and leucocyte-induced endothelial remodelling. *Biochem J* 385: 329–37
Morales FC, Takahashi Y, Momin S, Adams H, Chen X & Georgescu M-M (2007) NHERF1/EBP50 Head-to-Tail Intramolecular Interaction Masks Association with PDZ

Domain Ligands. *Mol Cell Biol* 27: 2527–2537
Musch A (2014) The unique polarity phenotype of hepatocytes. *Exp Cell Res* 328: 276–83
Nakano K, Takaishi K, Kodama A, Mammoto A, Shiozaki H, Monden M & Takai Y (1999) Distinct Actions and Cooperative Roles of ROCK and mDia in Rho Small G Protein-induced Reorganization of the Actin Cytoskeleton in Madin–Darby Canine Kidney Cells. *Mol Biol Cell* 10: 2481–2491
Oton J, Pereiro E, Conesa JJ, Chichon FJ, Luque D, Rodriguez JM, Perez-Berna AJ, Sorzano CO, Klukowska J, Herman GT, *et al* (2017) XTEND: Extending the depth of field in cryo soft X-ray tomography. *Sci Rep* 7: 45808
Oton J, Pereiro E, Perez-Berna AJ, Millach L, Sorzano CO, Marabini R & Carazo JM (2016) Characterization of transfer function, resolution and depth of field of a soft X-ray microscope applied to tomography enhancement by Wiener deconvolution. *Biomed Opt Express* 7: 5092–5103
Park EJ, Lee JH, Yu GY, He G, Ali SR, Holzer RG, Osterreicher CH, Takahashi H & Karin M (2010) Dietary and genetic obesity promote liver inflammation and tumorigenesis by enhancing IL-6 and TNF expression. *Cell* 140: 197–208
Ponsaerts R, D'hondt C, Bultynck G, Srinivas SP, Vereecke J & Himpens B (2008) The Myosin II ATPase Inhibitor Blebbistatin Prevents Thrombin-Induced Inhibition of Intercellular Calcium Wave Propagation in Corneal Endothelial Cells. *Invest Ophthalmol Vis Sci* 49: 4816
Pradhan-Sundd T, Kosar K, Saggi H, Zhang R, Vats R, Cornuet P, Green S, Singh S, Zeng G, Sundd P, *et al* (2019) Wnt/beta-Catenin Signaling Plays a Protective Role in the Mdr2 Knockout Murine Model of Cholestatic Liver Disease. *Hepatology*
Reczek D & Bretscher A (2001) Identification of Epi64, a Tbc/Rabgap Domain–Containing Microvillar Protein That Binds to the First PDZ Domain of Ebp50 and E3karp. *J Cell Biol* 153: 191–206
Regimbald LH, Pilarski LM, Longenecker BM, Reddish MA, Zimmermann G & Hugh JC (1996) The breast mucin MUCI as a novel adhesion ligand for endothelial intercellular adhesion molecule 1 in breast cancer. *Cancer Res* 56: 4244–9
Reglero-Real N, Alvarez-Varela A, Cernuda-Morollon E, Feito J, Marcos-Ramiro B, Fernandez-Martin L, Gomez-Lechon MJ, Muntane J, Sandoval P, Majano PL, *et al* (2014) Apicobasal polarity controls lymphocyte adhesion to hepatic epithelial cells. *Cell Rep* 8: 1879–93
Reglero-Real N, García-Weber D & Millán J (2016) Cellular Barriers after Extravasation: Leukocyte Interactions with Polarized Epithelia in the Inflamed Tissue. *Mediators inflamm* 2016: 1–10
Reglero-Real N, Marcos-Ramiro B & Millan J (2012) Endothelial membrane reorganization during leukocyte extravasation. *Cell Mol Life Sci* 69: 3079–99
Riento K & Ridley AJ (2003) Rocks: multifunctional kinases in cell behaviour. *Nat Rev Mol Cell Biol* 4: 446–56
Rothlein R, Dustin ML, Marlin SD & Springer TA (1986) A human intercellular adhesion molecule (ICAM-1) distinct from LFA-1. *J Immunol* 137: 1270–4
Roux KJ, Kim DI, Raida M & Burke B (2012) A promiscuous biotin ligase fusion protein identifies proximal and interacting proteins in mammalian cells. *J Cell Biol* 196: 801–10
Ruiz-Saenz A, Kremer L, Alonso MA, Millan J & Correas I (2011) Protein 4.1R regulates cell migration and IQGAP1 recruitment to the leading edge. *J Cell Sci* 124: 2529–38
Sai Y, Nies AT & Arias IM (1999) Bile acid secretion and direct targeting of mdr1-green fluorescent protein from Golgi to the canalicular membrane in polarized WIF-B cells. *J Cell Sci* 112: 4535–4545
Schneider CA, Rasband WS & Eliceiri KW (2012) NIH Image to ImageJ: 25 years of image

analysis. *Nat Methods* 9: 671–5
Schoppmeyer R, van Steen ACI, Kempers L, Timmerman AL, Nolte MA, Hombrink P & van Buul JD (2022) The endothelial diapedesis synapse regulates transcellular migration of human T lymphocytes in a CX3CL1- and SNAP23-dependent manner. *Cell Rep* 38: 110243
Sharanek A, Burban A, Burbank M, Le Guevel R, Li R, Guillouzo A & Guguen-Guillouzo C (2016) Rho-kinase/myosin light chain kinase pathway plays a key role in the impairment of bile canaliculi dynamics induced by cholestatic drugs. *Sci Rep* 6: 24709
Shitara A, Malec L, Ebrahim S, Chen D, Bleck C, Hoffman MP & Weigert R (2019) Cdc42 negatively regulates endocytosis during apical membrane maintenance in live animals. *Mol Biol Cell* 30: 324–332
Shousha S, Gadir F, Peston D, Bansi D, Thillainaygam AV & Murray-Lyon IM (2004) CD10 immunostaining of bile canaliculi in liver biopsies: change of staining pattern with the development of cirrhosis. *Histopathology* 45: 335–42
Smith ME & Thomas JA (1990) Cellular expression of lymphocyte function associated antigens and the intercellular adhesion molecule-1 in normal tissue. *J Clin Pathol* 43: 893–900
Sonal, Sidhaye J, Phatak M, Banerjee S, Mulay A, Deshpande O, Bhide S, Jacob T, Gehring I, Nuesslein-Volhard C, *et al* (2014) Myosin Vb mediated plasma membrane homeostasis regulates peridermal cell size and maintains tissue homeostasis in the zebrafish epidermis. *PLoS Genet* 10: e1004614
Sultan A, Luo M, Yu Q, Riederer B, Xia W, Chen M, Lissner S, Gessner JE, Donowitz M, Yun CC, *et al* (2013) Differential Association of the $Na^+/H^+$ Exchanger Regulatory Factor (NHERF) Family of Adaptor Proteins with the Raft- and the Non-Raft Brush Border Membrane Fractions of NHE3. *Cell Physiol Biochem* 32: 1386–1402
Sumagin R, Robin AZ, Nusrat A & Parkos CA (2014) Transmigrated neutrophils in the intestinal lumen engage ICAM-1 to regulate the epithelial barrier and neutrophil recruitment. *Mucosal Immunol* 7: 905–15
Tilghman RW & Hoover RL (2002) The Src-cortactin pathway is required for clustering of E-selectin and ICAM-1 in endothelial cells. *Faseb J* 16: 1257–9.
Tsakadze NL, Zhao Z & D'Souza SE (2002) Interactions of intercellular adhesion molecule-1 with fibrinogen. *Trends Cardiovasc Med* 12: 101–8
Tsukada N, Ackerley CA & Phillips MJ (1995) The structure and organization of the bile canalicular cytoskeleton with special reference to actin and actin-binding proteins. *Hepatology* 21: 1106–1113
Uhlen M, Fagerberg L, Hallstrom BM, Lindskog C, Oksvold P, Mardinoglu A, Sivertsson A, Kampf C, Sjostedt E, Asplund A, *et al* (2015) Proteomics. Tissue-based map of the human proteome. *Science* 347: 1260419
Vestweber D (2015) How leukocytes cross the vascular endothelium. *Nat Rev Immunol* 15: 692–704
Volpes R, van den Oord JJ & Desmet VJ (1990) Immunohistochemical study of adhesion molecules in liver inflammation. *Hepatology* 12: 59–65
Yu NY, Hallstrom BM, Fagerberg L, Ponten F, Kawaji H, Carninci P, Forrest AR, Hayashizaki Y, Uhlen M & Daub CO (2015) Complementing tissue characterization by integrating transcriptome profiling from the Human Protein Atlas and from the FANTOM5 consortium. *Nucleic Acids Res* 43: 6787–98

**FIGURE LEGENDS**

**Figure 1. ICAM-1 regulates the size of apical BCs in polarized HepG2 cells (A)** ICAM-1 concentrates in bile canaliculi (top images) and bile ducts (bottom images) from polarized hepatocytes and cholangioncytes, respectively (arrows), and in sinusoids in human livers from healthy donors. Right images show a two-fold enlargement of the boxed areas in left images. Inset cartoon represents the basic organization of polarized hepatocytes at the hepatic lobule. Their apical membranes form bile canaliculi and their basolateral membranes face the sinusoids. Scale bars, 10 μm **(B)** CRISPR-CAS9 mediated editing of the *ICAM1* gene (ICAM-1_KO) in HepG2 cells. Several clones were selected and pooled to prevent clonal variations. WT, parental wild type cells **(C-D)** Polarized human epithelial HepG2 cells form bile canalicular structures (BCs). Control WT and ICAM-1_KO HepG2 cells were cultured on coverslips for 72 h, fixed and stained for F-actin and ICAM-1, which concentrate in apical BCs (C), for ZO-1 and F-actin in cells expressing MDR1-GFP (D, top images) and for CD59, ZO1 and F-actin (D, bottom images). Scale bars, 20 μm. **(E)** Plots represent the mean ± SD. BC area increased from 18.9 $\pm$ 1.1 $\mu m^2$ in WT cells to 51.2 $\pm$ 7.2 $\mu m^2$ in ICAM-1_KO cells. ***p<0.001; ns, not statistically significant. BC area and frequency were quantified in at least 70 cells per experiment. Nuclei were stained with DAPI. **(F)** WT and ICAM-1_KO cells were transfected with GFP or ICAM-1-GFP expression plasmids, grown for 48 h and processed for immunofluorescence and confocal microscopy analysis (left images) or lysed for western blot analysis (central images). Single channels from the boxed areas are enlarged on the right of the corresponding image. The right panel shows the quantification of BC areas and represents the mean ± SD. * p<0.05. n=3. Scale bar, 10 μm. **(G)** Cryo-SXT of WT and ICAM-1_KO cells stably expressing GFP-Rab11 to localize BCs. Cells were cultured on holey carbon

grids for TEM for 48-72 h. BCs were identified in live cells with an epifluorescence microscope (dotted lines) and immediately vitrified and cryopreserved for cryo-SXT. SXT images show a slice the reconstructed tomogram from the boxed areas in the correlative Epifluo-SXT images. GFP-Rab11 panels display the epifluorescence images of the same area. Scale bars, 2 μm.

**Figure 2. ICAM-1 regulates BC dynamics in polarized HepG2 cells. (A)** Correlative cryo-SXT of ICAM-1_KO cells stably expressing GFP-Rab11 showing two fusing BCs. The SXT image shows an slice of the reconstructed tomogram from the boxed area in the correlative Epifluo-SXT image (top left). The GFP-Rab11 panel displays the epifluorescence image of the same area. Scale bar, 2 μm. **(B)** HepG2 cell stably expressing MDR1-GFP were subjected to time-lapse fluorescence microscopy analysis. White arrows point at MDR1-GFP-positive BCs. Red arrows point at two fusing MDR-1-GFP-positive BCs. Central panel shows the quantification of BCs in which fusing events were observed during the time-lapse microscopy assays. Right panel quantifies variations in BC area between consecutive frames, expressed as positive values. Scale bars, 10 μm **(C)** WT and ICAM-1_KO hepatic cells were cultured for at least 96 h, fixed and stained for the indicated proteins. Scale bar, 20 μm. The left scatter-plot shows the quantification of BC area of cells cultured for the indicated periods and represents the mean ± SD. *p<0.05; ***p<0.001;****p<0.0001. 50 BCs per experiment, n=3. **(D)** Distribution of F-actin and ZO-1 in ICAM-1_KO cells cultured for 96 h suggest coalescence of small BCs into enlarged (e)BC. Enlarged areas show F-actin-enriched BCs (arrows) in contact with massive eBCs. Bottom right images show a graphical representation of the top right images. Scale bar, 10 μm. **(E)** ICAM-1_KO cells were grown for 96 h and incubated with sulfo-NHS-biotin for 30 min at 4ºC, washed, fixed and permeabilized. Biotinylated surface proteins

were detected with TRITC-conjugated streptavidin. XZ stack projections are shown to visualize the relative localization of surface proteins, accessible to sulfo-NHS-biotin from the extracellular milieu, and F-actin-rich BCs (left images) and eBC (right images), which are sealed and not accessible from the extracellular milieu. Nuclei were stained with DAPI. Bottom images show a graphical representation of the top images. Scale bars, 10 μm.

**Figure 3. Upregulation of ICAM-1 expression in response to inflammatory cytokines reduces BC frequency. (A-D)** Polarized hepatic epithelial cells were stimulated or not for 48 h with 50 ng/ml TNF-α, 15 ng/ml IL-1β and IFN-γ 1000 U/ml as indicated. (A) cells were lysed and ICAM-1 expression levels detected by western blot. Tubulin was blotted as a loading control. (B-D) Cells were fixed and stained for ICAM-1, F-actin and nuclei. (B) Basolateral-to-apical ratio of ICAM-1 staining intensities. (C) Representative confocal images of the effect of cytokine treatment. Scale bar, 10 μm. (D) Quantification of BCs (left) and BC area (right). Bars represent the mean ± SD. $n \geq 3$. *p<0.05, **p<0.01, ***p<0.001, ****p<0.0001.

**Figure 4. ICAM-1 controls canalicular membrane expansion by regulating a distal canalicular actomyosin ring. (A,B)** BCs contain a ring of actomyosin. (A) Polarized HepG2 cells expressing GFP-MLC were incubated with SirActin for 2 h and subjected to time-lapse confocal microscopy. Left images show the image projection of the indicated frames. Right images show a single image of the stack corresponding to t=0 of the same time-lapse movie (B) Polarized hepatic epithelial cells were cultured on coverslips for 72 h, fixed and stained for F-actin, ICAM-1 and phosphorylated myosin light chain (pMLC) (left images). Central panel. Relative distribution of the staining intensity for the indicated proteins, starting from the distal parts of BCs, which contain actomyosin, towards the centers of the BCs, which

contain the microvillar tips. Note that p-MLC staining is mostly distal, F-actin distribute all along the profile and ICAM-1 is mostly found in microvilli. Right panel. Manders' analysis for the indicated pairs of staining. Scale bar, 3 μm **(C,D)** Control WT, ICAM-1_KO and ICAM-1_KO cells expressing ICAM-1-GFP were cultured on coverslips for 72 h, fixed and stained for pMLC and F-actin (C) and for F-actin and non-muscle myosin heavy chain-IIb (MHCIIb) (D). Scale bar, 5 μm. **(E)** Quantification of relative apical and basolateral levels of F-actin, pMLC and MHCIIb detected in (C) and (D). n=3. At least 20 BCs (apical) or 20 cells (basolateral) were quantified in each experiment. **(F)** WT cells were exposed or not to 10 μM of the myosin inhibitor blebbistatin for the indicated times. Scale bar, 10 μm. Plots show the quantification of the effect of blebbistatin on BC size (top) and BC frequency (bottom). n=3. At least 20 BCs were quantified in each experiment. **(G)** WT and ICAM-1_KO cells were cultured, stimulated with IL-1β, fixed and stained as in Figure 3. When indicated, cells were incubated with 10 μM blebbistatin for the last 40 h. BC frequency was quantified. Quantifications represent the mean ± SD. n≥3. *p<0.05, **p<0.01, ***p<0.001, ****p<0.0001. Except otherwise indicated, scale bars correspond to 5 μm.

**Figure 5. ICAM-1 signals to actomyosin thereby reducing apicobasal polarity. (A)** Surface ICAM-1 engagement reduces BC morphogenesis. ICAM-1-GFP HepG2 cells were cultured for 24 h on coverslips precoated with the indicated antibodies (α), IgG control or fibronectin (FN). Cells were fixed and stained for F-actin to quantify the amount of BCs per cell (right). Nuclei were stained with DAPI. Bars represent the mean ± SD. n=3. Scale bar, 50 μm. TfR, Transferrin receptor. **(B)** Impairment of BC morphogenesis depends on myosin-II. ICAM-1-GFP cells were cultured for 24 h as in (A) on coverslips precoated with the indicated proteins. Cells were seeded for 4 h and incubated with blebbistatin when indicated (blebb.). As a

control, ICAM-1_KO cells were plated in parallel on ICAM-1. Cells were fixed, stained for F-actin and pMLC and the amount of BCs per cell was quantified (right graph). Nuclei were stained with DAPI. Bottom images are enlargements of the boxed areas in the top images showing cells plated on αICAM-1 coverslips. Bars represent the mean ± SD. n=3. Scale bar, 20 μm; enlarged boxed area 10 μm. Note that blebbistatin inhibits myosin but does not reduce pMLC levels, as previously described. Scale bar, 10 μm. **(C)** Quantification of the stress fibers (top) and stellate stress fibers (bottom) in cells plated on the coverslips precoated with the indicated proteins as in (b). n= 4. **(D)** Stellate stress fibers concentrate F-actin and pMLC but not the canalicular marker MDR1. Hepatic epithelial cells expressing MDR1-GFP were plated on coverslips precoated with FN or anti-ICAM-1 antibody (αICAM-1). **(E)** Effect of ICAM-1 clustering (X-ICAM-1) on MLC phosphorylation. Cells were cultured for 24 h on plastic dishes and then were sequentially incubated with anti-ICAM-1 antibody (1$^{st}$ Ab) for 30 min and an specific secondary antibody (2$^{nd}$) for the indicated times. Cells were lysed and proteins were detected by western blot. Bottom plot shows the quantification of pMLC levels upon receptor clustering. **(F)** Hepatic epithelial cells stably expressing ICAM-1-GFP were cultured for 72 h and then incubated with T-lymphocytes (1 T-cell : 2 hepatic cells) for the indicated periods. The plot shows the percentage of BCs quantified prior to exposure to T-lymphocytes (0 h). Bars represent the mean ± SD. n=5. *p<0.05; **p<0.01; ***p<0.001; ****p<0.0001. (G) Current model for the effect of ICAM-1 signaling on hepatic epithelial cells. ICAM-1 engagement signals through the Rho-ROCK axe and increases the formation of actomyosin fibers that prevent the formation of actomyosin-regulated BC structures. In polarized hepatic cells, leukocyte-mediated engagement of ICAM-1 activates pericanalicular actomyosin, which induces contraction at BCs, thereby reducing their frequency.

**Figure 6. Proximal interaction of ICAM-1 with EBP50/NHERF1/SLC9A3R1 into nano-scale microvillar domains (A).** The ICAM-1 BioID interactome reveals the proximal interaction of ICAM-1 with EBP50. Parental polarized HepG2 cells (WT) and HepG2 cells stably expressing ICAM-1-BirA* were incubated with 50 μM biotin for 16 h, lysed and subjected to a pull-down (PD) assay with neutravidin-agarose. Western blots show ICAM-1 and EBP50 biotinylation. Exo70 and ERK are shown as negative controls. ICAM-1 and ICAM-1-BirA* were detected with anti-ICAM-1 antibody. **(B)** Polarized hepatic epithelial cells were fixed and stained for ICAM-1 and EBP50. BC, bile canaliculi. The Manders' analyses for the indicated pairs of staining show the remarkable co-localization between ICAM-1 and EBP50. Scale bar, 5 μm. **(C)** EBP50 is localized in murine hepatic sinusoids (S) and in the liver bile canaliculi (red arrows). Scale bar, 50 μm. **(D)** Triple staining of EBP50, F-actin and pMLC in BCs. Central panel. Relative distribution of the staining intensity for the indicated proteins, starting from the distal parts of BCs, which are enriched in actomyosin, towards the centers of the BCs, which contain the microvillar tips. Right panel. The Manders' analyses for the indicated pairs of staining show the remarkable co-localization of EBP50 with F-actin, but not with pMLC. Scale bars, 3 μm. **(E)** Hepatic epithelial cells were transfected with the indicated expression vectors coding for FLAG-tagged full-length EBP50 or its N-termina PDZ domains. 24 post-transfection, cells were lysed, subjected to immunoprecipitation with anti-FLAG antibodies and the immunoprecipitates and the lysates were analyzed by western blot for the indicated proteins. **(F,G)** Polarized hepatic epithelial cells were stained for the indicated proteins and analyzed by STED super-resolution microscopy. Only two different fluorophores could be subjected to simultaneous STED. (F) STED analysis of ICAM-1 and EBP50. Central and right images are a 2.5-fold enlargement of the boxed area in the left image, which corresponds to BCs. Bottom images are a 2-fold enlargement of the boxed area in top central and right

images, which corresponds to a canalicular microvilli-rich area. (G) STED analysis of F-actin and EBP50 in a BC. Bottom images are a 2-fold enlargement of the boxed area in the top image, which corresponds to a canalicular microvilli-rich area. Scale bars, 5 μm. **(H)** STED analyses of non-polarized epithelial cells exposed to anti-ICAM-1 for 30 min in the cold and then incubated at 37ºC for the indicated times. ICAM-1 and EBP50 did not overlap at t=0 in these non-canalicular regions. However, 90 min at 37ºC with anti-ICAM-1 antibody induced a redistribution of EBP50 into ring-shaped macroclusters that overlapped with ICAM-1 aggregates. Scale bars, 5 μm. **(I)** Manders' analyses for the indicated pairs of staining from (F) (apical) and (H) (non-polarized). **(J)** Polarized WT and ICAM-1_KO cells were fixed, stained and the intensity of EBP50 at the apical BCs was quantified by confocal microscopy (right). **(K)** Polarized WT and ICAM-1_KO cells were fixed, stained and analyzed by STED confocal microscopy. Intensity and nearest neighbor distance (nnd) of detected spots at BCs and eBCs were calculated.

**Figure 7. EBP50 regulates ICAM-1-mediated signaling. (A,B)** HepG2 cells were transfected with siRNA control (siControl) or with siRNA targeting EBP50 (siEBP50) and cultured for 72 h. Cells were lysed and analyzed by western blot for the indicated antibodies (A) or fixed and stained for the indicated proteins (B). BC frequency and area and the intensity levels of the indicated protein at BCs were quantified. Bars represent the mean ± SD of at least 3 experiments. Scale bar, 10 μm. **(C)** HepG2 cells stably expressing ICAM-1-GFP were cultured for 24 h on coverslips precoated with anti-ICAM-1 antibody, fixed and stained for F-actin and EBP50. Central and right images are an enlargement of the boxed area in the left confocal image, which shows an region enriched in stress fibers and stellate stress fibers. Scale bar, 5 μm. **(D)** HepG2 cells were transfected with siControl or siEBP50 for 48 h, then cultured for

24 h on coverslips precoated with anti-ICAM-1 antibody. Cells were fixed and stained for F-actin and EBP50. Central and right images are enlargements of the boxed areas in the left images, which show regions enriched in stress fibers and stellate stress fibers. Arrows point at BCs. **(E)** Quantification of the number of BC per cell (top) and the percentage of stress fibers per cell with respect to siControl-transfected cells (bottom) of experiments shown in (i). Bars represent the mean ± SD of at least 4 experiments. *p<0.05. **p<0.01. ***p<0.001. ****p<0.0001. A.U. Arbitrary Units. Nuclei were stained with DAPI.

**Figure 8. ICAM-1 and non muscle myosin-II regulate the size of canalicular-like cavities in hepatic organoids. (A)** ICAM-1 concentrates in bile canaliculi and bile ducts in livers of LPS-stimulated mice (arrows). S, sinusoids. Scale bars, 20 μm (left image) and 10 μm (right image). **(B)** ICAM-1, F-actin and nucleus staining of livers from WT and ICAM-1_KO mice. Scale bar, 20 μm. Right graph. Quantification of BC width from WT and ICAM_KO murine livers identified morphologically by F-actin staining more than 80 bile canaliculi from four WT and four ICAM-1_KO mice. **(C)** Immunohistochemical analyses of F-actin and MRP2 in bile canaliculi in WT and ICAM-1_KO mice. Insets show enlargements of the boxed areas. Scale bar, 6 μm. **(D)** Mouse liver organoids have a spherical morphology. Differentiated hepatic organoids were fixed and stained for the indicated antiboidies and for F-actin and nuclei to visualize cell morphology. A Z-stack projection of an organoid is shown in left an central image. A single confocal image is shown on the central right image. Enlargement of the boxed areas are shown on the right. Scale bar, 100 μm. **(E)** Mouse liver organoids were treated with 25 μM CFDA for 30 min. Left panel shows the Z-stack projections of different confocal planes of an organoid. Central and right panels show the distal and central confocal planes, respectively, of the organoid in the left images. Right images show a two-fold

magnification of the boxed areas. Scale bars, 100 μm. **(F)** Mouse liver organoids were fixed and processed for transmission electron microscopy. Cells organized in sheets facing big central lumens (central left image) but also formed cavities between their lateral membranes containing cell-cell junctions and microvilli (lateral lumens) (top and central right image, bottom cartoon). Scale bars, 5 μm. **(G)** Mouse (top) and human (bottom) liver organoids were fixed, permeabilized and stained for ICAM-1, F-actin and nuclei. Left images show a confocal plane which crosses the central part of a cell sheet. F-actin and ICAM-1 accumulations were detected between cells (arrows). ZO-1 staining clearly surrounded these accumulations in the mouse organoid (bottom). Black lines on the side of left images mark the location of the X-Z reconstructions shown in the right images. Encircled regions show lateral areas of ICAM-1 accumulation. **(H)** Ultrastructural analysis of differentiated WT and ICAM-1_KO liver organoids. Quantification of lateral lumen areas for organoids from two WT and five ICAM-1_KO mice (right). Areas of more than twenty lateral lumens were analyzed for each mouse. Bars represent the mean ± SD. Scale bars, 5 μm. **(I)** Functional comparison of WT and ICAM-1_KO organoids. WT and ICAM-1_KO organoids equally processed and secreted CFDA into lateral lumens (top images) and secreted albumin (bottom graph). A.U. arbitrary units. **(J)** Ultrastructural analysis of differentiated WT liver organoids treated or not with 10 μM blebbistatin for 24 h. Scale bars, 5 μm. The right plot shows the quantification of lateral lumen areas. Quantifications represent the mean ± SD. *p<0.05; **p<0.01; ***p<0.001;****p<0.0001. Nuclei were stained with DAPI in confocal images.

A

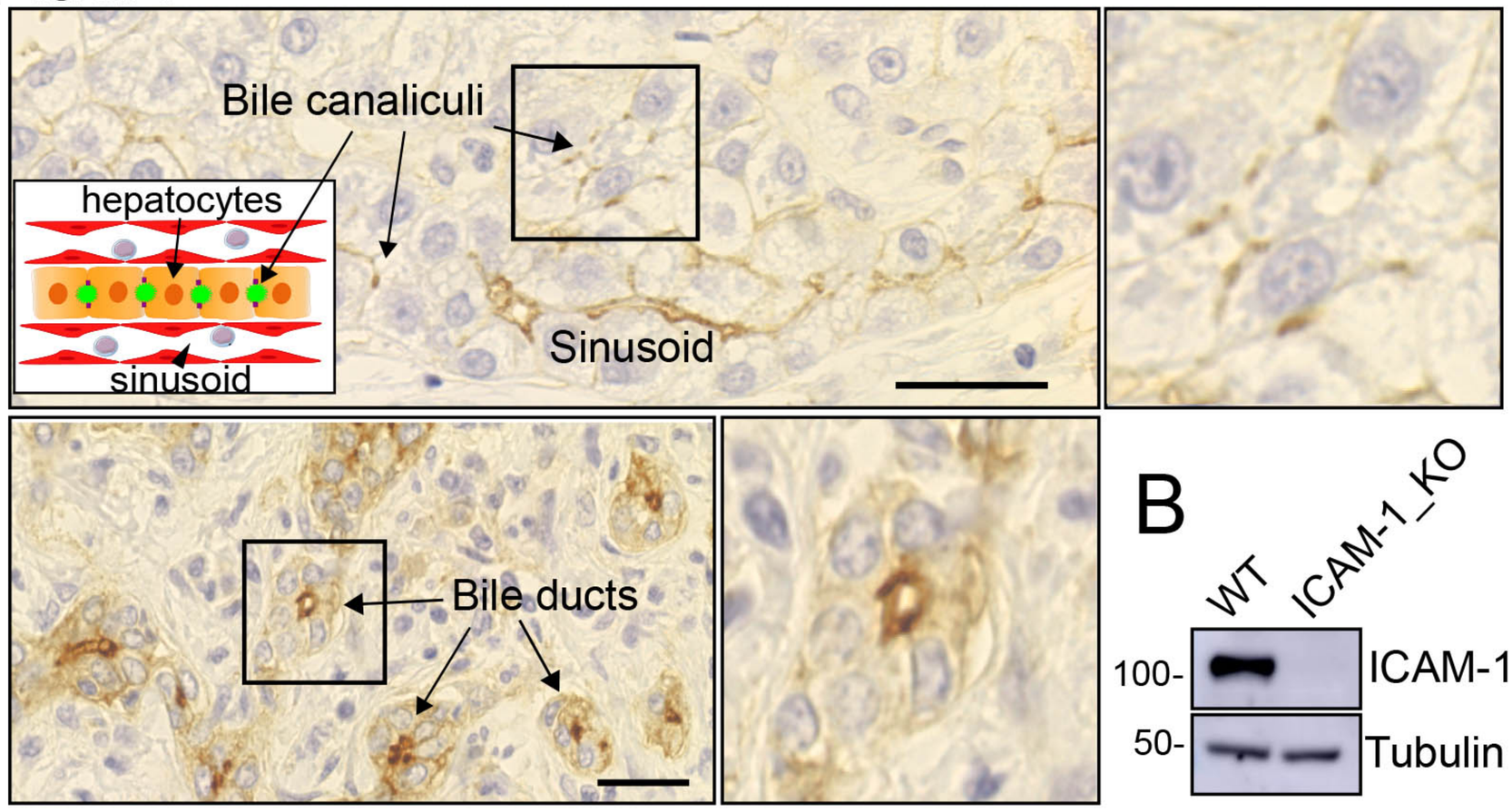
ICAM-1
Bile canaliculi
hepatocytes
sinusoid
Sinusoid
Bile ducts

B


WT
ICAM-1_KO
100-
ICAM-1
50-
Tubulin

C

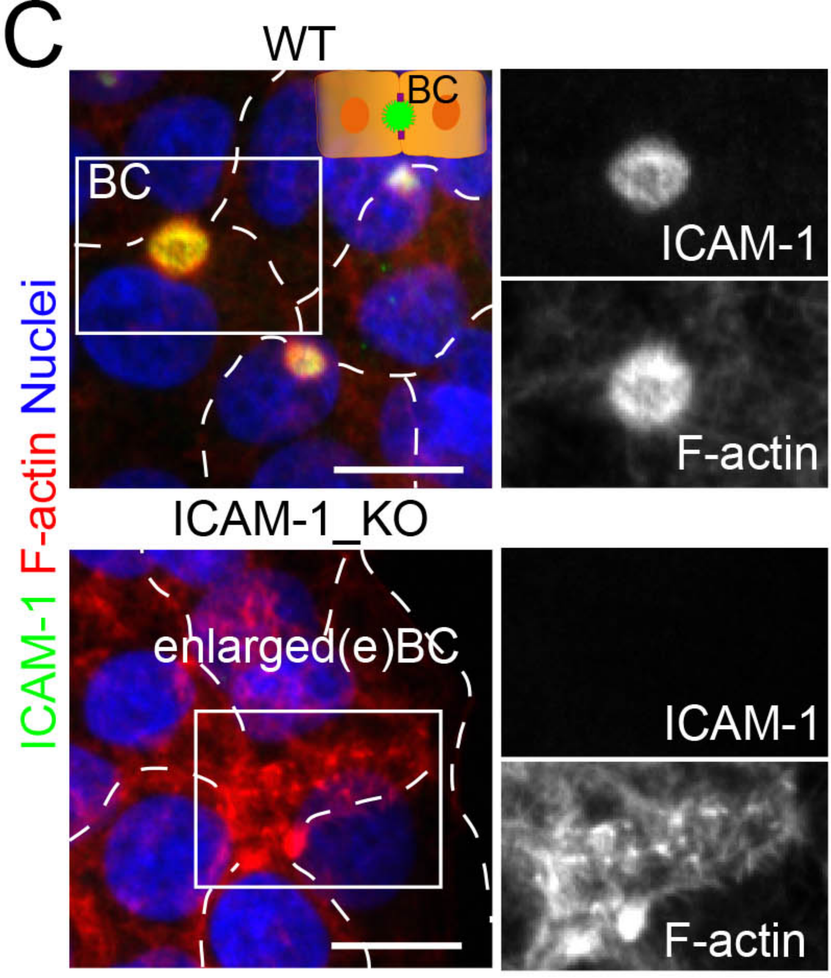
WT
BC
ICAM-1 F-actin Nuclei
ICAM-1
F-actin
ICAM-1_KO
enlarged(e)BC
ICAM-1
F-actin

D

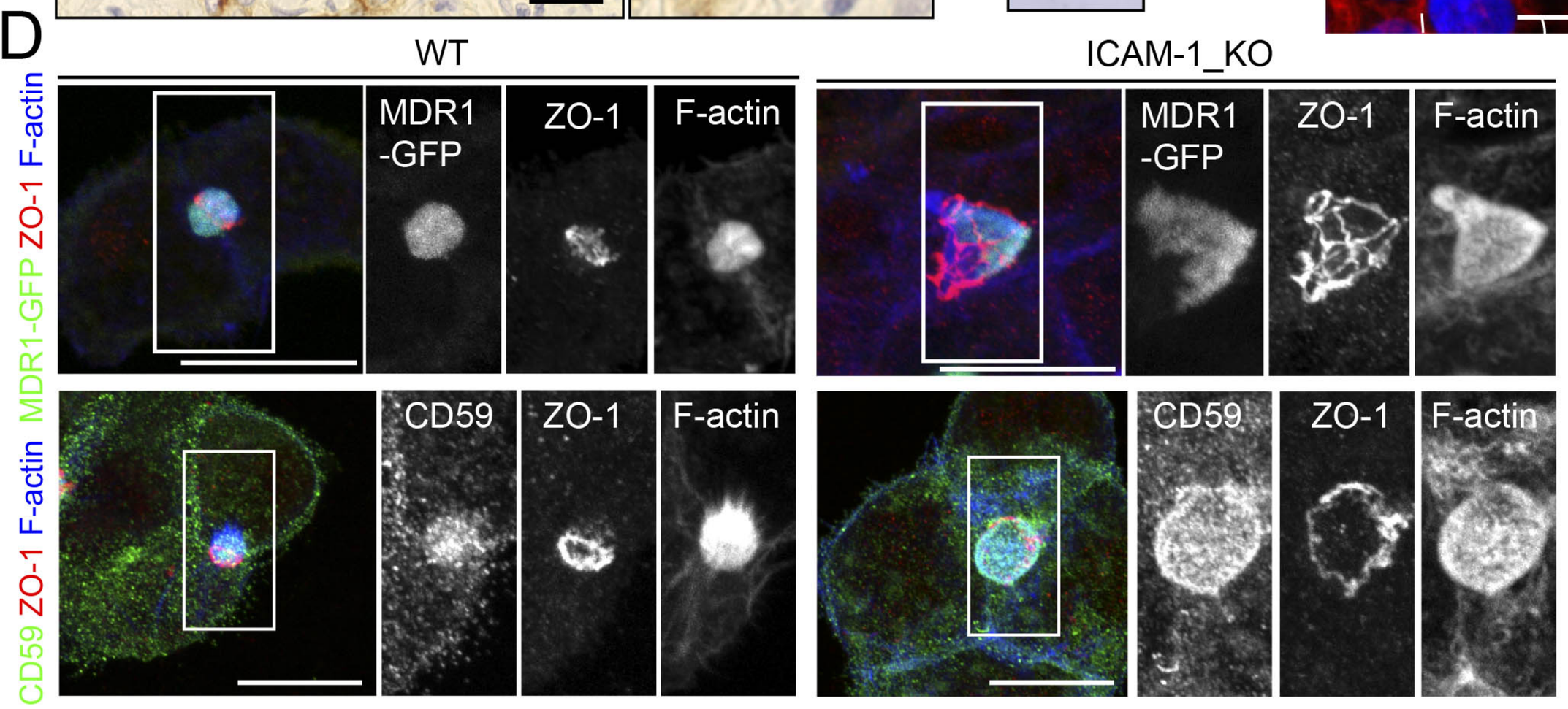
WT
ICAM-1_KO
MDR1-GFP ZO-1 F-actin
MDR1 -GFP
ZO-1
F-actin
CD59 ZO-1 F-actin
CD59

E

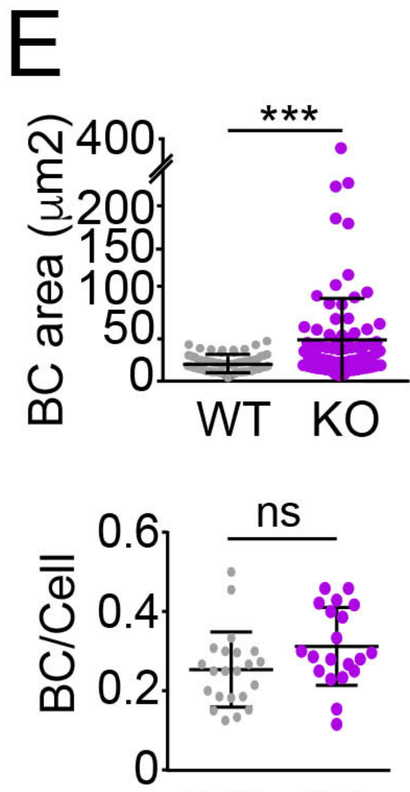
BC area (μm2)
400
200
150
100
50
0
***
WT
KO
BC/Cell
0.6
0.4
0.2
0
ns
WT
KO

F

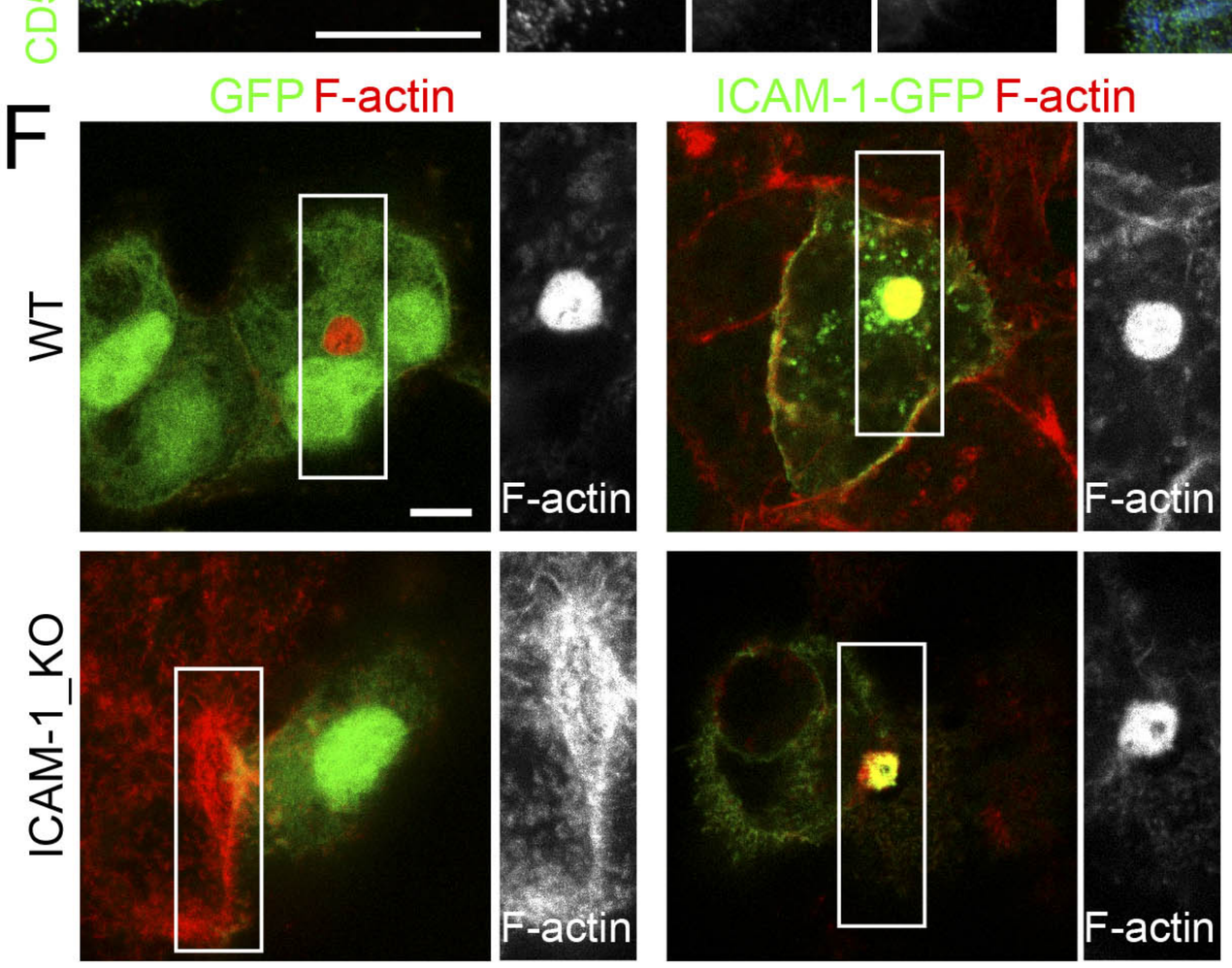
GFP F-actin
ICAM-1-GFP F-actin
WT
ICAM-1_KO
F-actin

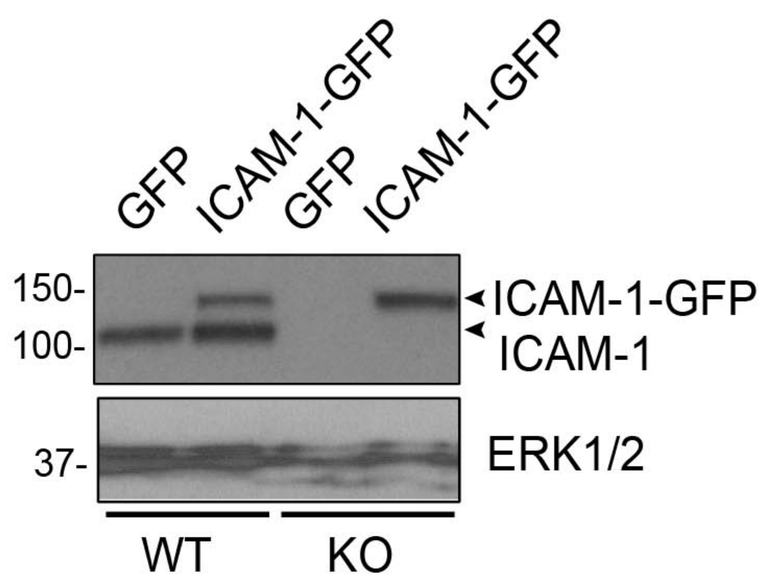
GFP
ICAM-1-GFP
GFP
ICAM-1-GFP
150-
100-
ICAM-1-GFP
ICAM-1
37-
ERK1/2
WT
KO

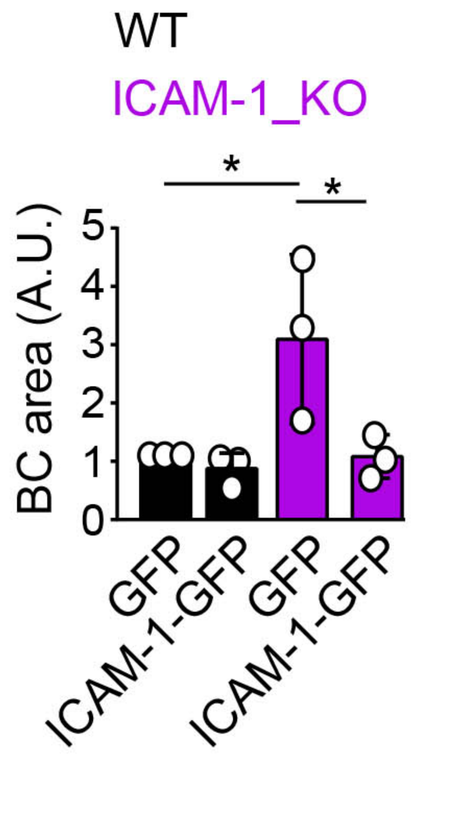
WT
ICAM-1_KO
*
*
BC area (A.U.)
5
4
3
2
1
0
GFP
ICAM-1-GFP
GFP
ICAM-1-GFP

G

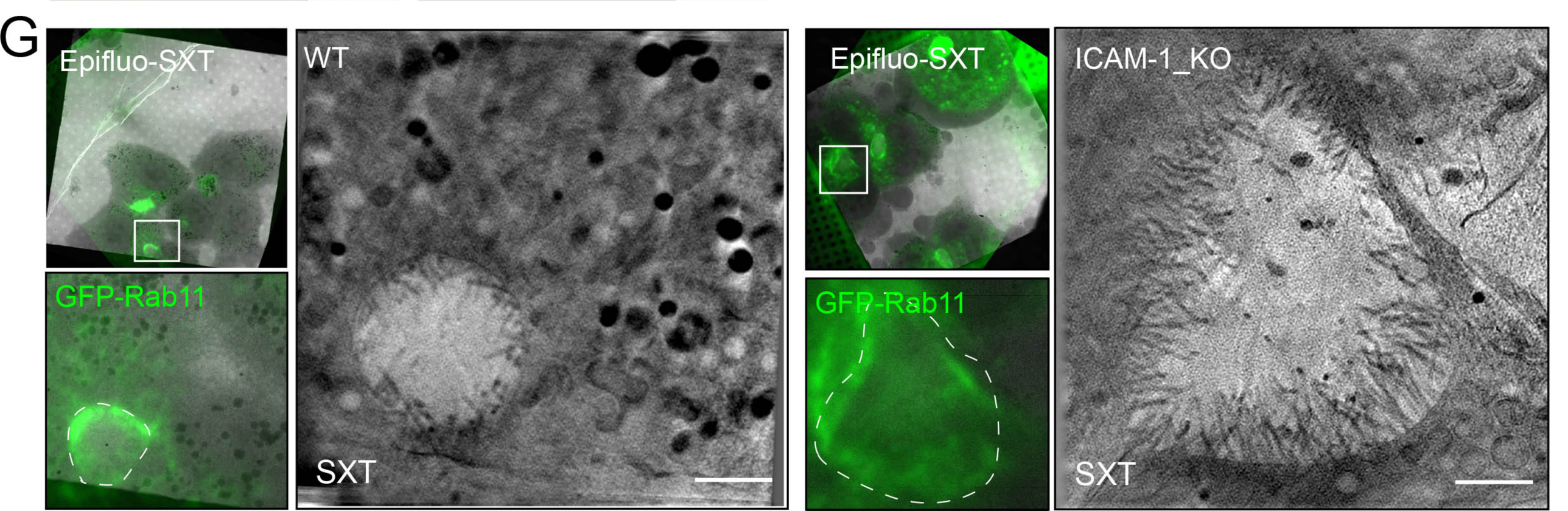
Epifluo-SXT
GFP-Rab11
WT
SXT
Epifluo-SXT
GFP-Rab11
ICAM-1_KO
SXT

A

ICAM-1_KO

Epifluo-SXT

GFP-Rab11

SXT

B

MDR1-GFP

WT

ICAM-1_KO

0 (h)

6

12

18

MDR2-GFP-postive BCs

80
60
40
20
0

6
55
21
40
fused
non-fused

WT KO

ΔBC area (%)

100
80
60
40
20
0

WT KO

C

F-actin ZO-1 Nuclei

WT

ICAM-1 KO

F-actin

ZO-1

BC area (μm2)

150
100
50
0

****
****
***
***
****
*
*
*

48 72 96 48 72 96

Time (h)

WT ICAM-1 KO

D

F-actin ZO-1 Nuclei

E

F-actin Surface biotinylation Nuclei

XZ

BC

eBC

A

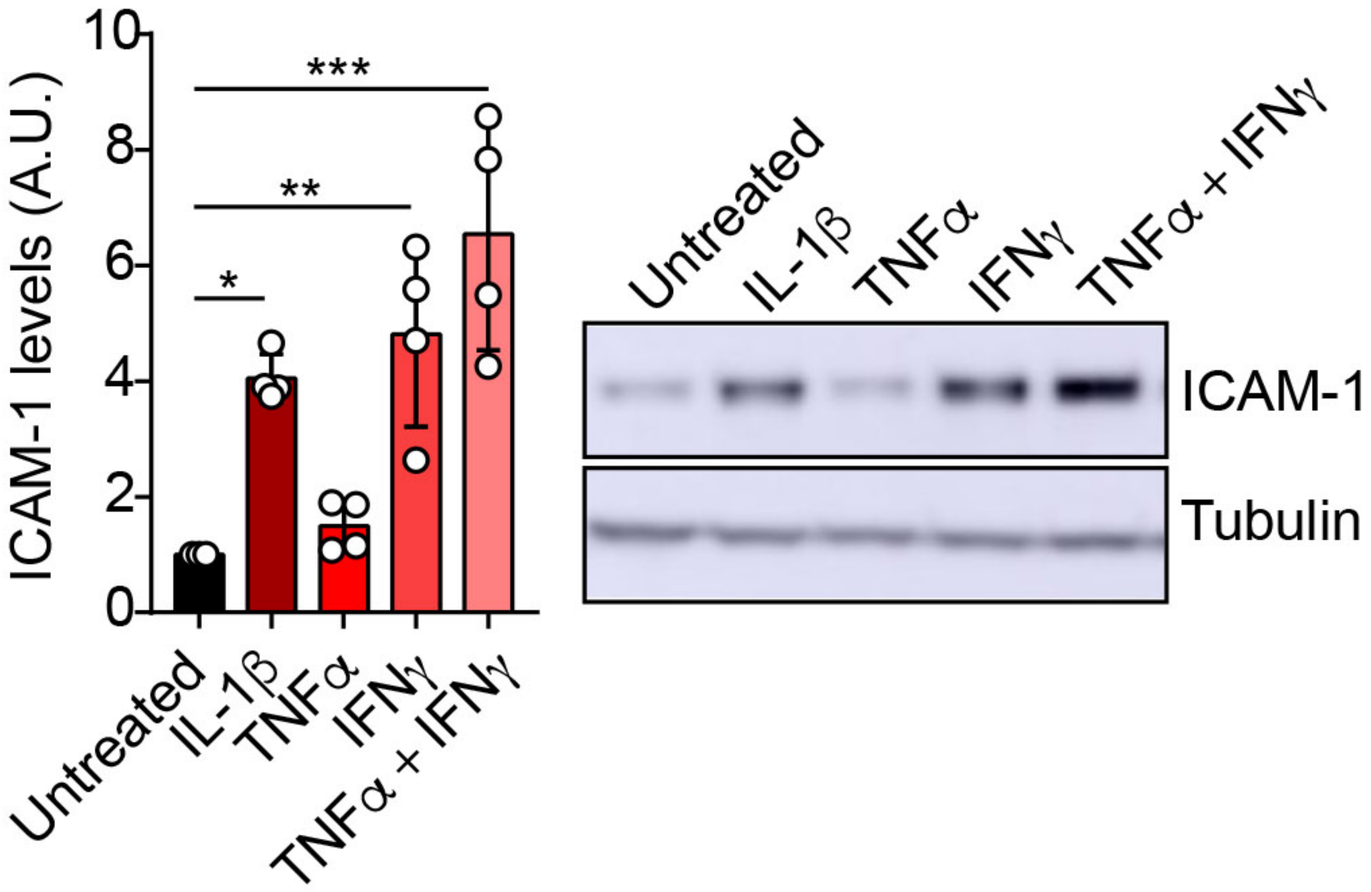
ICAM-1 levels (A.U.)
0
2
4
6
8
10
*
**
***
Untreated
IL-1β
TNFα
IFNγ
TNFα + IFNγ
ICAM-1
Tubulin

B

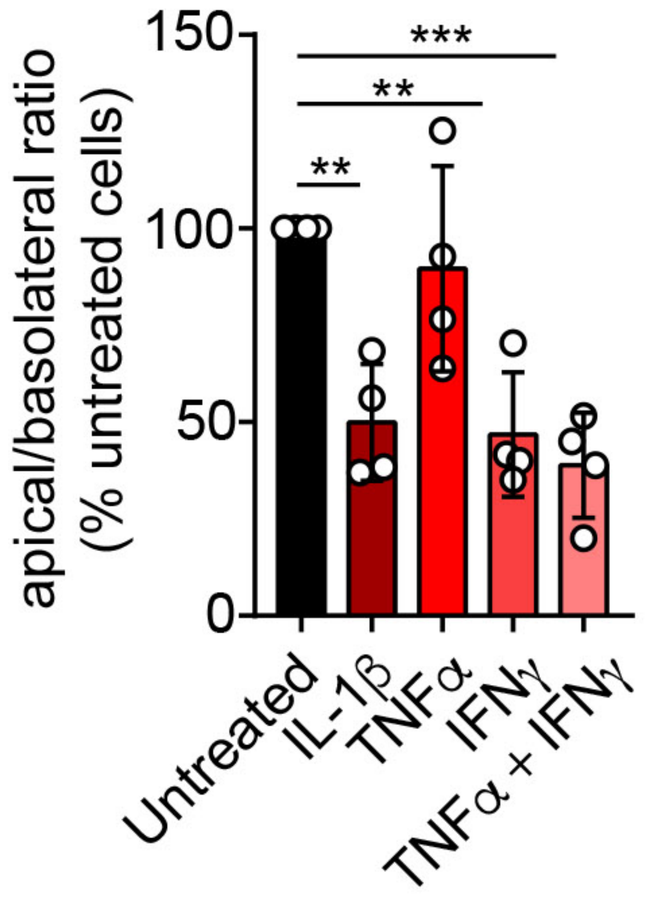
apical/basolateral ratio
(% untreated cells)
0
50
100
150
**
**
***
Untreated
IL-1β
TNFα
IFNγ
TNFα + IFNγ

C

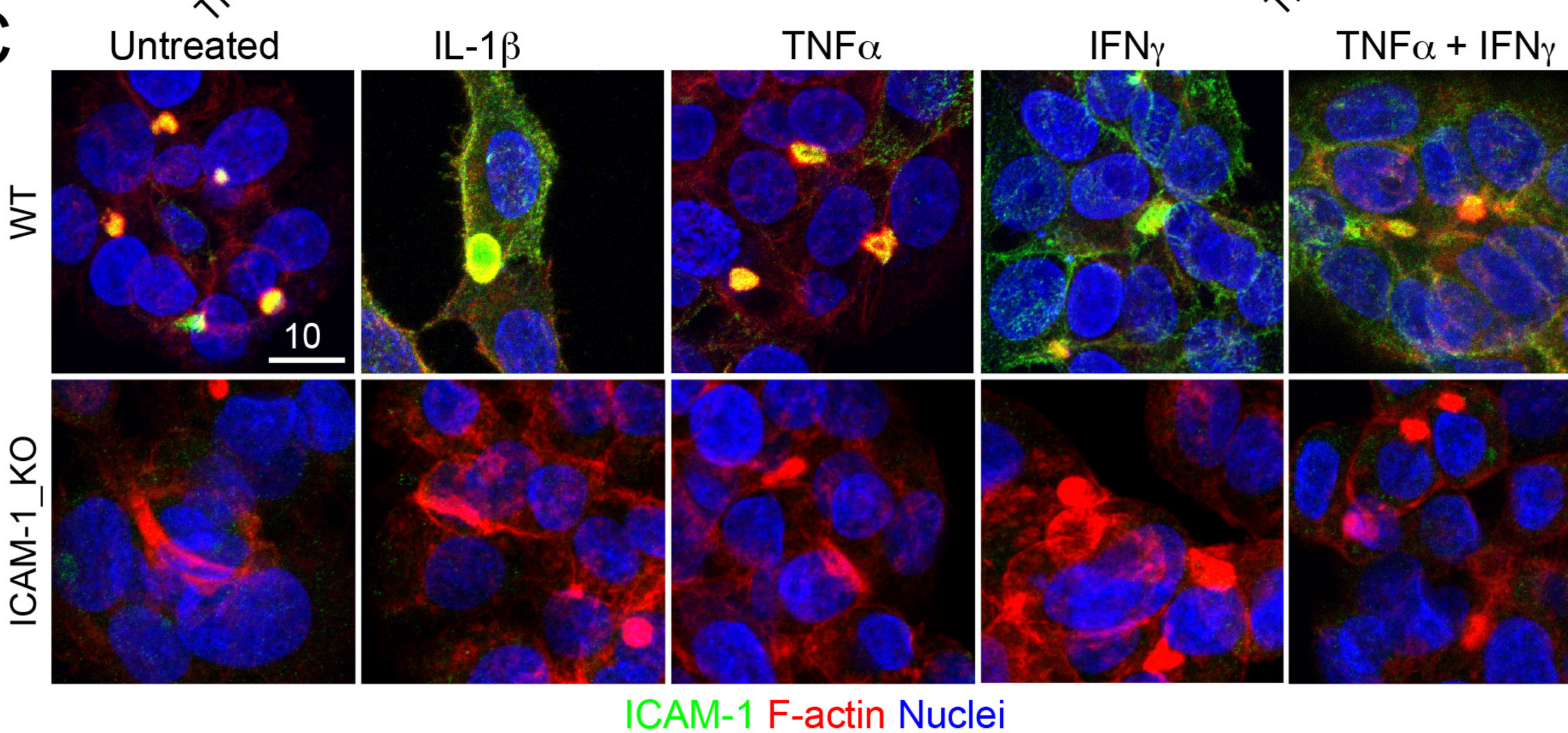
Untreated
IL-1β
TNFα
IFNγ
TNFα + IFNγ
WT
ICAM-1_KO
10
ICAM-1 F-actin Nuclei

D

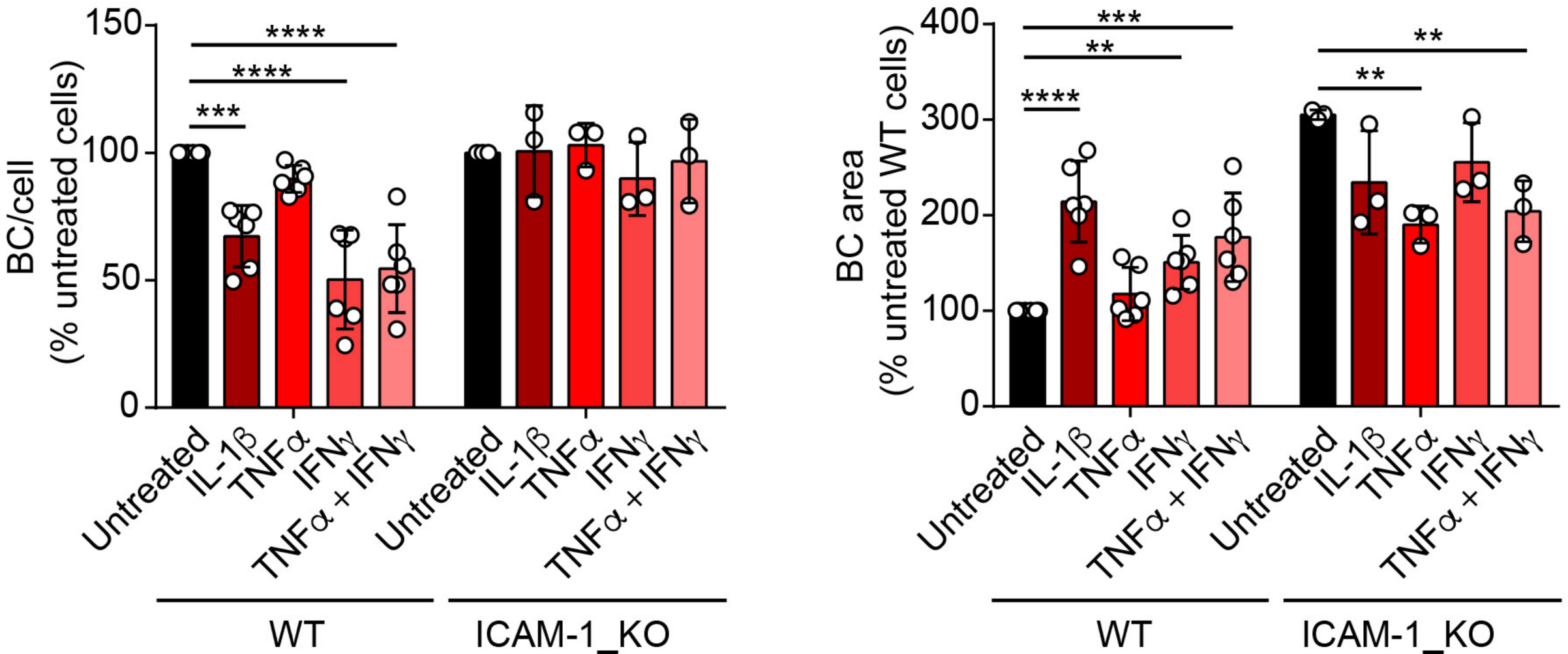
BC/cell
(% untreated cells)
0
50
100
150
***
****
****
BC area
(% untreated WT cells)
0
100
200
300
400
****
**
***
**
**
Untreated
IL-1β
TNFα
IFNγ
TNFα + IFNγ
WT
ICAM-1_KO

A

MLC-GFP SirActin (projection)

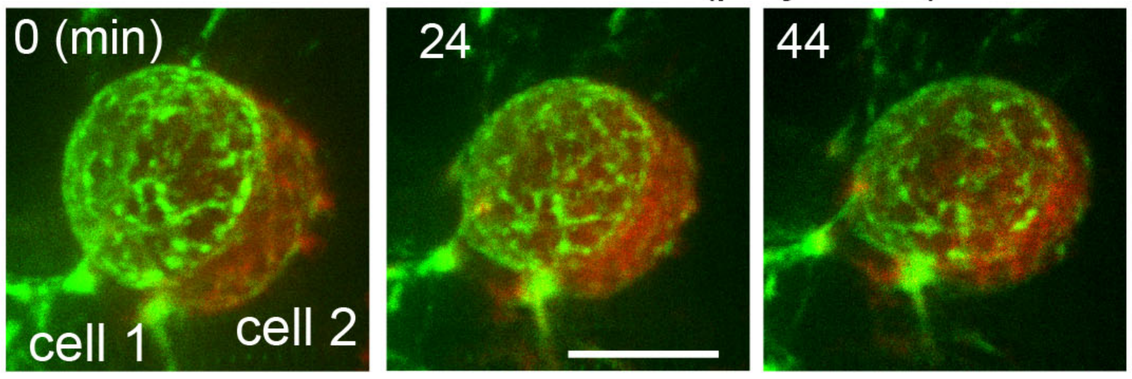


MLC-GFP SirActin (single image)

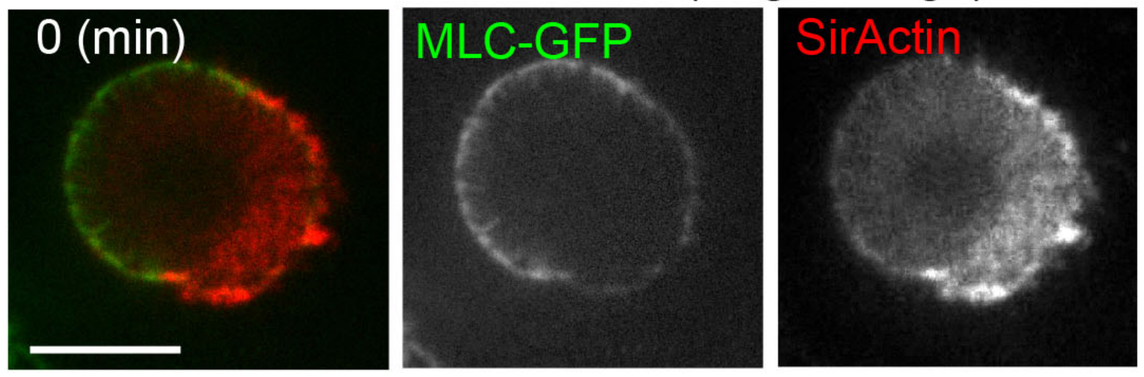


B

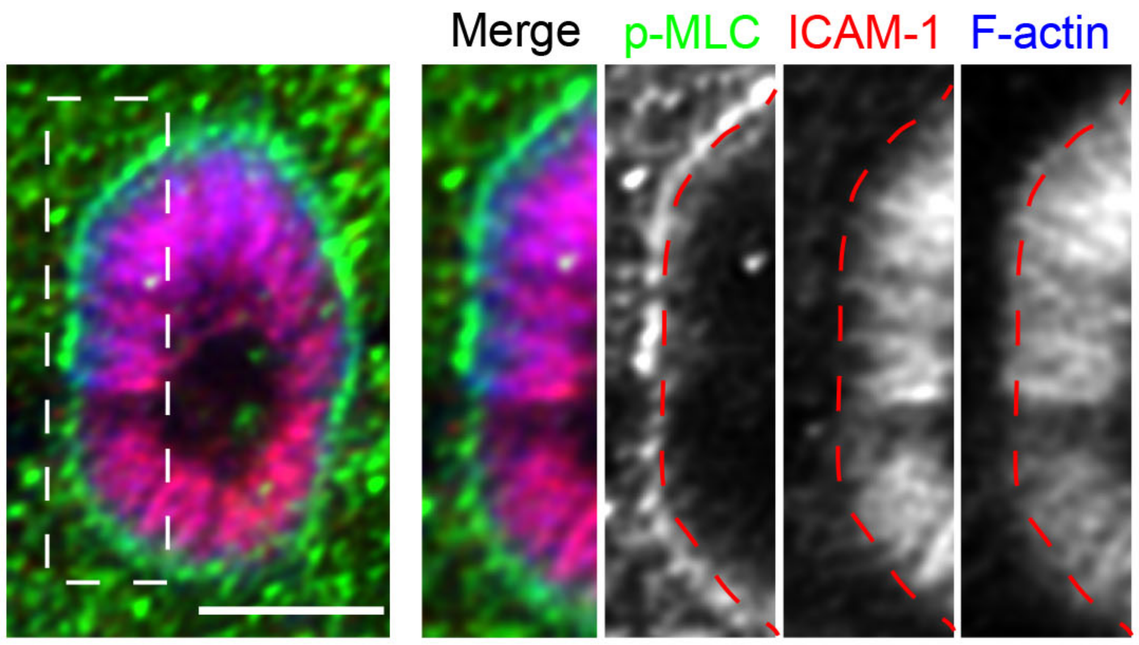


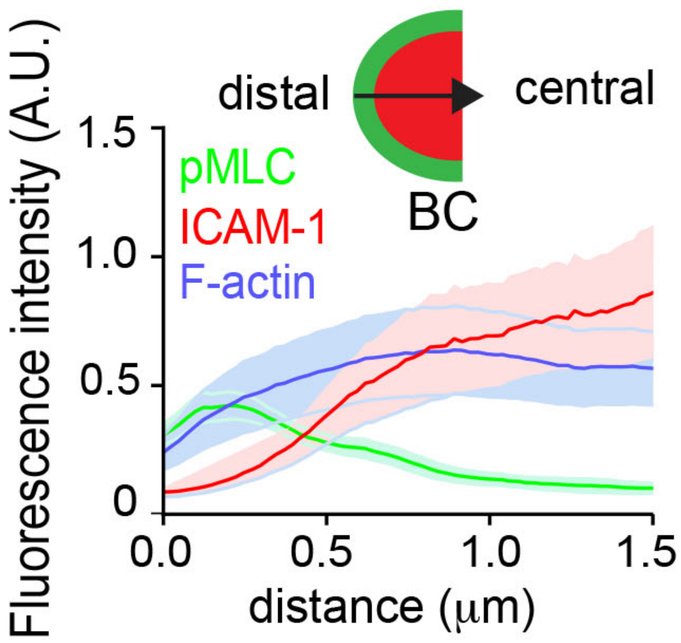


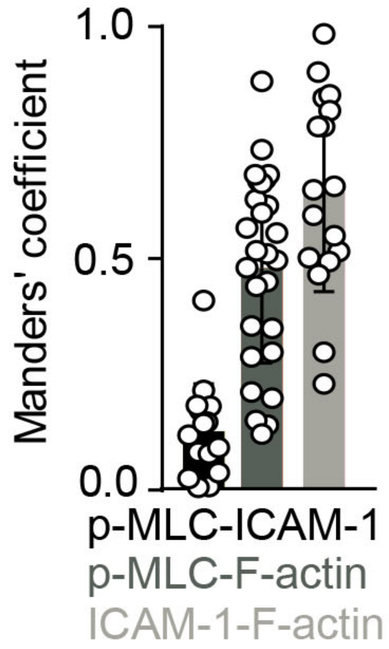


C

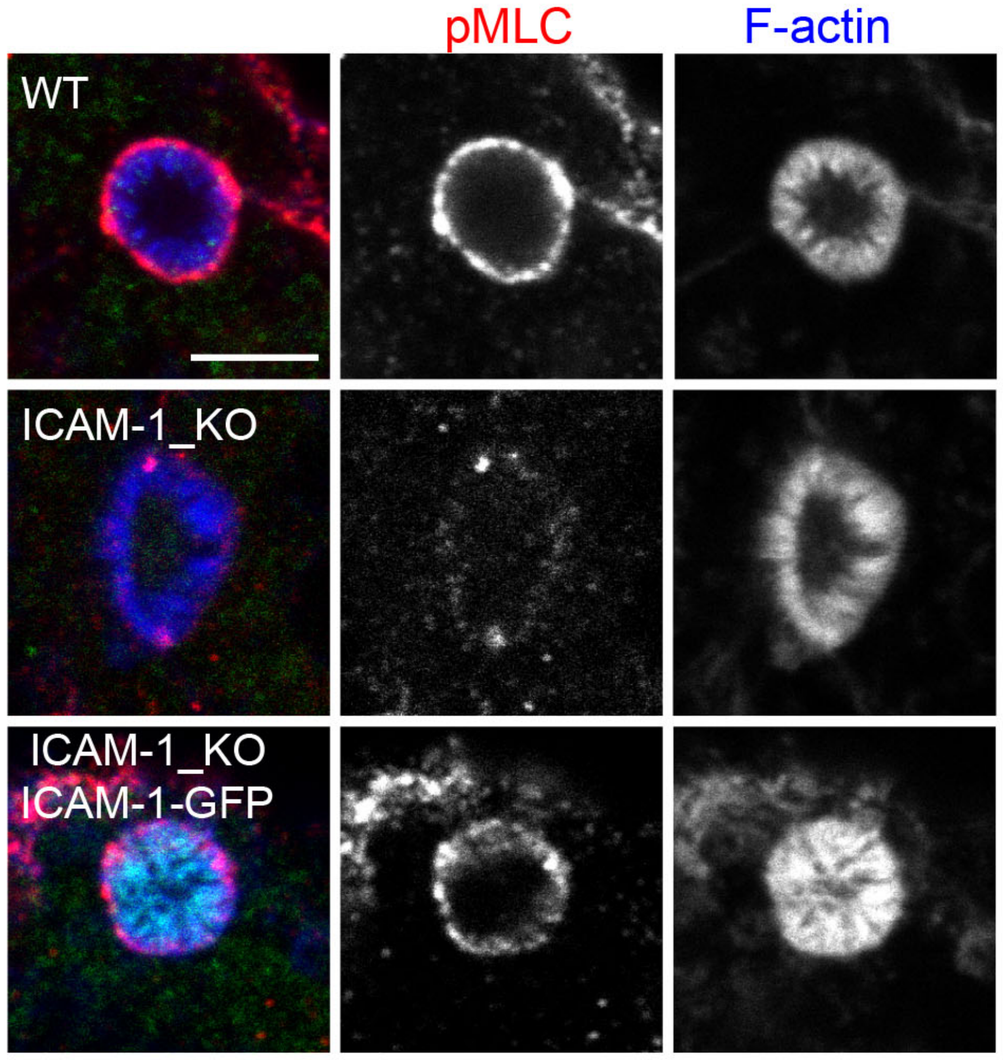


D

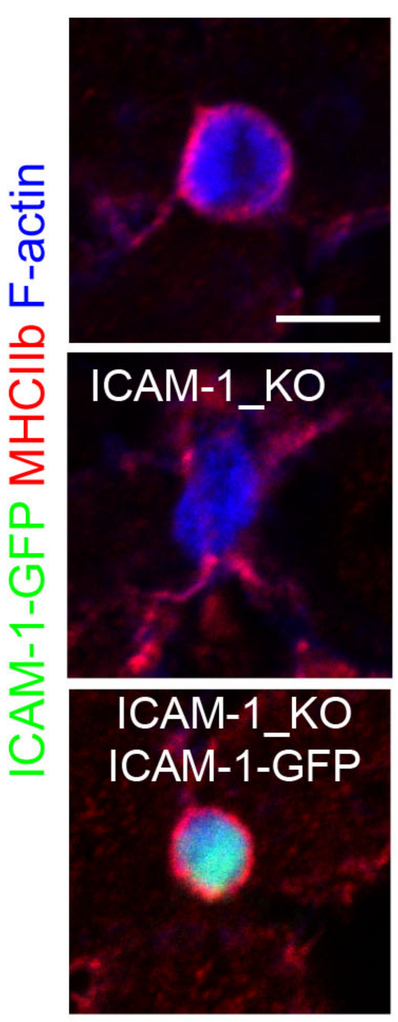


E

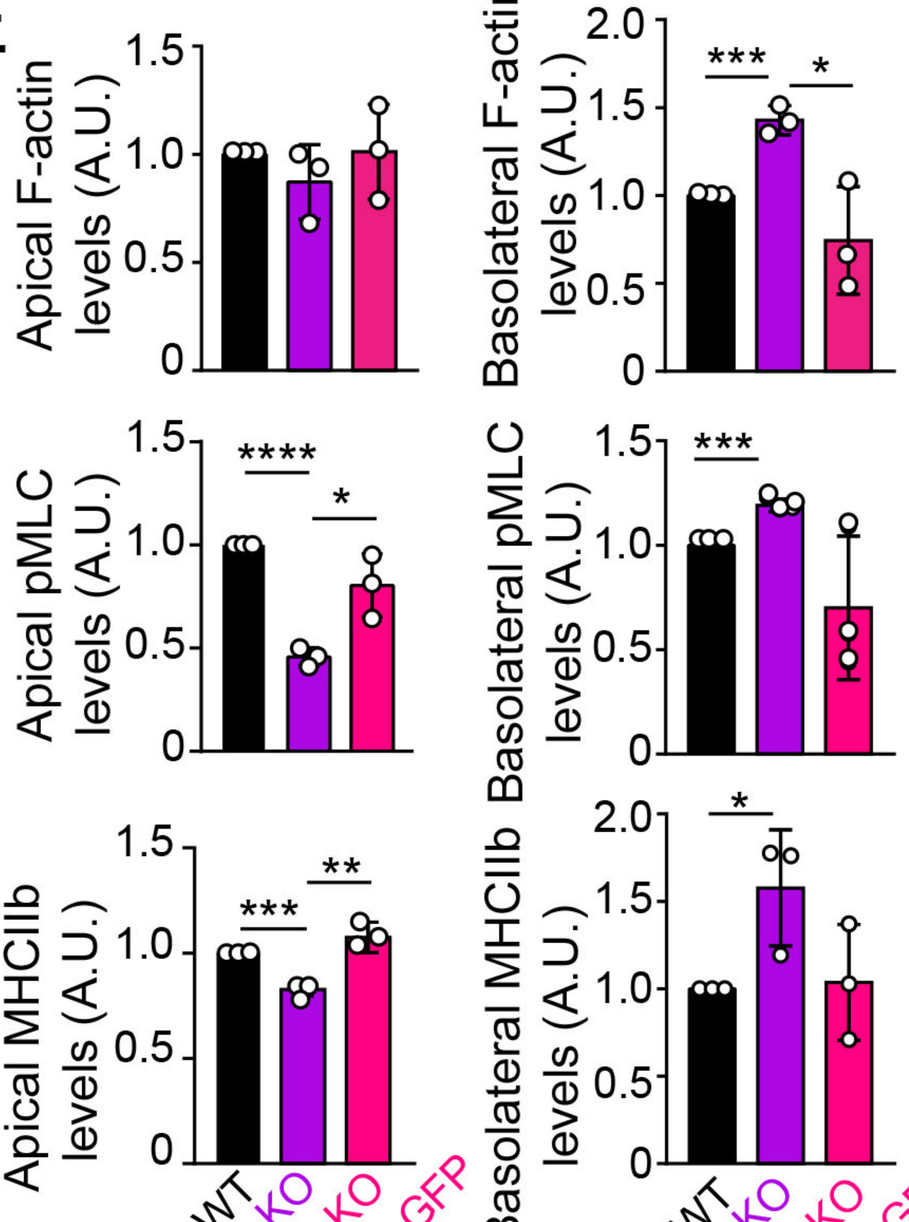


F

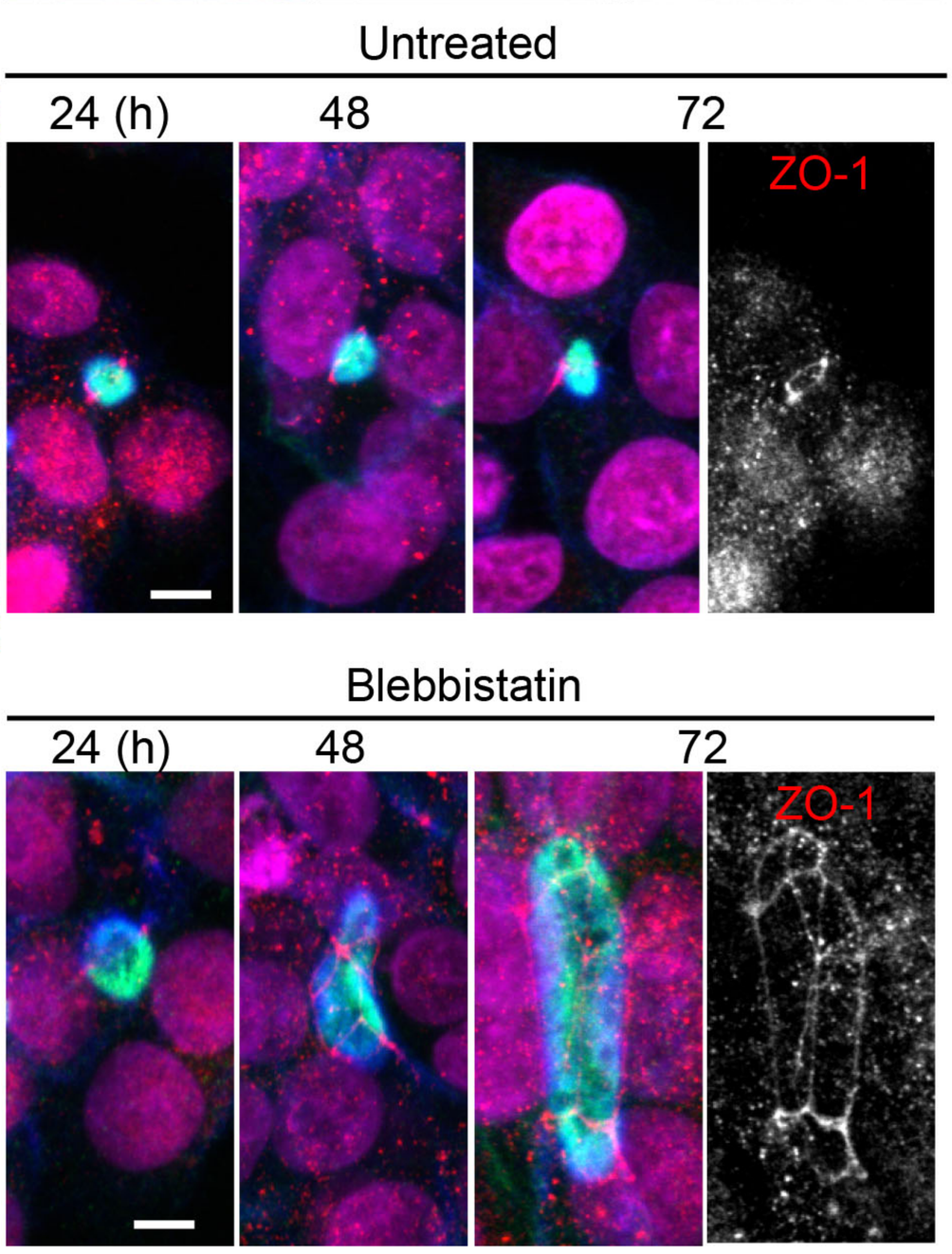


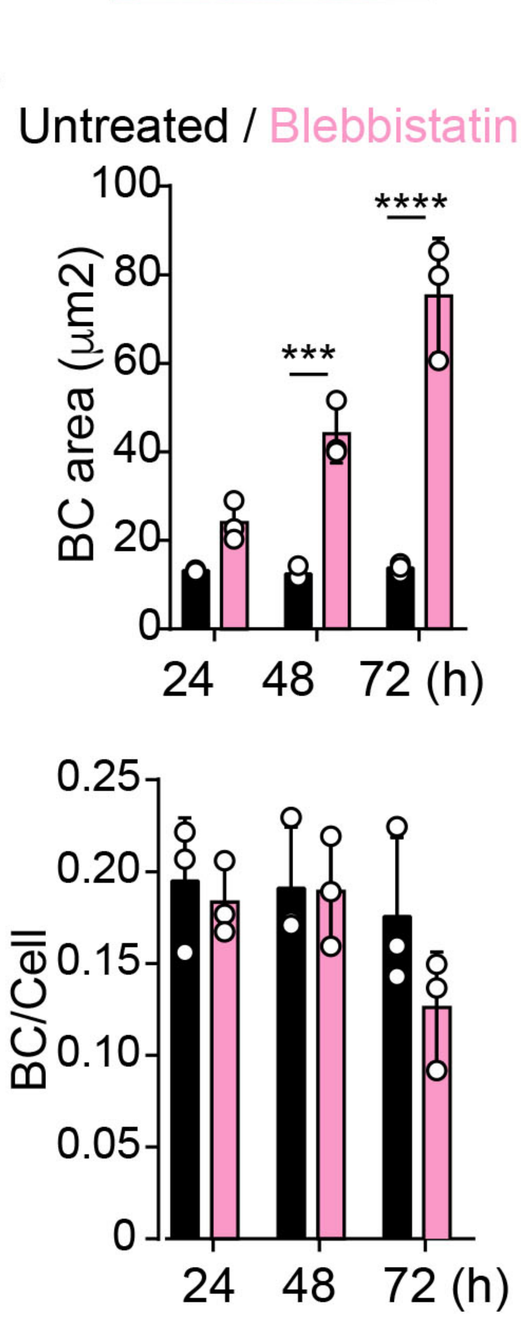


G

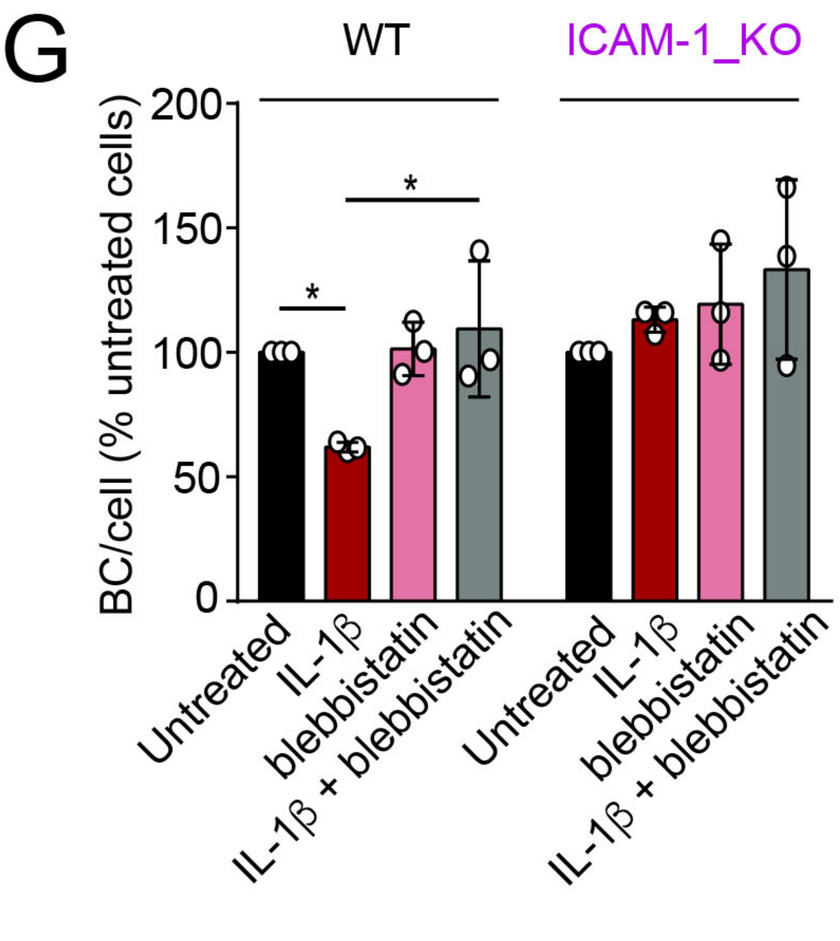

A

ICAM-1-GFP F-actin Nuclei

PBS (coating)

IgG control

αICAM-1

ICAM-1-GFP

αTfR

FN

F-actin

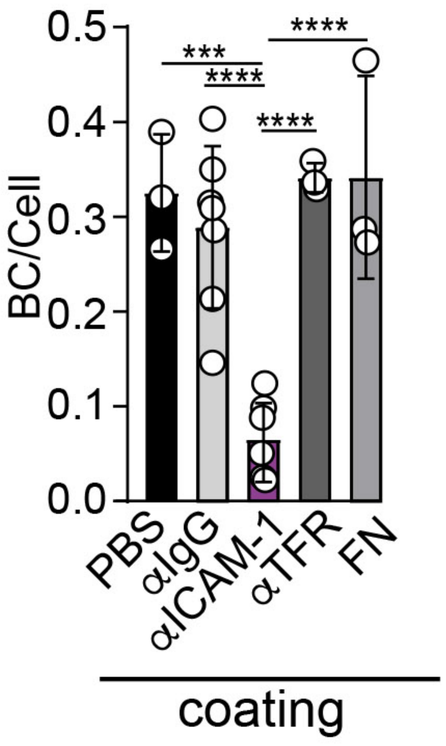


C

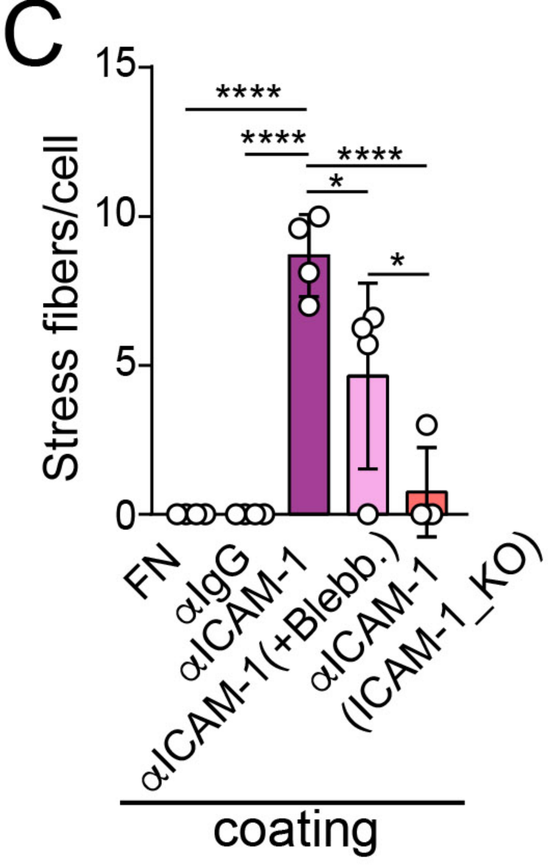


B

pMLC F-actin Nuclei

αICAM-1 (coating)

WT

WT + Blebbistatin

ICAM-1_KO

IgG (coat.) (WT)

FN (coat.) (WT)

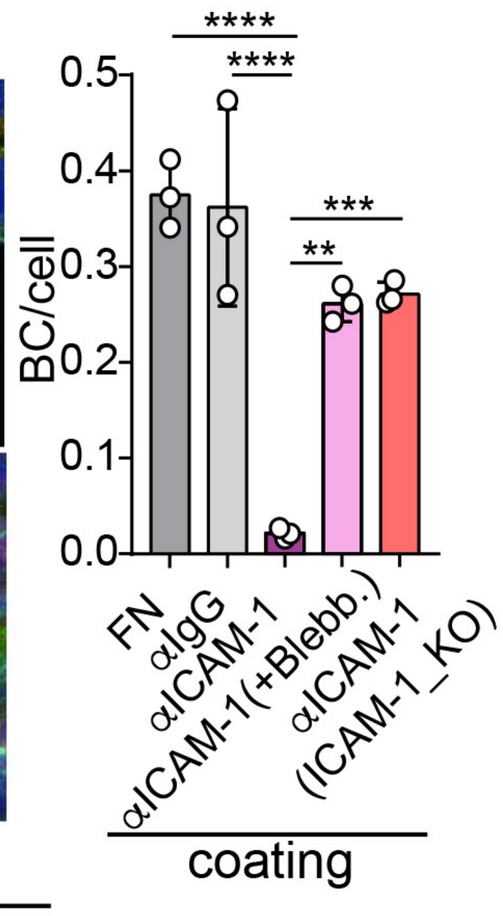


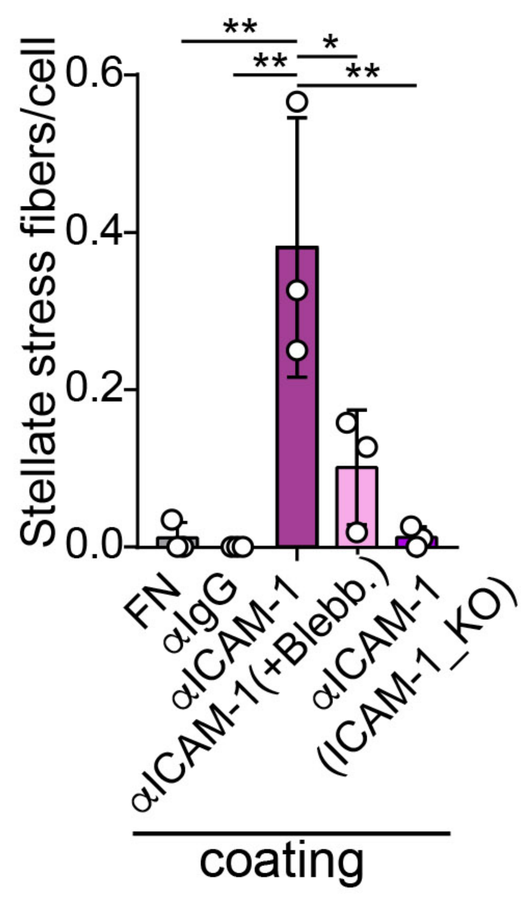


D

MDR1-GFP pMLC F-actin Nuclei

αICAM-1 (coating)

Untreated

Blebbistatin

MDR1-GFP

pMLC

F-actin

E

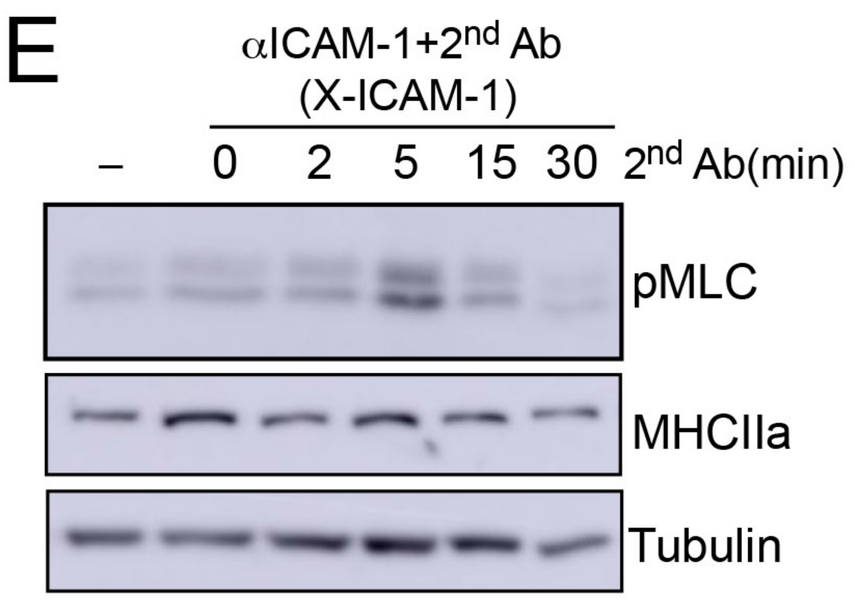


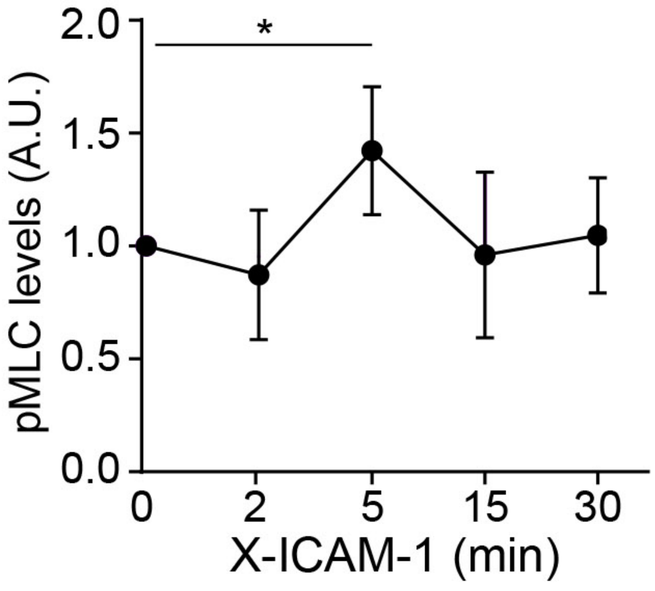


F

ICAM-1-GFP F-actin CD3 Nuclei

0 (h)

6

24

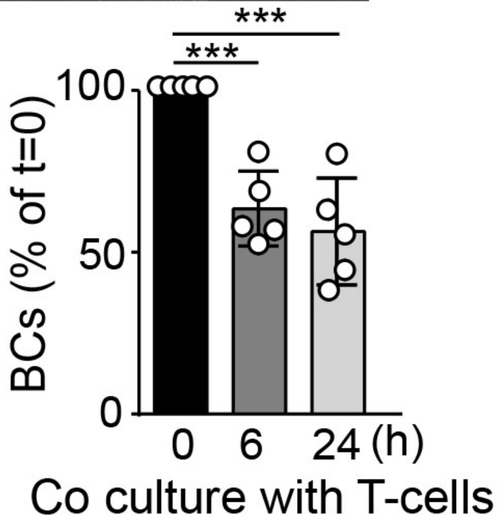


G

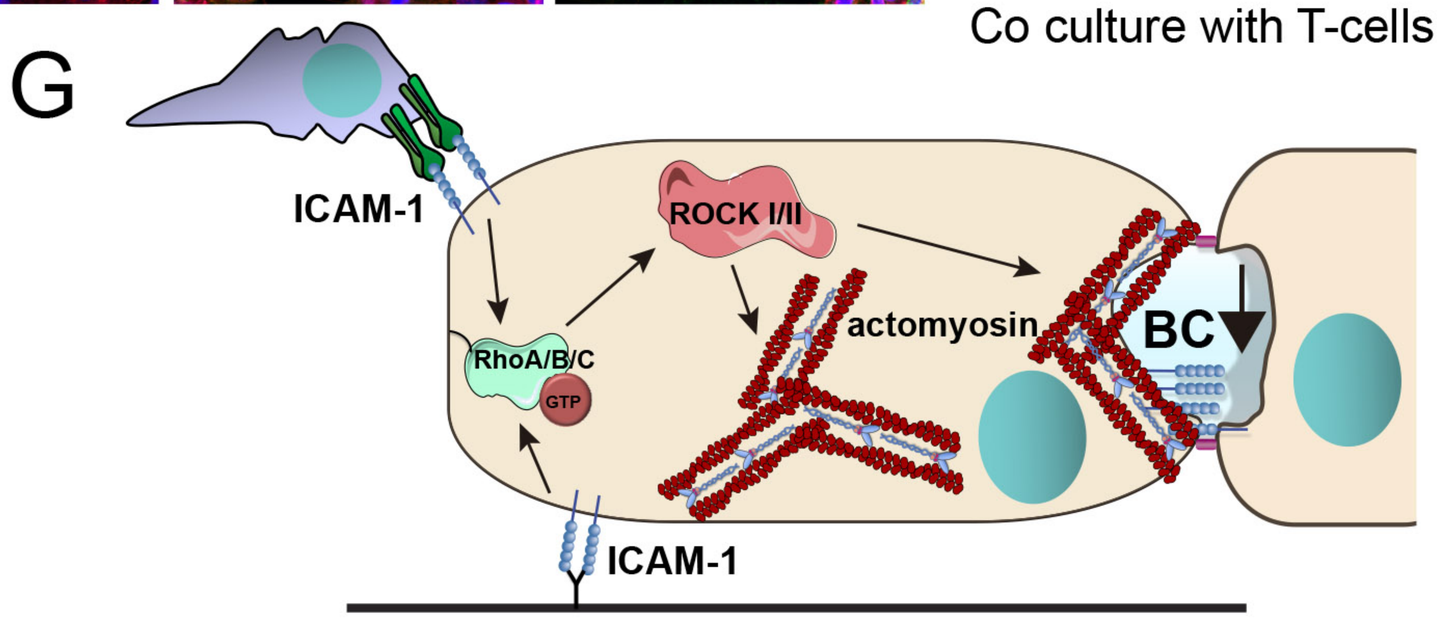

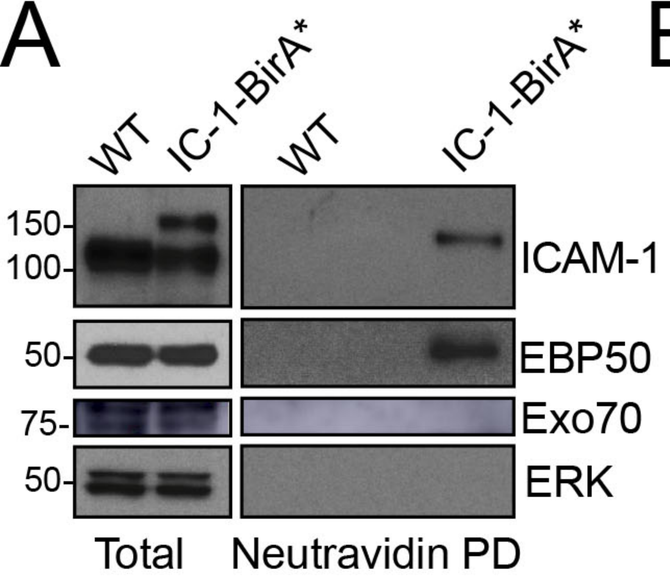
A
WT
IC-1-BirA*
WT
IC-1-BirA*
150-
100-
ICAM-1
50-
EBP50
75-
Exo70
50-
ERK
Total
Neutravidin PD

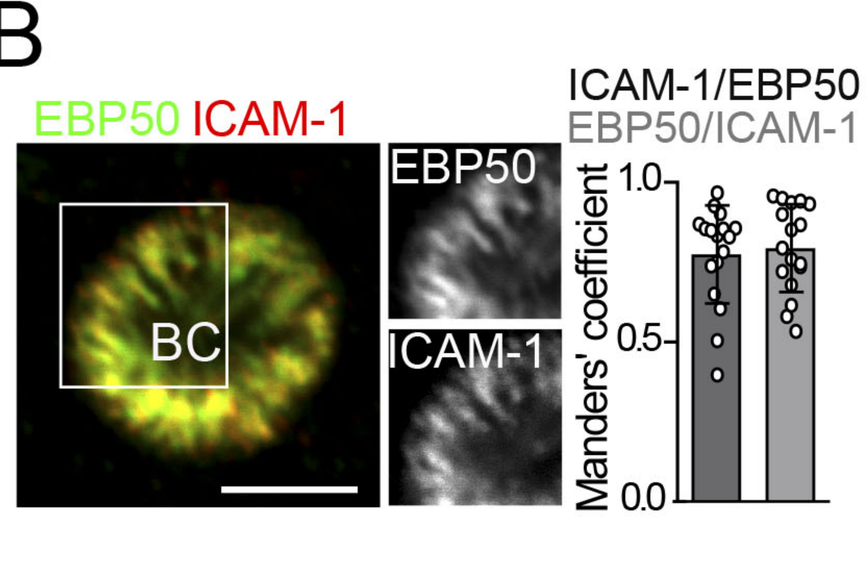
B
EBP50 ICAM-1
BC
EBP50
ICAM-1
ICAM-1/EBP50
EBP50/ICAM-1
Manders' coefficient
1.0
0.5
0.0

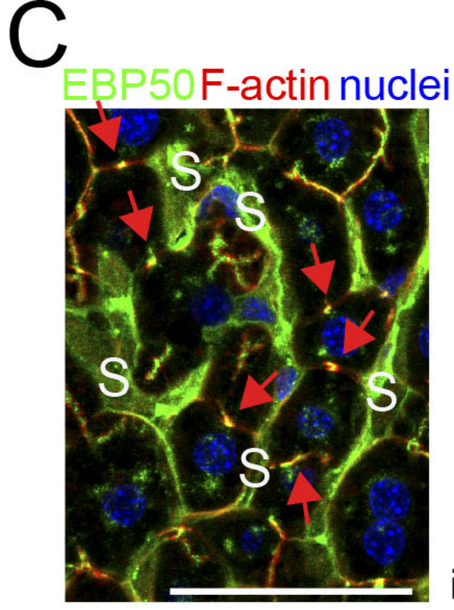
C
EBP50 F-actin nuclei
S
S
S
S
S
S

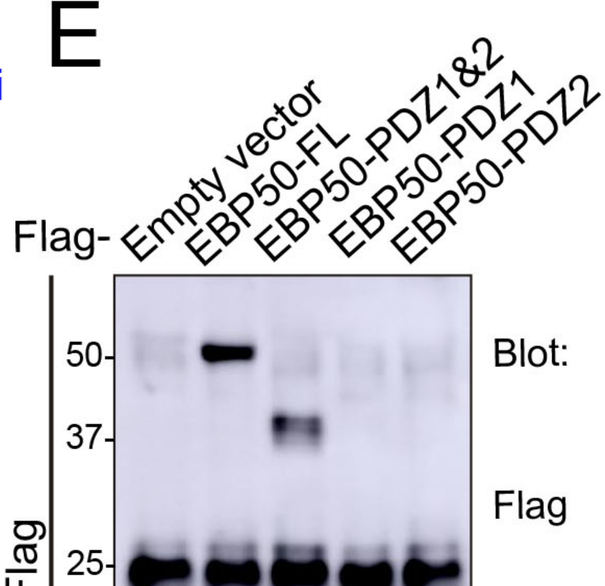
E
Flag-
Empty vector
EBP50-FL
EBP50-PDZ1&2
EBP50-PDZ1
EBP50-PDZ2
IP anti-Flag
50-
37-
25-
20-
Blot:
Flag
100-
ICAM-1
Lysate
100-
ICAM-1

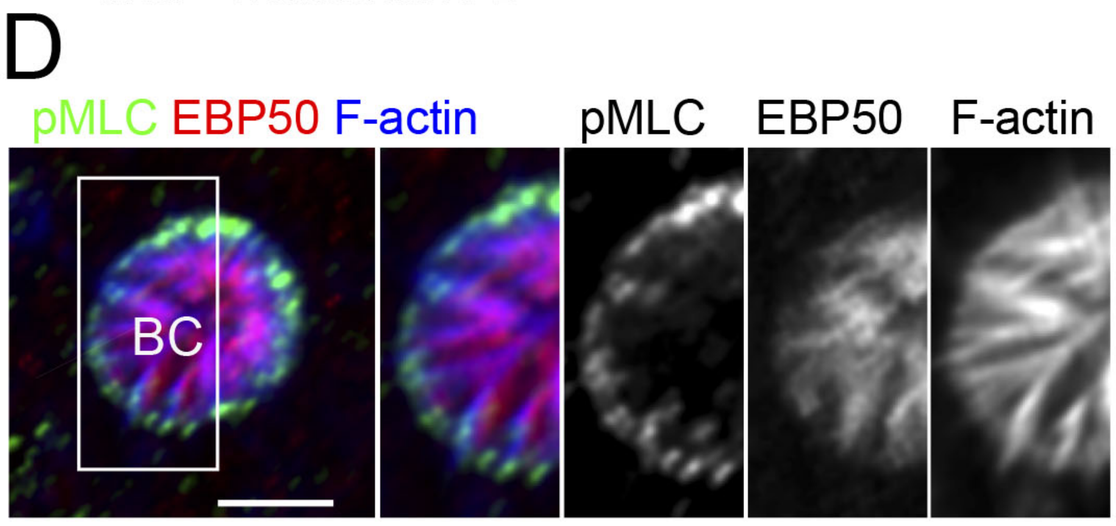
D
pMLC EBP50 F-actin
BC
pMLC
EBP50
F-actin

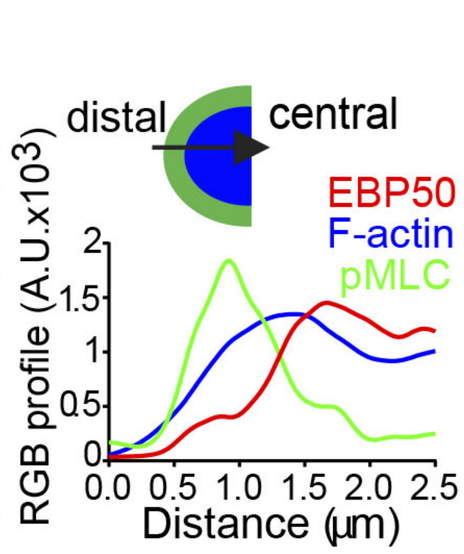
distal
central
EBP50
F-actin
pMLC
RGB profile (A.U.x10³)
2
1.5
1
0.5
0
0.0 0.5 1.0 1.5 2.0 2.5
Distance (μm)

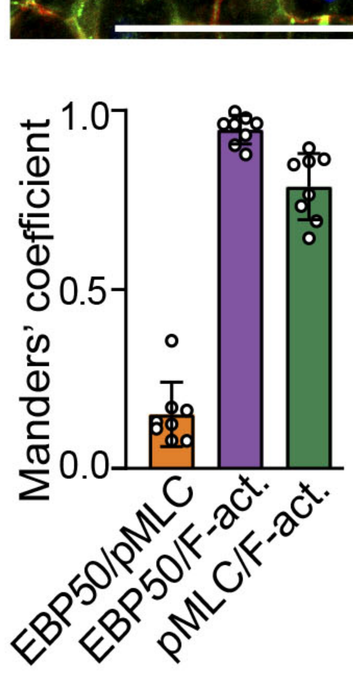
Manders' coefficient
1.0
0.5
0.0
EBP50/pMLC
EBP50/F-act.
pMLC/F-act.

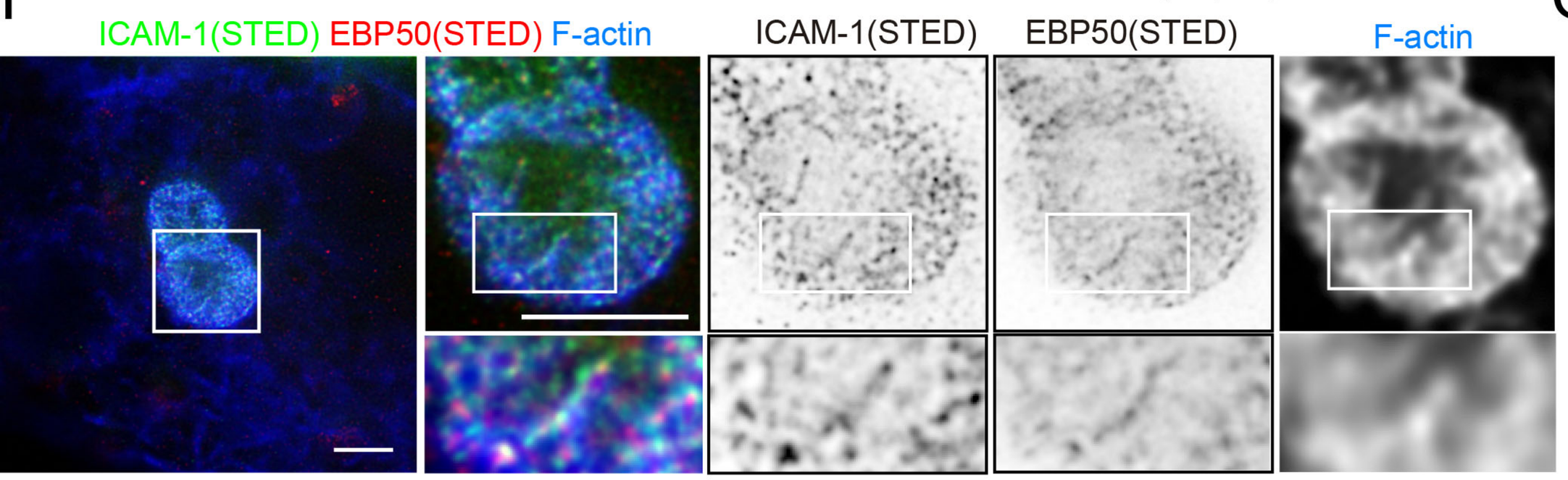
F
ICAM-1(STED) EBP50(STED) F-actin
ICAM-1(STED)
EBP50(STED)
F-actin

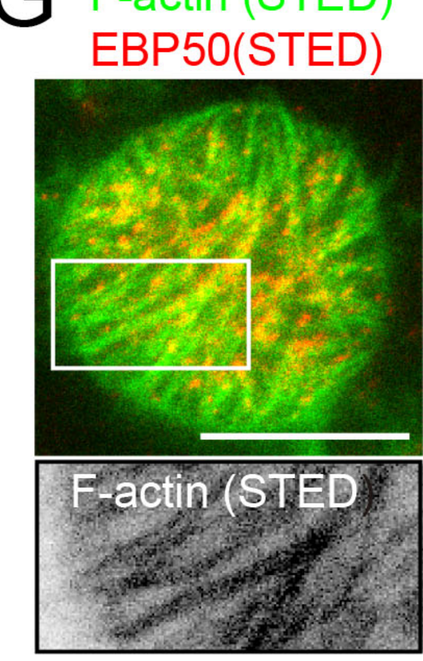
G
F-actin (STED)
EBP50(STED)
F-actin (STED

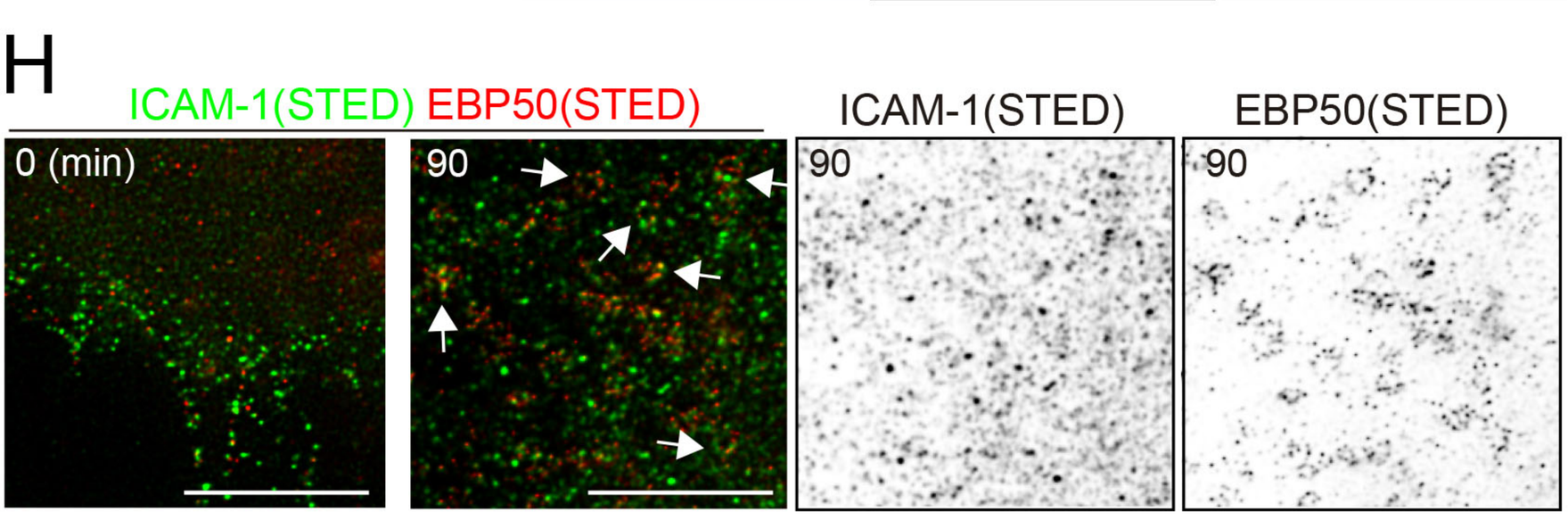
H
ICAM-1(STED) EBP50(STED)
0 (min)
90
ICAM-1(STED)
EBP50(STED)
90
90

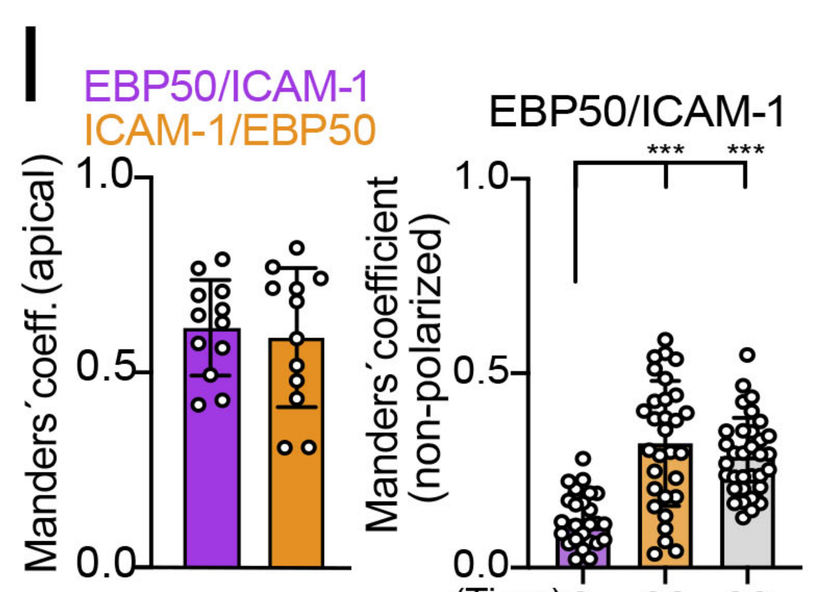
I
EBP50/ICAM-1
ICAM-1/EBP50
Manders´coeff. (apical)
1.0
0.5
0.0
EBP50/ICAM-1
Manders´coefficient (non-polarized)
***
***
(Time) 0
30
90

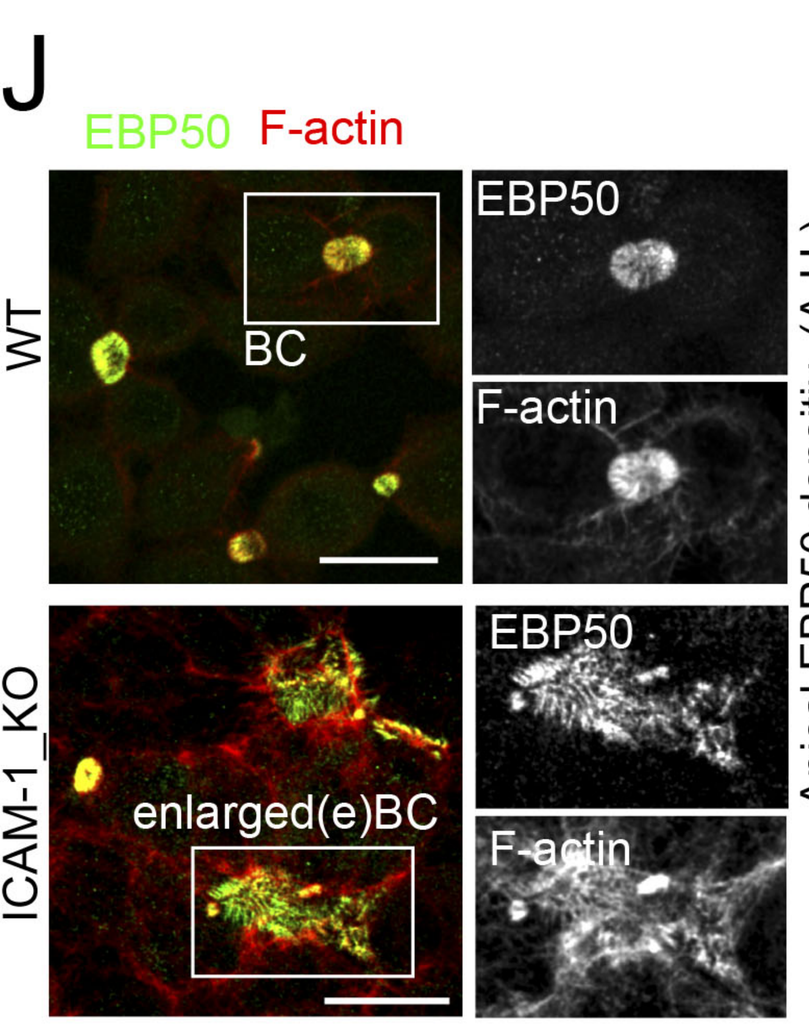
J
EBP50 F-actin
WT
BC
EBP50
F-actin
ICAM-1_KO
enlarged(e)BC
EBP50
F-actin
Apical EBP50 density (A.U.)
1.0
0.5
0
WT
KO

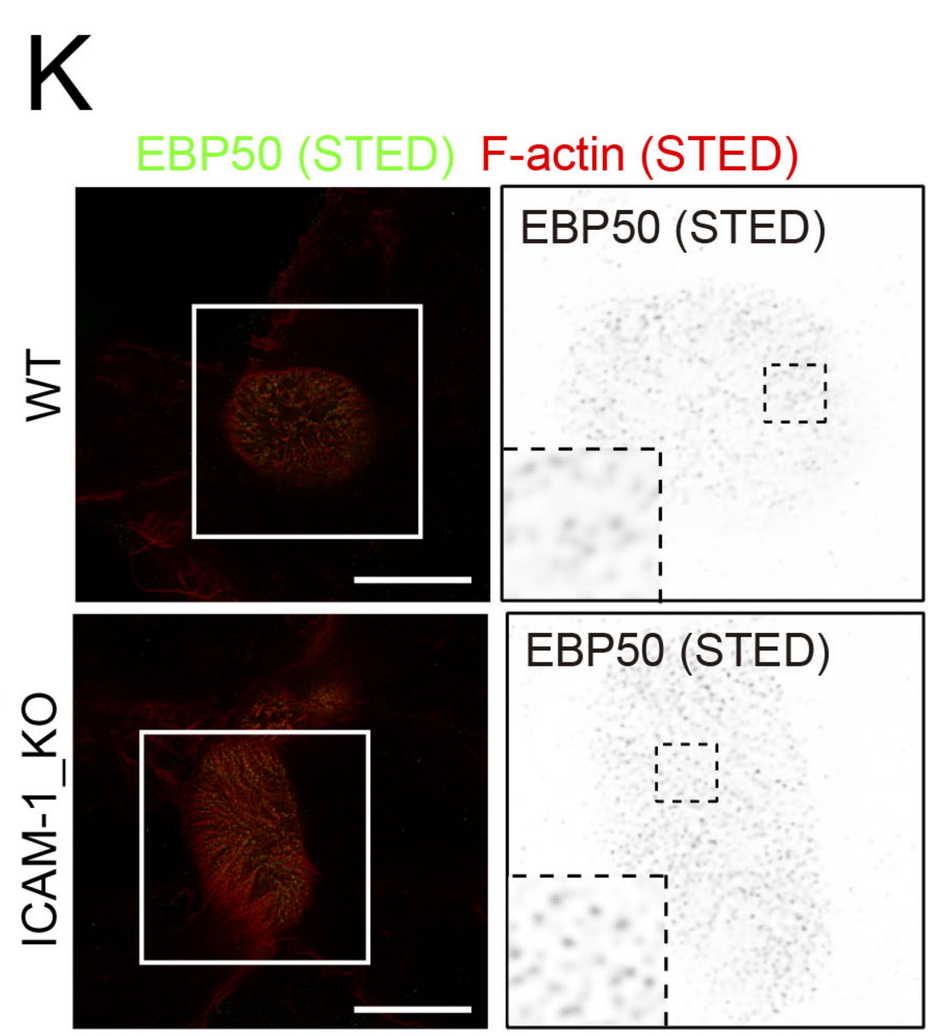
K
EBP50 (STED) F-actin (STED)
WT
ICAM-1_KO
EBP50 (STED)
EBP50 (STED)

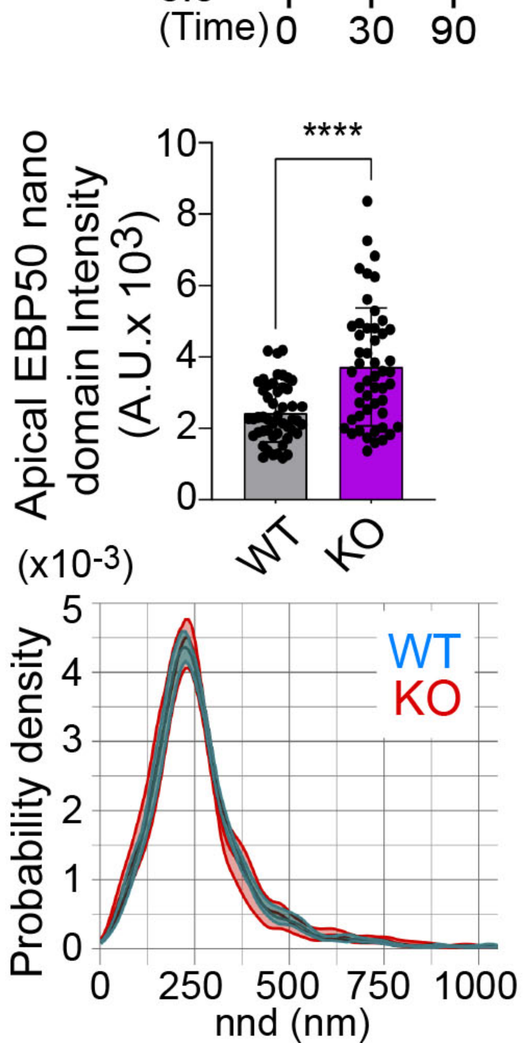
Apical EBP50 nano domain Intensity (A.U.x 10³)
10
8
6
4
2
0
****
WT
KO
(x10⁻³)
Probability density
5
4
3
2
1
0
WT
KO
0
250
500
750
1000
nnd (nm)

A

siControl siEBP50

EBP50 -50

GAPDH -37

EBP50 levels (A.U.)

B

siControl

siEBP50

EBP50 F-actin

EBP50 levels in BC (A.U.)

BC area (μm2)

BC/Cell

F-actin levels in BC (A.U.)

pMLC levels in BC (A.U.)

C

ICAM-1-GFP EBP50 F-actin

ICAM-1-GFP

EBP50

αICAM-1 (coating)

D

EBP50 F-actin Nuclei

EBP50

F-actin

si Control

si EBP50

E

siControl

siEBP50

BC/cell (% siControl on IgG)

αIgG αICAM-1

coating

Stress fibers/cell (% siControl)

αICAM-1

coating

A

ICAM-1 Nuclei

Bile canaliculi

Bile duct

S

S

S

S

B

ICAM-1 F-actin Nuclei

WT

ICAM-1 KO

BC width (μm)

5

4

3

2

1

0

***

WT ICAM-1_KO

C

F-actin MRP2 Nuclei

WT

ICAM-1 KO

D

F-actin ZO-1 Nuclei

HA-4 Nuclei

Z projection

1

HA-4 Nuclei

2

1

2

E

CFDA

CF

Hepatocyte

CFDA Nuclei

Z projection

1

CFDA Nuclei

2

1

2

F

Lateral lumen

G

ICAM-1 ZO-1 Nuclei

XY

1

2

(xz)

Mouse

xz

1

XZ

Mouse

xz

2

XZ

Mouse

XY

xz

Human

xz

XZ

Human

Central lumen

apical microvilli

cell-cell junctions

Lateral lumen

lateral microvilli

cell-cell junctions

TJ

TJ

Lateral lumen

H

WT

ICAM-1_KO

Lateral lumen area (μm2)

25

20

15

10

5

0

**** **** **** **

**** **** **** * ***

Ctl1 Ctl2 KO1 KO2 KO3 KO4 KO5

I

CFDA

WT

ICAM-1 KO

albumin secretion (A.U.)

80

60

40

20

0

Ctl KO

J

Untreated

Blebbistatin

Lateral lumen area (μm2)

***

25

20

15

10

5

0

Untr. Blebb.